Instability and Beam-Beam Study for Multi-TeV PWFA e^+e^- and $\gamma\gamma$ Linear Colliders

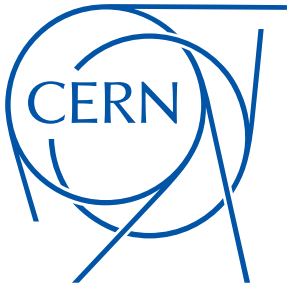

Jian Bin Ben Chen

Beams Department,
The European Organization for Nuclear Research

Department of Physics,
University of Oslo

A thesis submitted for the degree of Philosophiae Doctor
October 2020

CERN-THESIS-2020-301
//2020

Series of dissertations submitted to
The Faculty of Mathematics and Natural Sciences, University of Oslo
No. 2358

ISSN 1501-7710

Cover: Hanne Baadsgaard Utigard.
Print production: Reprosentralen, University of Oslo.

Abstract

Beam-driven plasma wakefield acceleration (PWFA) is considered as one of the most promising novel acceleration technologies capable of drastically shrinking the footprints of high-energy particle colliders. There are however several challenges that have to be addressed before PWFA can be deployed for high-energy, high-efficiency, high beam brightness particle colliders. Transverse instabilities due to interactions between particle beams and accelerating structures are known to restrict the maximum beam charge in conventional accelerators, and are considered as one of the most important challenges for PWFA accelerators. This thesis focuses on transverse instabilities induced by transverse wakefields and the corresponding implications for multi-TeV PWFA e^+e^- and $\gamma\gamma$ colliders.

First, a simplified model describing the PWFA transverse instability in the form of a wake function parameterised only with an effective cavity aperture radius a is benchmarked against PIC (Particle In Cell) simulations. This wake function implies a $1/a^4$-scaling of the transverse wakefields, which indicates transverse intra-beam wakefields typically several orders of magnitude larger than in conventional acceleration structures. Furthermore, the wakefield formalism is utilised to perform a parameter study for a 1.5 TeV plasma wakefield accelerator, where the constraint on drive beam to main beam efficiency imposed by transverse wakefields is taken into account. Ultimately, an electron accelerator parameter set with promising properties in terms of energy spread, stability and luminosity per power is derived, and is the basis for subsequent PWFA e^+e^- and $\gamma\gamma$ linear collider parameter studies.

The thesis then presents a beam-beam parameter study for a TeV-scale PWFA e^+e^- linear collider using GUINEA-PIG (Generator of Unwanted Interactions for Numerical Experiment Analysis - Program Interfaced to GEANT) simulations based on the derived accelerator parameters. The beam-beam parameter study shows that the total luminosity follows the $1/\sqrt{\sigma_z}$-scaling predicted by beamstrahlung theory, where σ_z is the rms beam length, which is advantageous for PWFA, as short beam lengths are preferred. We also derive a parameter set for a 3 TeV PWFA linear collider with main beam parameters optimised for luminosity and luminosity spread introduced by beamstrahlung. Due to the considerable challenges associated with positron acceleration in plasma, this thesis also compares the performance for scenarios with reduced positron beam charge at 3 TeV and 14 TeV with CLIC (Compact Linear Collider) parameters.

We also perform a similar beam-beam parameter study for a 3 TeV $\gamma\gamma$ collider again using the derived PWFA main beam parameters. The parameter study involved using electron beams with short beam lengths in the range $2\,\mu\text{m} \leq \sigma_z \leq 10\,\mu\text{m}$ to scatter the laser photons. The results for such short examined electron beam lengths indicate that at 3 TeV, the total luminosity, as well as the sharpness of the luminosity spectrum for a $\gamma\gamma$ collider are independent of the beam length of the electron beams, given an adequate final focus system and that the hourglass effect is avoided. The total luminosity can

consequently be maximised by minimising the horizontal and vertical beta functions $\beta^*_{x,y}$ at the interaction point.

Furthermore, we perform background studies for both collider types using GUINEA-PIG. Simulation results indicate that our proposed parameter set for a 3 TeV PWFA $\gamma\gamma$ collider is able to deliver a total luminosity significantly higher than a $\gamma\gamma$ collider based on CLIC parameters, but gives rise to more background particles. The examined $\gamma\gamma$ collider parameter sets are able to deliver significantly larger total luminosities than the e^+e^- collider parameter sets considered in this thesis, but result in comparatively larger luminosity spreads. The examined parameter sets for 3 TeV and 14 TeV e^+e^- colliders offer interesting improvements over the CLIC parameter set in terms of luminosity and beam power, but also suffer from strong backgrounds.

Preface

This thesis is submitted in partial fulfilment of the requirements for the degree of *Philosophiae Doctor* at the European Organization for Nuclear Research and University of Oslo. The research presented here is conducted under the supervision of Dr Daniel Schulte and Prof Erik Adli.

Jian Bin Ben Chen
Geneva, Switzerland
October 2020

Acknowledgments

Towards the end of my master's studies at the Norwegian University of Science and Technology, I had the fortune of meeting CERN's representatives at a career evening, which eventually led to a campus canteen. After sharing a few slices of pizzas, some bottles of beers (all paid by CERN, believe it or not) and a conversation about pentaquarks, I was suddenly in possession of an e-mail address for a CERN employee with knowledge about relevant PhD positions. One thing led to another, and before I could say "accelerate", I was standing at Geneva Airport with a suitcase in each hand about to embark on an adventure at the world's largest laboratory for particle physics research – a dream that I carried since I first got a real taste for physics.

Speaking of first motivations, I have to thank my upper secondary school teachers Knut Askeland and Kåre Håland not only for their extraordinary pedagogical abilities, but also for their encouragement and wisdom, which instilled in me a desire to pursue a scientific career. They were the wizards who motivated this hobbit to leave the rolling hills and little rivers of his hometown behind and venture into the world ahead, where the many wonderful friends and colleagues encountered along the path have all made the journey memorable through their kindness, support and inspiration. In particular, I would like to thank my supervisors Dr Daniel Schulte and Prof Erik Adli, whose directions have been insightful, advice have been inspiring and support have been encouraging. Even during days when solving problems felt like decapitating the mythical creature hydra, their patience and support have been exceptional.

I am very grateful to have had the privilege of being part of the unique CERN community, which has been a source of awe and inspiration. It is intriguing to think that such an impressive assembly of resources and talents across nationalities, cultures and professions exists simply because of our human curiosity. Curious about our origin, curious about the fate of the Universe and curious about questions that we yet have to formulate. After 13.8 billion years, this is perhaps one of the most peculiar accomplishments of matter and the fundamental laws of physics – a collaboration enabling collections of fundamental particles to understand their past and postulate their future.

Lastly, I would like to express my gratitude for my family and relatives, who have tirelessly and unconditionally supported, encouraged and believed in me throughout the entire journey.

Contents

Nomenclature

Physics Constants

α	Fine structure constant	
$\hbar$	Dirac's constant	$6.582\,119\,569 \cdot 10^{-16}\,\mathrm{eV\,s}$
μ_0	Permeability in vacuum	$1.256\,637\,062\,12 \cdot 10^{-6}\,\mathrm{H/m}$
ε_0	Permittvity in vacuum	$8.854\,187\,812\,8 \cdot 10^{-12}\,\mathrm{F/m}$
c	Speed of light in vacuum	$299\,792\,458\,\mathrm{m/s}$
e	Elementary charge	$1.602\,176\,634 \cdot 10^{-19}\,\mathrm{C}$
h	Planck's constant	$4.135\,667\,696 \cdot 10^{-15}\,\mathrm{eV\,s}$
m_e	Electron rest mass	$0.510\,998\,95\,\mathrm{MeV/c^2}$

Beam dynamics

$\alpha_{x,y}$	Horizontal/vertical optical function
$\beta_{x,y}$	Horizontal/vertical beta function
$\boldsymbol{\mathcal{W}}$	Wakefield
$\boldsymbol{A}$	Magnetic vector potential
$\boldsymbol{B}$	Magnetic field/magnetic flux density
$\boldsymbol{E}$	Electric field
$\boldsymbol{J}$	Current density

$\mathscr{E}$	Energy
η	Efficiency
$\gamma_{x,y}$	Horizontal/vertical gamma function
Λ	Normalised amplitude
λ	Longitudinal beam particle position distribution
μ	Betatron phase
ϕ	Electric potential
Ψ	Density function
ψ	Pseudo potential
ρ	Charge density
$\sigma_{\mathscr{E}}$	rms energy deviation
σ_z	rms beam length
$\sigma_{x,y}$	rms horizontal/vertical beam size
Θ	Heaviside step function
λ	Wavelength
$\varepsilon_{\mathrm{N}x,y}$	Normalised horizontal/vertical emittance
$\varepsilon_{x,y}$	Horizontal/vertical emittance
H	Hamiltonian
k_{p}^{-1}	Plasma skin depth
n_{b}	Beam particle position distribution
W	Wake function
X	Beam slice mean transverse offset
Y	Betatron growth parameter

Particle collider

$\beta^*_{x,y}$ Horizontal/vertical beta function at IP

η_γ Conversion efficiency

$\mathcal{L}$ Total/instantaneous luminosity

Ω Photon polarisation

σ_c Total cross section for inverse Compton scattering

$\sigma^*_{x,y}$ Horizontal/vertical beam size at IP

$\sqrt{s}$ Centre of mass energy

Υ Beamstrahlung parameter

ϱ Normalised distance between IP and conversion region

A Laser pulse energy

f_r Repetition frequency

h_e Electron helicity

n_γ Number of emitted photons per electron during collision

N_b Number of beams in a pulse

Other Symbols

θ Polar angle

φ Azimuthal angle

ξ Co-moving longitudinal coordinate

s Propagation distance

z Lab frame longitudinal coordinate

CHAPTER 1

Introduction

1.1 High-energy physics – Quo vadis?

"As a layman I would now say I think we have it." With these words, CERN's Director-General Rolf-Dieter Heuer proclaimed the discovery of a Higgs-like particle on 4 July 2012, which was the result of a 40-year search. In March 2013, the ATLAS and CMS collaborations announced that the newly discovered particle indeed has properties consistent with those of the Higgs boson predicted by the Standard Model of particle physics [1, 2].

The Standard Model of particle physics is currently our best understanding of fundamental particles and their interactions. Developed in the early 1970s, it describes fundamental particles in the language of quantum field theory, where both matter particles (fermions) and force carriers (bosons) are manifestations of fundamental quantum fields. The matter particles are divided into leptons and quarks, while the force carrying bosons mediate three of the four fundamental forces, along with the Higgs boson that gives particles their masses through the Brout-Englert-Higgs mechanism [3, 4, 5, 6].

The Standard Model has been remarkably successful in providing predictions that have later been confirmed experimentally. One of the most notable demonstrations is being able to predict the electron magnetic moment with an accuracy of one part in a trillion. Furthermore, in addition to the Higgs boson, the Standard Model predicted the existence of particles such the gluon, top and charm quarks and the W and Z bosons, all of which have been later experimentally confirmed.

Experiments at high energies are often required for the discovery of new particles, which

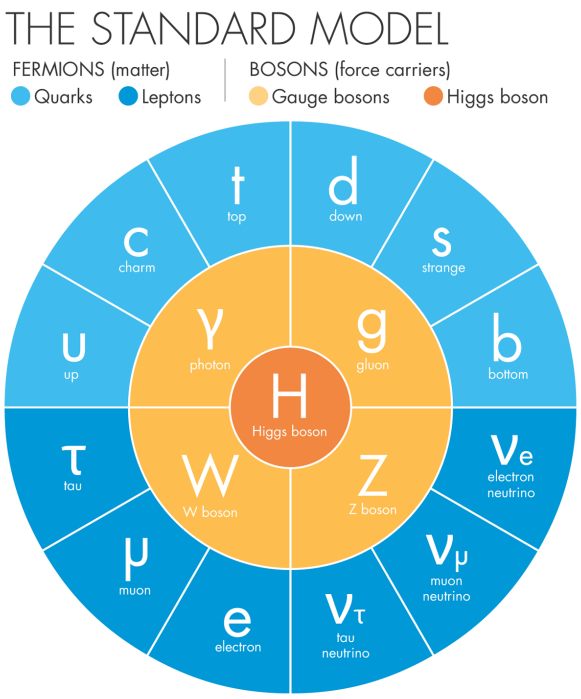

Figure 1.1: The fundamental particles of the Standard Model of Particles physics. The outer shell consists of the 12 fermions divided into quarks and leptons, followed by the four force carriers in the middle shell mediating the electromagnetic force (photon), the strong nuclear force (gluon) and the weak nuclear force (W and Z bosons). Lastly, the Higgs boson in the middle is the mediator for the Brout-Englert-Higgs field which gives particles their masses. Source: Quanta magazine.

is why particle colliders have proven to be invaluable tools for subatomic physics. Notable discoveries using particle colliders include the antiproton at the Berkeley Bevatron in 1955 [7], the muon-neutrino at the Alternating Gradient Synchrotron at Brookhaven National Laboratory (BNL) in 1962 [8], the charm quark at BNL and Stanford Linear Accelerator Center (SLAC) in 1974 [9, 10], the gluon at Deutsches Elektronen-Synchrotron (DESY) in 1979 [11, 12], the W and Z bosons at CERN's Super Proton Synchrotron in 1983 [13, 14] and most recently, the discovery of the Higgs boson in 2012 at CERN's Large Hadron Collider (LHC) [15, 16].

However, despite all the triumphs of the Standard Model, it clearly does not offer a complete description of fundamental interactions, as many questions have yet to be answered. First of all, since there are no accepted or verified quantum theory of gravity, the Standard Model does not include gravitation. Secondly, it does not propose any dark matter candidates possessing properties deduced from observational cosmology. Other challenges include the matter-antimatter asymmetry, non-zero neutrino masses and the accelerating expansion rate of the Universe.

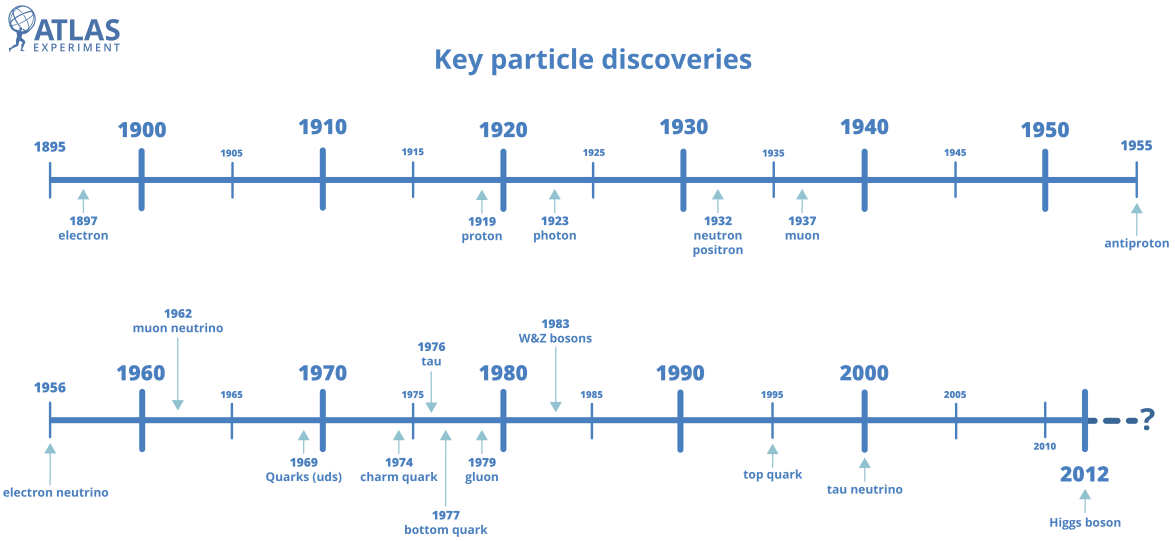

Figure 1.2: Key particle discoveries timeline. Source: ATLAS Experiment © 2019 CERN.

The LHC is currently the most powerful particle collider in the world capable of reaching an energy level of 14 TeV. As a hadron collider, it is designed to be a discovery machine capable of sweeping over a large range of energy levels, but as it so far has failed to discover any particle heavier than the top quark (179 GeV), attention is being gradually shifted to precision machines based on leptons.

1.2 Particle accelerators and colliders

Considering past discoveries, particle accelerators and colliders are arguably the most important workhorses of high-energy physics, and their development is closely related to the quest for gaining understanding of the fundamental building blocks of the Universe. As outlined by the Livingston plot in figure 1.3, progression in high-energy physics requires ever more powerful particle colliders able to collide fundamental particles at progressively higher energies, as well as other performance improvements. This has resulted in particle accelerators and colliders becoming increasingly sophisticated machines with correspondingly large footprints and price tags. Nevertheless, the basic principles for acceleration are trivial and can promptly provide some insights into the development of particle accelerators.

1.2.1 Acceleration principles

Amongst the four fundamental forces of nature, only the electromagnetic force is suitable for particle acceleration, as gravity is too weak, the range of the strong nuclear force is too small and the weak nuclear force has a weak relative strength and short range.

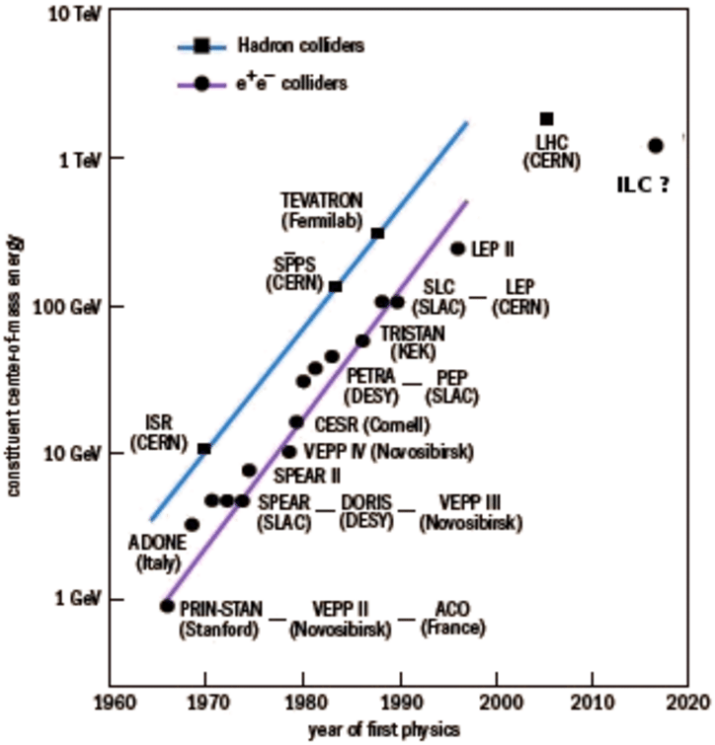

Figure 1.3: Livingston plot showing the centre of mass energy of several particle colliders vs. time. Energies for hadron colliders have been adjusted to account for quark and gluon constituents. Adapted from reference [17].

A particle with charge q and velocity $\boldsymbol{v}$ propagating in a region with electric field $\boldsymbol{E}$ and magnetic field $\boldsymbol{B}$ is affected by the Lorentz force

$$\boldsymbol{F} = q(\boldsymbol{E} + \boldsymbol{v} \times \boldsymbol{B}). \tag{1.1}$$

As the term $\boldsymbol{v} \times \boldsymbol{B}$ is always perpendicular to the direction of motion, only the electric field perform work on the particle. The change in energy for a particle moving from $\boldsymbol{r}_1$ to $\boldsymbol{r}_2$ is hence

$$\Delta\mathscr{E} = q \int_{\boldsymbol{r}_1}^{\boldsymbol{r}_2} \boldsymbol{E} \cdot \mathrm{d}\boldsymbol{r}. \tag{1.2}$$

Even though magnetic fields cannot be used to increase the energy of the particles, they are used to steer, bend and focus charged particle beams.

1.2.2 High-energy particles in particle colliders

The need for high-energy particles in particle physics experiments originates from two requirements. The first requirement is related to resolution. When examining subatomic structures, a probe that is able to resolve the structure is required, which means that one needs a wave whose wavelength λ is small compared to the size of the structure.

The relation between a particle's energy $\mathscr{E}$ and its wavelength is given by de Broglie wavelength

$$\lambda = \frac{hc}{\mathscr{E}}, \tag{1.3}$$

where h is Planck's constant and c is the speed of light in vacuum. Relevant structures typically have sizes $< 10^{-15}\,\mathrm{m}$, which requires probe particles with energy $> 1\,\mathrm{GeV}$ to resolve the structure.

The second requirement is given by the threshold energy for particle production. Let $p_1^\mu = (\mathscr{E}_1/c, \boldsymbol{p}_1)$ denote the four-momentum of an accelerated particle with rest mass m_1, $p_2^\mu = (\mathscr{E}_2/c, \boldsymbol{p}_2)$ be the four-momentum of a target particle with rest mass m_2 and M be the total rest mass of all particles after collision. For a fixed target experiment, accelerated particles are collided into a target at rest, so that the inner product of the total four-momentum $P^\mu = p_1^\mu + p_2^\mu$ before collision is

$$P^\mu P_\mu = (m_1^2 + m_2^2)c^2 + 2\mathscr{E}_1 m_2. \tag{1.4}$$

Conservation of four-momentum leads to the threshold energy

$$\mathscr{E}_1 = \frac{(M^2 - m_1^2 - m_2^2)c^2}{2m_2}. \tag{1.5}$$

Alternatively, particle 2 can also be accelerated and collided head on with particle 1. The inner product of the total four-momentum is now

$$P^\mu P_\mu = (m_1^2 + m_2^2)c^2 + 2\left(\frac{\mathscr{E}_1\mathscr{E}_2}{c^2} + p_1 p_2\right). \tag{1.6}$$

For comparison, this shows that the centre of mass energy scales as $\mathscr{E}_{\mathrm{CM}} = \sqrt{s} \sim \sqrt{4\mathscr{E}_1\mathscr{E}_2}$ for head on collisions[i], while it scales as $\mathscr{E}_{\mathrm{CM}} \sim \sqrt{2\mathscr{E}_1 m_2}$ for a fixed target experiment.

For $\mathscr{E}_1 = \mathscr{E}_2 = \mathscr{E}$, $\boldsymbol{p}_2 = -\boldsymbol{p}_1$ and $p_1, p_2 \gg m_1, m_2$, the threshold energy for head on collisions is

$$\mathscr{E} = \frac{c^2}{2}\sqrt{M^2 - m_1^2 - m_2^2}, \tag{1.7}$$

which scales more favourably with M than in the case of a fixed target experiment. Colliding particle beams however requires the colliding beams to be focused to small sizes in order to maximise chances of collision.

1.2.3 Luminosity

In addition to high-energy particles, a particle collider also needs to ensure high collision rates. In a particle collider, the production rate of particles through a physical process

[i] $p_1, p_2 \gg m_1, m_2$

with interaction cross-section σ_{p} is given by the relation

$$\frac{\mathrm{d}N_{\mathrm{p}}}{\mathrm{d}t} = \sigma_{\mathrm{p}}\mathcal{L}, \tag{1.8}$$

where $\mathcal{L}$ is the luminosity[ii]. The luminosity is a measure of the collider's ability to force beam particles through a given area in a given time, and is hence dependent on the accelerator parameters. Processes studied in modern particle physics experiments typically have very small interaction cross-sections, so that high luminosities are required in order to complete measurements within a reasonable time frame.

For collisions of two pulses containing N_{b} equally spaced Gaussian beams arriving at the interaction point (IP) with repetition frequency f_{r}, the luminosity is given by

$$\mathcal{L} = \frac{N_1 N_2}{4\pi\sigma_x^*\sigma_y^*} N_{\mathrm{b}} f_{\mathrm{r}}, \tag{1.9}$$

where σ_x^*, σ_y^* are the horizontal and vertical beam sizes at the IP and N_1, N_2 are the number of particles in the colliding beams. Luminosity given by equation (1.9) is often termed the geometric luminosity.

In an $\mathrm{e}^+\mathrm{e}^-$ linear collider, the particles of each beam are focused by the other beam, which leads to a pinch-effect that increases luminosity. This enhancement is measured by the enhancement factor H_{D}, and the total luminosity is given by

$$\mathcal{L} = H_{\mathrm{D}} \frac{N_1 N_2}{4\pi\sigma_x^*\sigma_y^*} N_{\mathrm{b}} f_{\mathrm{r}}. \tag{1.10}$$

H_{D} is typically in the range 1–2 and is generally calculated using simulation codes such as CAIN [18] or GUINEA-PIG [19].

This can also be written in the form

$$\mathcal{L} = H_{\mathrm{D}} \frac{N_2}{4\pi\sigma_x\sigma_y} \frac{P_{\mathrm{b}}}{\mathscr{E}_{\mathrm{b}}}, \tag{1.11}$$

where $P_{\mathrm{b}} = N_{\mathrm{b}} f_{\mathrm{r}} N_1 \mathscr{E}_{\mathrm{b}}$ is the beam power per beam, $\mathscr{E}_{\mathrm{b}}$ is the beam energy and N_1 is chosen to be the largest number of N_1, N_2 in this thesis.

1.2.4 Circular collider

Beams in a circular collider are steered to follow a circular orbit using dipole magnets and accelerated every time they pass through the accelerating section of the collider. After the desired energy is reached, colliding beams that have been circulating in different beam

[ii] We will later refer to this quantity as the total luminosity, but the term instantaneous luminosity is also common.

pipes in the opposite direction with respect to each other are brought into collision at the IP of the colliders, where the collisions are studied using particle detectors. Particles that did not collide, are recycled, where they will again be brought into collision at the next cycle. This is repeated until the beam intensities have been reduced below a certain level.

The footprint of a circular collider can be estimated based on the field strength B of the dipole magnets and the momentum p of the particles with the relation

$$R = \frac{p}{qB}, \tag{1.12}$$

where R is the bending radius. The currently largest circular collider in the world is CERN's LHC, with a circumference of 27 km. The LHC is capable of accelerating and colliding protons at 6.5 TeV and ions at 2.5 TeV per nucleon. Each fill consists of roughly 10^{14} protons grouped into beams that circulate for 1–35 hours, during which there are about 600 million collisions per second.

1.2.5 Linear collider

In principle, one can set up a static electric field between two electrodes and use it to accelerate charged particles between the electrodes. However, due to electric breakdowns, the maximum energy gain is often limited to a few MeV. Instead, modern linear accelerators use radio frequency (RF) cavities to accelerate particles over long distances. This idea was first proposed by Gustav Ising in 1925 and first successfully tested by Rolf Widerøe in 1928.

Ising's concept was to use a series of metallic drift tubes with varying lengths separated by gaps (illustrated in figure 1.4) and connected with alternating polarities to a RF supply. The RF supply generates a high-frequency alternating voltage in the gaps that accelerate the charged particles for half a RF period, after which the particles will arrive in a drift tube before the direction of RF electric field is reversed. During the decelerating half period, the particles will be inside a drift tube, which acts as a Faraday cage to shield the particles from unwanted external fields. When the particles enter the next gap, they will again undergo acceleration, and this can in principle be repeated to reach arbitrarily high energies.

However, such an acceleration and shielding process clearly requires the separation between the gaps to be matched to the energy of the particles and the RF frequency, which requires the separation lengths to increase as the particles gain energy in the gaps. This may thus lead to large structures and high costs. Since the major part of a linear collider consists of linear accelerators, its footprint can be estimated by the relation

$$L = \frac{\mathscr{E}_{\mathrm{CM}}}{qE_z}, \tag{1.13}$$

where E_z is the average accelerating electric field, i.e. the accelerating gradient. The footprint can thus be reduced by using a larger accelerating gradient, but the metallic acceleration cavities in conventional accelerators are limited by electric breakdown.

In a linear collider, beams after collision cannot be reused for subsequent collisions, which sets a more stringent requirement on luminosity and efficiency for linear colliders compared to circular colliders.

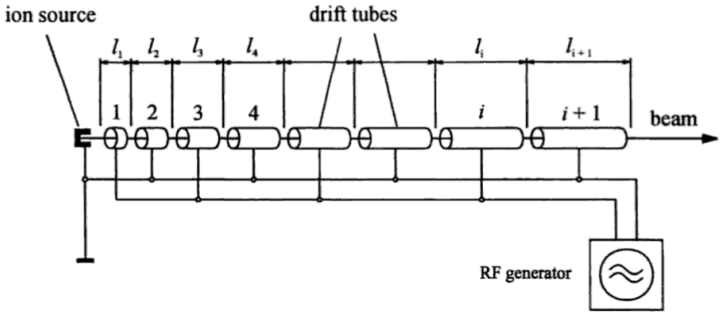

Figure 1.4: Sketch of the Widerøe linear accelerator. Source: [20].

The largest constructed linear collider in the world was SLAC's 3 km Stanford Linear Collider (SLC) capable of colliding electrons and positrons at 90 GeV centre of mass energy. It ceased operation in 1989 and has been re-purposed and divided into 3 separate 1 km linear accelerators.

1.2.6 Future collider considerations

Since hadrons consist of quarks and gluons with unknown energy and momentum distributions, the achievable precision is limited. Leptons, on the other hand, are elementary particles with well-defined initial states and can achieve higher precision measurements. Therefore, there has been a gradual shift in focus from high-energy discovery machines based on hadrons to precision machines based on lepton collisions.

An electron-positron collider can produce Higgs bosons in a clean environment that enables model-independent determination of the absolute Higgs couplings to fermions and to gauge bosons through the Higgsstrahlung and WW-fusion processes [21, 22]. The focus on lepton colliders is reflected in the European Strategy for Particle Physics, which has identified an electron-positron Higgs factory as the highest priority next collider [23, 24].

A circular collider can in principle be used to collide leptons, examples of which include VEPP II–IV, PETRA, SuperKEKB, Beijing Electron-Positron Collider II (BEPC II) and LHC's predecessor Large Electron Positron collider (LEP). However, due to synchrotron radiation, a circular lepton collider is limited in collision energy. For a charged particle with charge e, rest mass m and energy $\mathscr{E}$ circularly accelerated in an orbit with bending

radius R, the radiated power via synchrotron radiation is [25]

$$P = \frac{e^2}{6\pi\varepsilon_0 c^7} \frac{\mathscr{E}^4}{m^4 R^2}. \tag{1.14}$$

Since this scales as $1/m^4$, electrons/positrons lose energy at a rate that is $1.13 \cdot 10^{13}$ times faster than protons. At high energies, the energy loss of electrons/positrons cannot be compensated in a feasible way, which is why linear accelerators are needed for accelerating light particles such as electrons and positrons in order to reach high energies in the multi-TeV scale.

Current proposed linear colliders include the 20–50 km International Linear Collider (ILC) [26] and the 11–50 km Compact Linear Collider (CLIC) [27], which are designed to collide electrons and positrons at 0.25–1 TeV and 0.38–3 TeV respectively. In addition, several circular colliders have also been proposed. This includes the 100 km Future Circular Collider (FCC) [28, 29] aiming to reach 100 TeV of proton collision energy and the 100 km Circular Electron Positron Collider (CEPC) [30] designed to collide electrons and positrons at 240 GeV centre of mass energy.

A common trait for these colliders is their titanic sizes, with estimated costs of tens of billions of euros. In view of the ever-increasing size and cost, it is clear that innovation in acceleration technology is crucial, if the field of high-energy physics is to survive in the long term. After all, acceleration technology has largely remained unchanged for several decades.

1.3 Novel acceleration techniques

Conventional acceleration technology is based on metallic cavities resonantly driven by RF electromagnetic fields. L- and S-band cavities are driven by 1–4 GHz RF-fields and can sustain electric fields up to 20 MV/m before breakdown occurs. CLIC uses 12 GHz X-band cavities able to sustain acceleration gradients up to 100 MV/m. This is currently the highest achievable acceleration gradient using conventional acceleration technology [31], and would still require tens of kilometres of acceleration structure to reach TeV energy levels. As indicated by the 3 TeV CLIC layout in figure 1.5, the main linacs (linear accelerator) occupy a major part of the collider length.

Thus, novel acceleration technologies able to reach higher gradients are crucial for shortening the length of the main linacs and hence also reducing the footprint of the linear collider. The Advanced LinEar collider study GROup (ALEGRO) was formed at the initiative of the International Committee for Future Accelerators (ICFA) to cultivate research on advanced accelerator concepts for application in high-energy physics. ALEGRO is an international community of researchers from universities and accelerator laboratories[iii] whose long-term goal is to design the Advanced Linear International Collider

[iii] CERN, DESY, INFN-LNF (Istituto Nazionale di Fisica Nucleare-Laboratori Nazionali di Frascati),

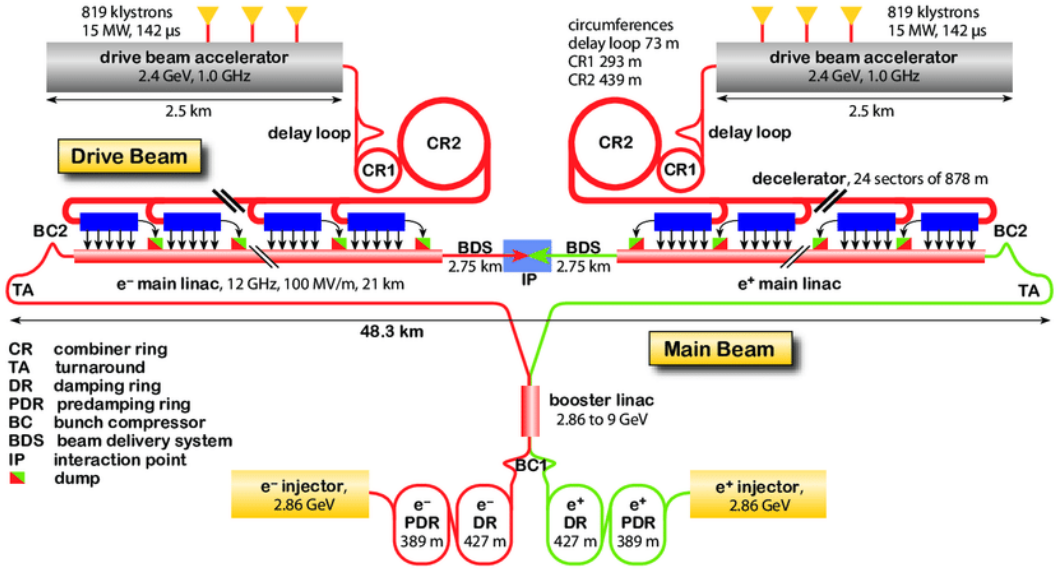

Figure 1.5: CLIC layout at $\sqrt{s} = 3\,\text{TeV}$. Source: reference [27].

(ALIC), an $e^+/e^-/\gamma$ collider with up to 30 TeV in the centre of mass energy.

The main purpose of advanced accelerator research is to study acceleration mechanisms that can provide space- and energy efficient acceleration using large acceleration gradients, while maintaining a high beam quality. Currently, the main acceleration media being studied are dielectric materials and plasma, due to their ability to sustain electric fields on the order of GV/m or higher. Two drivers commonly used to excite accelerating electric fields in these media are high-powered lasers and high-current charged particle beams, which gives four combinations between driver and medium. Of the four options, beam-driven plasma wakefield acceleration (PWFA) is able to sustain larger accelerating fields than the dielectric options and is more power efficient than laser wakefield acceleration[iv] [34], and is the main focus of this thesis.

The 3 TeV CLIC parameter set [27] is the main parameter set used to benchmark the performance of PWFA parameters that we will derive in this thesis. Relevant parameters from the 3 TeV CLIC parameter set are summarised in table 1.1.

1.3.1 Beam-driven plasma wakefield acceleration

In PWFA, an ultra-relativistic electron drive beam sent into an initially uniform plasma will repel plasma electrons away from the beam axis. After the drive beam has passed by, the attracting forces from the background ions will pull the plasma electrons back

PSI (Paul Scherrer Institut), ANL, LBNL (Lawrence Berkeley National Laboratory), BNL and SLAC.

[iv] In e.g. CLIC, particle beams can be produced and accelerated with a wallplug-to-beam power efficiency of around 60 % [32], while the wallplug-efficiency of high-powered laser systems are typically less than 0.1 % [33].

Parameter	Symbol	Unit	Value
Centre of mass energy	$\sqrt{s}$	TeV	3.0
Acceleration gradient	E_z	MV/m	100
Total linac length	L_{linac}	km	42.16
Particle number per beam	N	10^9	3.72
Number of beams per pulse	N_{b}		312
Repetition rate	f_{r}	Hz	50
rms beam length	σ_z	µm	44
Horizontal beta function at IP	β_x^*	mm	6.9
Vertical beta function at IP	β_y^*	mm	0.068
Normalised horizontal emittance	$\gamma\varepsilon_x$	mm mrad	0.66
Normalised vertical emittance	$\gamma\varepsilon_y$	mm mrad	0.02
Wall plug to main beam efficiency	η_{tot}	%	7
Beam power per beam	P_{b}	MW	14
Luminosity	$\mathcal{L}$	$10^{38}\,\text{m}^{-2}\,\text{s}^{-1}$	5.9
Peak luminosity	$\mathcal{L}_{0.01}$	$10^{38}\,\text{m}^{-2}\,\text{s}^{-1}$	2

Table 1.1: 3 TeV CLIC parameters.

towards the axis and set up a density oscillation. This oscillation is known as the plasma wake, and a trailing beam placed at the correct phase of the wake can extract energy from the wake and be accelerated. Such a two-beam plasma acceleration scheme was first demonstrated at Argonne National Laboratory (ANL) in 1988 [35].

Assuming electric fields of the form $\boldsymbol{E} \sim \boldsymbol{E}_0 \exp(-i\omega_{\text{p}} z/c)$ and applying Gauss's law, we obtain an estimate for the typical field strength

$$E_0 = \frac{m_{\text{e}} c \omega_{\text{p}}}{e} = \sqrt{\frac{m_{\text{e}} c^2 n_0}{\varepsilon_0}}, \tag{1.15}$$

where $\omega_{\text{p}} = \sqrt{e^2 n_0/(\varepsilon_0 m_{\text{e}})}$ is the plasma angular frequency and n_0 is the plasma particle number density. For a typical plasma density of $n_0 = 10^{16}\,\text{cm}^{-3}$, we obtain an electric field of 10 GV/m. Proof of concept PWFA experiments have demonstrated large accelerating gradients of more than 50 GV/m [36] and an energy transfer efficiency that can exceed 30 % [37], but space- and energy efficient acceleration of beams with collider-grade beam quality have yet to be demonstrated.

In order to be able to compete with conventional RF technology, novel plasma acceleration technology must be able to provide similar beam quality and efficiency, while offering a larger acceleration gradient. One of the main detrimental effects leading to beam quality deterioration is transverse wakefields, which may lead to transverse instabilities. Such transverse instabilities can restrict the maximum beam charge that can be accelerated and thus also constrain the efficiency of the accelerator. Hence, transverse instabilities and

their mitigation mechanisms are considered by the community to be amongst the most important challenges to be addressed towards developing a high-energy, high-efficiency, high beam brightness PWFA electron accelerator [32, 38]. Other challenges such as positron acceleration, coupling between plasma stages, preservation of emittance, high repetition rate plasma acceleration and energy deposition in the plasma sources have been identified in a number of papers, workshops and strategy sessions [39, 40, 41, 42, 43, 44].

This thesis applies formalism used in conventional linear collider studies to model the transverse wakefields and transverse instabilities in PWFA to perform parameter studies on the efficiency constrain. The wakefield model is also benchmarked against particle-in-cell simulations.

1.3.2 Plasma sources in PWFA facilities

Plasma source development for PWFA applications is currently focusing on density uniformity, density reproducibility, beam energy spread minimisation, high repetition rate (kHz-level) and long operation time (months). Common plasma sources used in current PWFA experiments include alkali-metal vapour sources, gas cells, electrical discharges and capillary discharges [43, 44].

Plasma sources used by some current and planned PWFA facilities are summarised in table 1.2.

Facility	**Plasma species**	**Source type**	**Density** [cm^{-3}]	**Length** [cm]
AWAKE	Rb	Vapour	10^{14}–10^{15}	1000
CLEAR	Ar, He	Capillary	10^{16}–10^{18}	5–20
FACET-II	Li	Pipe oven	10^{15}–10^{18}	10–100
FLASHForward	H, N	Gas cell	10^{15}–10^{18}	1–30
SPARCLAB	H	Capillary	10^{16}–10^{18}	3
EuPRAXIA	H	Capillary	10^{16}–10^{18}	> 30
CLARA	He	Capillary	10^{16}–10^{18}	10–30
MAX IV	H	Gas cell	10^{15}–10^{18}	10–50

Table 1.2: Plasma source overview for some current and planned PWFA facilities.

Relative density uniformity of less than 1% has been demonstrated in metal vapour sources in e.g. AWAKE [45] and rms energy spread of a few percent has been measured in reference [37, 46]. Issues such as high repetition rates, long operation times and dissipation of energy not extracted by the main beam are still considered major challenges in plasma source development.

1.3.3 The positron challenge

While conventional RF accelerators can accelerate both electrons and positrons by simply using appropriate phases of the RF field, the plasma response can be charge asymmetric due to the large difference in plasma electron mass and plasma ion mass. This leads to serious challenges in achieving simultaneous acceleration and focusing of positron beams, especially in the non-linear regime, where the accelerating structures consist of plasma ion bubbles with expelled plasma electrons concentrated in thin sheaths around the bubbles (see chapter 2). The non-linear regime has many ideal properties for electron acceleration, but the regions that are simultaneously accelerating and focusing for positrons are much smaller than the corresponding regions for electrons. In addition, the accelerating field has a very steep slope in these regions, and both the focusing and accelerating fields vary transversely, which can lead to large energy spreads and beam quality degradation.

Several alternative schemes have been proposed to address the challenge of positron acceleration in plasma. Examples include:

- The linear/quasi-linear regime of PWFA (see chapter 2) has a charge symmetric response, but has non-linear focusing fields that lead to beam quality degradation.

- Doughnut-shaped drivers can be used to shape the wakefields in the non-linear regime to obtain linear focusing fields and strong positron accelerating fields [47]. The generation and preservation of such beams are however challenging,

- Hollow channel plasmas makes use of plasma tubes where there is no plasma in the centre, and thus avoid positron being defocused by background ions. This can provide large accelerating fields, but no focusing fields, which makes this acceleration scheme very susceptible to transverse instabilities. In addition, in contrast to acceleration using uniform plasma, the symmetry axis is not defined by the drive beam, which introduces additional misalignment and instability challenges. Proof of concept experiments at FACET have demonstrated production of hollow channel plasmas and acceleration of a trailing positron beam using hollow channel plasma [48, 49], but transverse wakefields about 10000 times stronger than those found in CLIC have also been reported [50].

- Recent analytical and numerical studies [51, 52] have demonstrated that using a plasma column with column radius smaller than the maximum ion bubble radius can create a long high-density electron filament at the axis return point. This can enlarge the region that is simultaneous accelerating and focusing for positrons, and the studies have demonstrated that quasi-matched positron beams with tailored current profiles can be combined with this scheme to accelerate high-charge beams with sub-percent relative energy spread and percentage level emittance growth. The feasibility of this scheme remains to be demonstrated experimentally.

Currently, high-gradient, high-efficiency and high beam quality positron acceleration in plasma remain considerably more challenging than electron acceleration.

1.3.4 The photon collider alternative

Photon colliders, or $\gamma\gamma$ colliders, were first proposed in the 1980s as potential extensions to VLEPP and SLC [53, 54]. In the 1990s, $\gamma\gamma$ colliders were suggested as potential add-ons for several high-energy linear colliders such as SLAC's NLC, KEK's JLC and DESY's TESLA, and then saw a decline in interest as ICFA in 2009 rejected the proposal for building a 180 GeV $\gamma\gamma$ collider as an initial step towards a full-scale ILC [55]. A turning point came in 2012 following the discovery of the Higgs boson with the relatively low mass of 125 GeV. $\gamma\gamma$ collisions can produce Higgs bosons through the process $\gamma\gamma \to \mathrm{H}$, which has a cross section that is comparable to the that of the $\mathrm{e^+e^-} \to \mathrm{ZH}$ process. The required energy for a photon beam is however only 63 GeV, compared to 120 GeV for an electron beam [55].

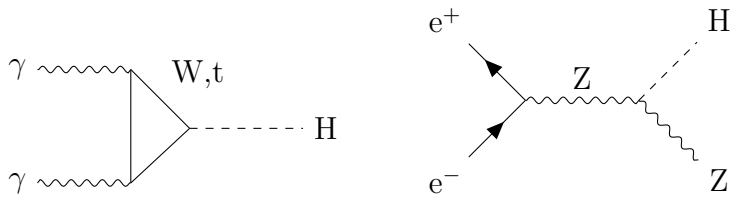

(a) $\gamma\gamma \to \mathrm{H}$. **(b)** $\mathrm{e^+e^-} \to \mathrm{ZH}$.

Figure 1.6: Feynman diagrams for common Higgs production processes in $\gamma\gamma$ and $\mathrm{e^+e^-}$ collisions.

As the path for stable and efficient positron acceleration in plasma remains unclear, further attention has been given to photon colliders as PWFA $\gamma\gamma$ colliders could potentially be a viable alternative to PWFA $\mathrm{e^+e^-}$ colliders. Photon colliders circumvent the positron acceleration challenge and use high-energy electron beams accelerated by PWFA to increase the energies of laser photons through inverse Compton scattering in a conversion region located shortly upstream of the IP. Back-scattered photons will be boosted to energies close to the electron energies, and are collided against an opposite photon beam in the IP.

At high energies a $\gamma\gamma$ collider has a comparable discovery potential as a $\mathrm{e^+e^-}$ collider for processes involving charged products [56], with cross sections for pairs of scalars, fermions or vector particles all being significantly larger in $\gamma\gamma$ collisions compared to $\mathrm{e^+e^-}$ collisions, as seen in figure 1.7. A $\gamma\gamma$ collider is however unable to perform model-independent measurements of the Higgs couplings [57], so the results should ideally be combined with those of a sub-TeV $\mathrm{e^+e^-}$ collider, for instance ILC at 250 GeV or CLIC at 380 GeV [58].

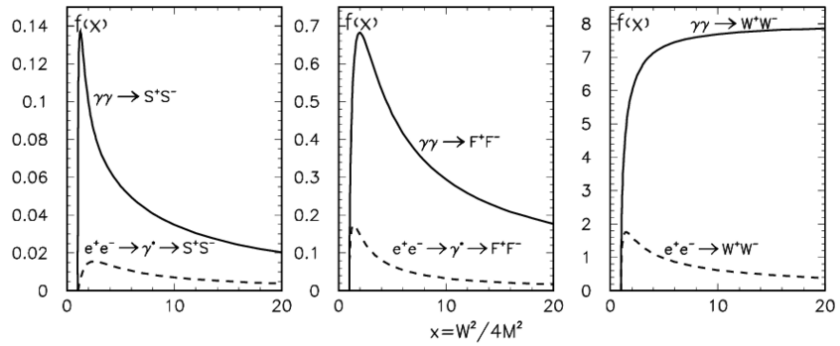

Figure 1.7: Cross sections for pair production of charged scalars (S), fermions (F) and W bosons in $\gamma\gamma$ and e^+e^- collisions [57].

1.4 Thesis outline

This thesis first presents a review of beam dynamics and wakefield theory for the linear and non-linear regimes of PWFA ending with introducing a transverse wake function for the non-linear regime. This wake function is then benchmarked against QuickPIC simulations and incorporated into a simplified quasi-static model used to describe the transverse dynamics of trailing beams in the PWFA non-linear regime in chapter 3. By combining the simplified model with QuickPIC simulations, we perform a parameter scan for a 1.5 TeV PWFA electron accelerator taking the effects of beam loading, energy spread and transverse instabilities into account to derive a parameter set with reasonable energy spread, stability and efficiency. This parameter set then forms the basis for subsequent PWFA e^+e^- and $\gamma\gamma$ collider parameter studies.

After deriving a parameter set able to provide a satisfying acceleration process, the thesis proceeds to optimise main beam parameters at the IP. Optimistically assuming that positrons can be accelerated in a similar manner, the derived PWFA electron accelerator parameter set is adopted in chapter 4 to perform a beam-beam parameter study (using GUINEA-PIG simulations) for a multi-TeV PWFA e^+e^- collider in order to optimise the main beam parameters at the IP with respect to luminosity and luminosity spread introduced by beam-beam effects. Furthermore, chapter 4 also presents background studies and examines asymmetric collision scenarios with reduced numbers of positrons at 3 TeV and 14 TeV.

In chapter 5 we perform a beam-beam parameter study for a 3 TeV $\gamma\gamma$ collider with electron beams accelerated by a 1.5 TeV PWFA electron accelerator. The study is again performed with GUINEA-PIG simulations with electron beam parameters based on the parameter set derived in chapter 3 to optimise beam parameters in the IP.

Lastly, we provide a summary of the thesis in chapter 6, as well as suggestions for future directions.

CHAPTER 2

Beam Dynamics and PWFA Theory

In this chapter, we will give a brief introduction to relevant concepts in beam dynamics and plasma wakefield theory, ending with introducing a transverse wake function for the non-linear PWFA regime. This transverse wake function is benchmarked against simulations and used to model transverse beam dynamics in chapter 3.

2.1 Beam dynamics

Particle motions are described with respect to a nominal trajectory, also referred to as the orbit, given by the design of the accelerator. In circular accelerators, the orbit can have a complicated shape consisting of several sections of curves connected by straight sections with various lengths. The orbit in linear accelerators can simply be a straight line. We introduce a Cartesian co-moving coordinate system $K = (x, y, \xi)$, whose origin follows a reference particle moving along the orbit. With the ξ-axis pointing along the direction of beam propagation, the co-moving coordinate ξ describes a particle's longitudinal position in a beam, while x and y describe transverse motions with respect to the orbit. See figure 2.1 for an illustration.

2.1.1 Relativistic space charge cancellation

We will here show that the space charge forces are rapidly suppressed as the particle beam approaches the ultra-relativistic limit. For a cylindrical beam with constant charge density ρ, the radial electric field inside the beam is

$$E_r = \frac{\rho}{2\varepsilon_0} r, \tag{2.1}$$

where ε_0 is the permittivity in vacuum.

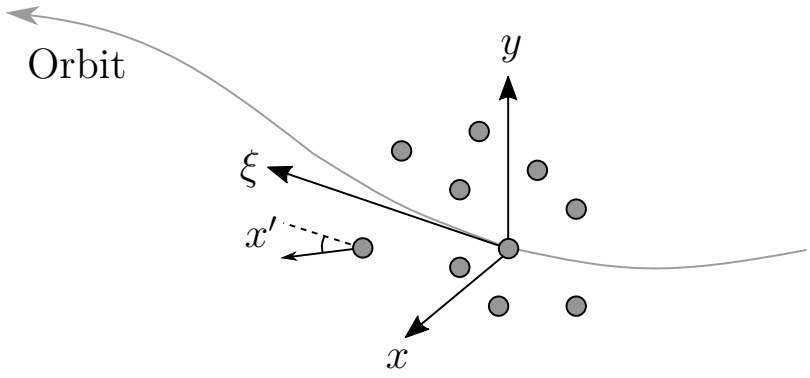

Figure 2.1: Schematics of the co-moving coordinate system used to describe particle motions, whose origin follows the design orbit of the accelerator.

Using Ampere's law, we obtain the azimuthal magnetic field

$$B_\varphi = \frac{\rho v}{2\varepsilon_0 c^2} r, \tag{2.2}$$

where v is the velocity of the beam.

The transverse force acting on a particle with charge q inside the beam is then given by the Lorentz force

$$F_r = q(E_r - vB_\varphi) = \frac{q\rho r}{2\varepsilon_0}\left(1 - \frac{v^2}{c^2}\right) = \frac{q\rho r}{2\varepsilon_0}\frac{1}{\gamma^2}, \tag{2.3}$$

which is suppressed by $1/\gamma^2$, where γ is the Lorentz factor.

Since we are mainly considering electron beams, which can be accelerated rapidly, we assume that $\gamma \gg 1$, so that the entire beam can be considered as an ensemble of non-interacting charged particles.

2.1.2 Single particle transverse dynamics

Even though the space charge forces of particles inside an ultra-relativistic beam can be neglected, the trajectories of individual particles within a beam may still diverge due to inherent angular divergence, which is affected by external electromagnetic fields.

In order to bring transversely offset particles back to the axis and focus the beam, it is common to use a magnetic quadrupole, which can provide a transverse force proportional to the transverse offset. A magnetic quadrupole provides the magnetic field

$$\boldsymbol{B} = gy\hat{\boldsymbol{x}} + gx\hat{\boldsymbol{y}}, \tag{2.4}$$

where $g = \partial B/\partial r$ is the radial magnetic field gradient.

A charged particle with charge q, velocity v and offset x, y is focused by the force

$$\boldsymbol{F} = qvg(-x\hat{\boldsymbol{x}} + y\hat{\boldsymbol{y}}) \tag{2.5}$$

in the x-direction. Since a magnetic quadrupole can only provide a focusing force in one direction, quadrupole magnets that alternate between focusing in the x- and y-direction are placed after each other to achieve net focusing.

In order to derive the equation of transverse motion, we apply Newton's second law in the x-direction. For a particle with mass m, this yields

$$F_x = \frac{\mathrm{d}p_x}{\mathrm{d}t} = \gamma m\ddot{x}. \tag{2.6}$$

It is however more practical to express quantities as functions of the propagation distance s instead of time. The transverse force can thus be written as

$$F_x = \gamma m v^2 x'', \tag{2.7}$$

where a prime denotes differentiation with respect to s.

Assuming that only the magnetic force is acting on the particle, we arrive at Hill's equation.

$$x''(s) + k(s)x(s) = 0, \tag{2.8}$$

where $k(s) = qg(s)/\gamma mv$. This equation has the solution

$$x(s) = \sqrt{\varepsilon_x \beta_x(s)}\cos(\mu(s)), \tag{2.9}$$

and describes a particle undergoing a betatron oscillation with phase

$$\mu(s) = \int_0^s \frac{\mathrm{d}s'}{\beta_x(s')} \tag{2.10}$$

and amplitude $\sqrt{\varepsilon_x\beta_x(s)}$ that depend on the focusing structure along s. The constant ε_x is known as the single particle emittance, while the function $\beta_x(s)$ is termed the beta function.

2.1.3 Emittance and Twiss parameters

The derivative of the trajectory $x(s)$ can be written as

$$x'(s) = -\sqrt{\frac{\varepsilon_x}{\beta_x(s)}}\left[\alpha_x(s)\cos(\mu(s)) + \sin(\mu(s))\right], \tag{2.11}$$

where we have introduced the optical function

$$\alpha_x(s) = -\frac{\beta_x'(s)}{2} \tag{2.12}$$

that represents the x–x' correlation of the beam and contains information about the divergence of the beam.

The phase μ can be eliminated using simple substitution and the identity $\sin^2\theta + \cos^2\theta = 1$ to describe the particle motion in the x–x' trace space plane. This is given by

$$\boxed{\gamma_x(s)x^2(s) + 2\alpha_x(s)x(s)x'(s) + \beta_x(s)x'^2(s) = \varepsilon_x,} \tag{2.13}$$

where

$$\gamma_x(s) = \frac{1 + \alpha_x^2(s)}{\beta_x(s)}, \tag{2.14}$$

and must not be confused with the Lorentz factor γ. The functions α_x, β_x and γ_x are known as the Twiss parameters.

Equation (2.13) describes an ellipse in the x–x'-plane with area $\pi\varepsilon$, and is illustrated in figure 2.2. Liouville's theorem states that the density of particles in phase space is constant with respect to time if the particles obey Hamilton's equations, i.e. when considering a conservative system. This condition is satisfied in a linear magnetic lattice in the non-accelerating parts of an accelerator, and implies that the area of the phase space ellipse and hence that the emittance is invariant of particle motion. The shape and position of the phase space ellipse evolve according to the beta function as the particle moves through the non-accelerating parts of the orbit, but the area remains constant, as illustrated in figure 2.3.

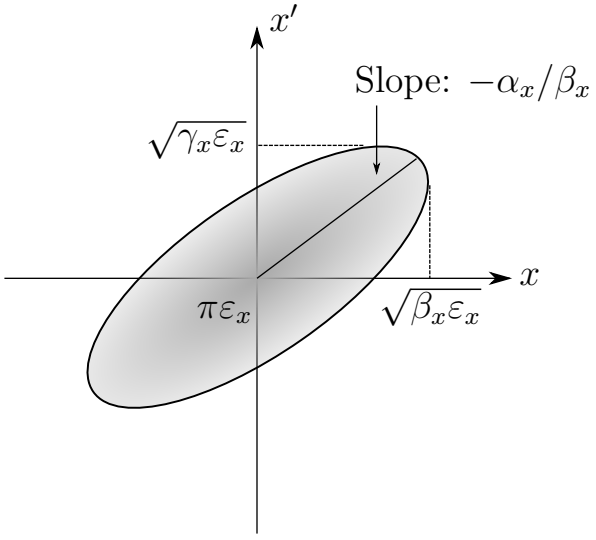

Figure 2.2: The phase space ellipse in the x–x'-plane. Particles on the ellipse have the same emittance, but are in different phases.

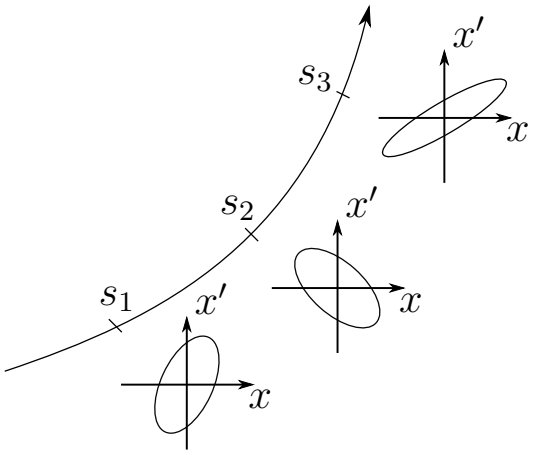

Figure 2.3: Evolution of phase space ellipse in non-accelerating parts of the orbit.

When non-conservative forces such as a RF-field perform work on the particles, the emittance, also termed geometrical emittance, will shrink due to the increase of the

particle momentum. Assuming a high energy beam where $p_z \gg p_x$, the angle that the particle's trajectory forms with the longitudinal axis can be written as

$$x' = \frac{\partial x}{\partial s} \approx \frac{p_x}{p_z} \approx \frac{p_x}{\gamma m v}. \tag{2.15}$$

In order to recover an invariant quantity, the geometrical emittance is multiplied by $\gamma v/c$ to obtain the normalised emittance

$$\varepsilon_{\mathrm{N}} = \frac{v}{c}\gamma\varepsilon, \tag{2.16}$$

which is conserved under acceleration.

2.1.4 Beam description

We have so far only considered single particle dynamics, but each particle moves with different amplitudes corresponding to different trace space ellipses. We must therefore specify what we mean by the average emittance of a particle beam.

A particle beam at a given time can be described as a collection of points in a six-dimensional phase space spanned by the spatial positions (x, y, ξ) and momenta (p_x, p_y, p_z). It is however more convenient to describe the beam in 6D trace space (also referred to as phase space) where $(x, y, \xi, p_x, p_y, p_z) \rightarrow (x, y, \xi, x', y', \mathscr{E})$, where $\mathscr{E}$ is the energy of a particle. The density function $\Psi = \Psi(x, y, z, x', y', \mathscr{E})$ describes the distribution of particles in trace space, so that the number of particles found in a given region of trace space is found by integrating over a that region of trace space

$$\mathrm{d}N = \Psi(\boldsymbol{q}, \boldsymbol{q}')\mathrm{d}^3q\mathrm{d}^3q', \tag{2.17}$$

and we can use the statistical moments of the density function to characterise the beam. For simplicity, we will only consider the x–x'-plane so that $\Psi = \Psi(x, x')$. The mean value is given by the first order moment

$$\langle x \rangle = \int x\Psi(x, x')\,\mathrm{d}x\mathrm{d}x' \tag{2.18}$$

$$\langle x' \rangle = \int x'\Psi(x, x')\,\mathrm{d}x\mathrm{d}x', \tag{2.19}$$

while the variances and correlation are calculated using the second order moments:

$$\langle x^2 \rangle = \int (x - \langle x \rangle)^2\Psi(x, x')\,\mathrm{d}x\mathrm{d}x' \tag{2.20}$$

$$\langle x'^2 \rangle = \int (x' - \langle x' \rangle)^2\Psi(x, x')\,\mathrm{d}x\mathrm{d}x' \tag{2.21}$$

$$\langle xx' \rangle = \langle x'x \rangle = \int (x - \langle x \rangle)(x' - \langle x' \rangle)\Psi(x, x')\,\mathrm{d}x\mathrm{d}x'. \tag{2.22}$$

For Gaussian beams, we can obtain the following relations between the second order moments and the Twiss parameters:

$$\langle x^2 \rangle = \beta_x \varepsilon_{\text{rms}} \tag{2.23}$$
$$\langle x'^2 \rangle = \gamma_x \varepsilon_{\text{rms}} \tag{2.24}$$
$$\langle x x' \rangle = -\alpha_x \varepsilon_{\text{rms}}, \tag{2.25}$$

where ε_{rms} is the rms emittance, i.e. the emittance for particles located one standard deviation σ_x away from the beam axis. We can thus define

$$\sigma_x(s) = \sqrt{\varepsilon_{\text{rms}} \beta_x(s)} \tag{2.26}$$

as the (horizontal) transverse beam size.

Since we can describe the second order moments of a beam of particles using the Twiss parameters, this implies that Gaussian beams are uniquely defined by the Twiss parameters. Furthermore, even though individual particles may have different single particle emittances and phases, they all have the same Twiss parameters. We can thus express the single particle emittance in terms of the Twiss parameters as

$$\varepsilon_x(x, x') = \gamma_x x^2 + 2\alpha_x x x' + \beta_x x'^2. \tag{2.27}$$

As a particle propagates through the accelerator, the particle traverses an ellipse with constant area, where its angular location on the ellipse is given by the phase μ. Assuming that all the particles are uniformly distributed in phase, the corresponding distribution in the x–x'-plane is given by the bi-Gaussian

$$\Psi(x, x') = \frac{1}{2\pi\sqrt{|\boldsymbol{\Sigma}|}} \exp\left(-\frac{1}{2}\boldsymbol{X}^{\mathrm{T}} \boldsymbol{\Sigma}^{-1} \boldsymbol{X}\right), \tag{2.28}$$

where $\boldsymbol{X} = (x, x')^{\mathrm{T}}$ and the sigma beam matrix is given by

$$\boldsymbol{\Sigma} = \begin{pmatrix} \langle x^2 \rangle & \langle x x' \rangle \\ \langle x' x \rangle & \langle x'^2 \rangle \end{pmatrix} = \varepsilon_{\text{rms}} \begin{pmatrix} \beta_x & -\alpha_x \\ -\alpha_x & \gamma_x \end{pmatrix}. \tag{2.29}$$

The rms emittance can be expressed with the determinant of the sigma matrix as

$$\varepsilon_{\text{rms}} = \sqrt{|\boldsymbol{\Sigma}|} = \sqrt{\langle x^2 \rangle \langle x'^2 \rangle - \langle x x' \rangle^2}, \tag{2.30}$$

so that the density function can also be written as

$$\Psi(x, x') = \frac{1}{2\pi\varepsilon_{\text{rms}}} \exp\left(-\frac{1}{2}\frac{\varepsilon(x, x')}{\varepsilon_{\text{rms}}}\right). \tag{2.31}$$

2.1.5 Beam size matching

The beta function is given by the equation

$$\frac{1}{2}\beta_x(s)\beta_x''(s) - \frac{1}{4}\beta_x'^2(s) + k(s)\beta_x^2(s) = 1, \tag{2.32}$$

which is obtained by inserting the solution for $x(s)$ into Hill's equation. An alternative way for describing the evolution of the transverse beam size is by using the envelope equation

$$\sigma_x''(s) + k(s)\sigma_x(s) = \frac{\varepsilon_x^2}{\sigma_x^3(s)}. \tag{2.33}$$

In order to preserve the normalised emittance of a beam, the beam size has to be matched to the magnetic lattice structure[i]. A matched beam has little to no variation in its spot size, so by requiring $\sigma_x'' = 0$, we obtain

$$\sigma_x^{\text{mat}} = \left(\frac{\varepsilon_x^2}{k}\right)^{1/4}, \tag{2.34}$$

or alternatively,

$$\beta_x^{\text{mat}} = \frac{1}{\sqrt{k}} = \sqrt{\frac{\gamma m v}{qg}}. \tag{2.35}$$

So far, we have only considered magnetic lattice structures that are linear in x and y. When contributions from non-linear fields are included, particles in a mismatched beam with a nonzero energy spread will not rotate in phase space at the same rate, resulting in dilution in phase space, and thus also emittance growth.

2.1.6 Wakefields

A driving charge with a m-th multipole moment propagating in a vacuum chamber with a periodic structure that is not perfectly smooth or perfectly conducting can excite a wake electromagnetic field behind it [59] that will affect trailing charges. The electric fields in this case are not perpendicular to the chamber walls, and the magnetic fields are not parallel to the chamber walls, so that the wavefront moving with the leading charge can be scattered against the chamber walls and affect trailing charges.

The longitudinal component of the short-range wakefield in metallic cavities is usually dominated by the $m = 0$ mode, and can provide acceleration for trailing particles placed at appropriate distances behind the driving particle. Transverse (short-range) wakefields are usually dominated by the $m = 1$ dipole fields that behave similarly to the bending

[i] In a linear magnetic lattice there is emittance preservation also for a mismatched beam, if there is no energy spread.

effects seen in dipole magnets, and can deflect trailing particles and cause instabilities, as explained in chapter 3. For a beam with longitudinal beam head position ξ_{H}, longitudinal position distribution $\lambda(\xi)$ and particle charge q, the wakefields acting on a beam slice with mean transverse offset X located at longitudinal position ξ after an elapsed propagation distance s can be written in the form[ii] [59, 60]

$$\mathcal{W}_z(\xi) = q \int_{\xi_{\mathrm{H}}}^{\xi} W_z(\xi' - \xi)\lambda(\xi')\,\mathrm{d}\xi' \tag{2.36}$$

$$\boldsymbol{\mathcal{W}}_\perp(\xi, s) = q \int_{\xi_{\mathrm{H}}}^{\xi} \boldsymbol{W}_\perp(\xi' - \xi)\lambda(\xi')X(\xi', s)\,\mathrm{d}\xi'. \tag{2.37}$$

where $W_z(\xi' - \xi)$ and $\boldsymbol{W}_\perp(\xi' - \xi)$ are the longitudinal and transverse wake functions, respectively. The wake functions describe the shock response of the vacuum chamber environment to a δ-function beam which carries an m-th moment, and resemble Green's functions.

Transverse wakefields can lead to transverse instabilities known to limit the amount of charge that can be transported in an accelerator and hence constrain the efficiency. The wakefield formalism has been used in the parameter study of CLIC to study such a limitation [27]. Since for small perturbations, the hose instability (see chapter 3) in plasma is similar to the transverse instabilities found in conventional acceleration cavities[iii], we will subsequently make the ansatz that similar formalisms can be applied for plasma acceleration in the non-linear regime. The model based on the wakefield formalism is benchmarked against particle-in-cell simulations in chapter 3.

The beam slices and coordinates are illustrated in figure 2.4.

2.2 Linear plasma wakefield theory

In beam-driven plasma wakefield acceleration (PWFA), an ultra-relativistic drive beam is used to "plough through" a plasma to excite a plasma wake by transferring its energy to the plasma. As the drive beam propagates through the plasma, the space charge field from the beam will expel some of the plasma electrons from the propagation axis and create a trailing region with a lower plasma electron density. In most cases, the heavy plasma ions will remain stationary during relevant time scales, and will thus exert an attracting force on the expelled plasma electrons. Thus, after the electron beam has passed, the plasma electrons will be attracted back onto the propagation axis and set up a density oscillation known as the plasma wake. This process is illustrated in figure 2.5.

[ii] Note that different definitions are commonly used in literature. $\mathcal{W}$ is sometimes referred to as kick, while W is also referred to as the wake.

[iii] With the main difference being the accelerating structure can be transversely displaced by the beam fields, whereas the accelerating structure in conventional acceleration cavities are rigid.

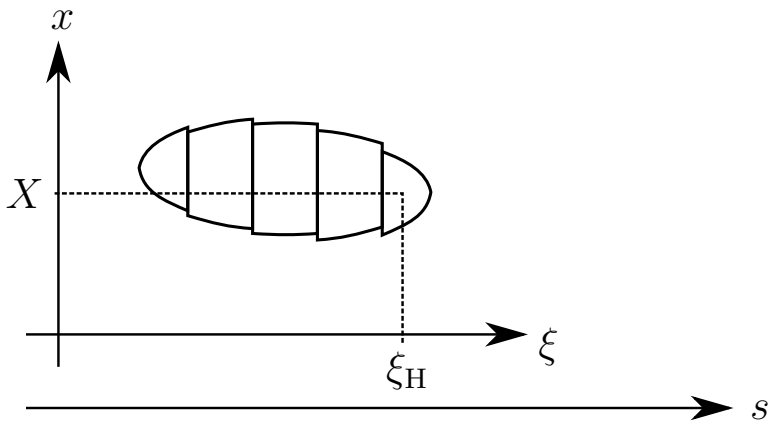

Figure 2.4: Illustration of beam slices and coordinates.

Large electric fields can be created by such plasma wakes, and a trailing witness beam appropriately placed can thus be accelerated by extracting energy from the wake.

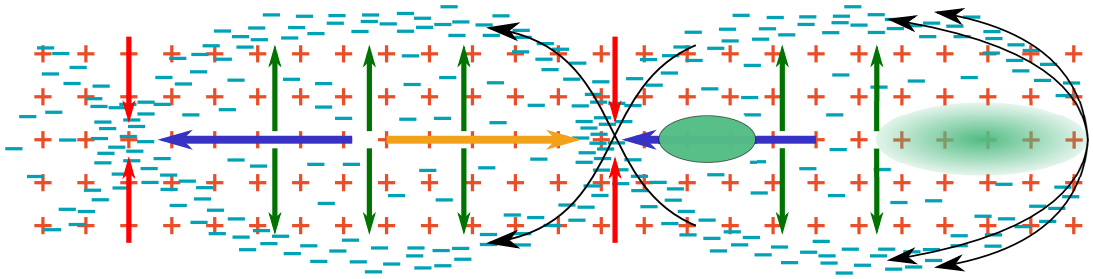

Figure 2.5: An illustration of the linear plasma acceleration process. A low-density ultra-relativistic electron beam expels part of the plasma electrons from the beam axis to form plasma ion cavities that can be used to accelerate a trailing electron beam. The yellow arrow illustrates the decelerating fields for electrons in one of the decelerating regions for electrons, the blue arrows indicate the accelerating fields for electrons and the green and red arrows highlight the focusing and defocusing fields for electrons, respectively.

2.2.1 Quasi-static approximation

The lab frame and the co-moving frame are related by the coordinate transformation $(x, y, z, t) \to (x, y, \xi, s)$ with

$$s = ct \tag{2.38}$$

$$\xi = z - ct \tag{2.39}$$

$$\frac{\partial}{\partial t} = \frac{\partial \xi}{\partial t}\frac{\partial}{\partial \xi} + \frac{\partial s}{\partial t}\frac{\partial}{\partial s} = -c\frac{\partial}{\partial \xi} + c\frac{\partial}{\partial s} \tag{2.40}$$

$$\frac{\partial}{\partial z} = \frac{\partial \xi}{\partial z}\frac{\partial}{\partial \xi} + \frac{\partial s}{\partial z}\frac{\partial}{\partial s} = \frac{\partial}{\partial \xi}. \tag{2.41}$$

An ultra-relativistic beam evolves over a much larger time scale compared to the plasma, which is evident when one compares the plasma wavelength with the betatron wavelength

$$\lambda_\beta = 2\pi\beta = \sqrt{2\gamma}\lambda_\mathrm{p}, \tag{2.42}$$

which is $\sqrt{2\gamma}$ times larger than the plasma wavelength[iv]. The quasi-static approximation,

$$\frac{\partial}{\partial t} \approx c\frac{\partial}{\partial s} \quad \text{for an ultra-relativistic beam,} \tag{2.43}$$

$$\frac{\partial}{\partial t} \approx -c\frac{\partial}{\partial \xi} \quad \text{for a plasma,} \tag{2.44}$$

exploits the fact that a short ultra-relativistic beam and its wake does not evolve significantly during the time it takes to pass by a plasma particle. This allows the beam and plasma evolution to be treated with separate scales.

2.2.2 Density perturbation

In the linear regime, the drive beam is only able to excite small density perturbations. Specifically, we make the following assumptions:

1. The plasma is initially neutral and uniform, with both the electron and ion number density equal to n_0.

2. The ions are much heavier than the plasma electrons, and remain stationary on relevant time scales.

3. The source is an ultra-relativistic particle beam with $v \approx c$ and number density $n_\mathrm{b} \ll n_0$. This means that the evolution of the beam distribution in response to forces generated in the plasma is negligible, and the system can be described perturbatively.

The evolution of the plasma electron number density n is governed by the continuity equation

$$\frac{\partial n}{\partial t} + \nabla \cdot (n\boldsymbol{v}) = 0, \tag{2.45}$$

where $\boldsymbol{v}$ is the velocity field.

The forces acting on the electrons are given by

$$m_\mathrm{e}\frac{\partial \boldsymbol{v}}{\partial t} = -e\left(\boldsymbol{E} + \boldsymbol{v} \times \boldsymbol{B}\right), \tag{2.46}$$

[iv]The derivation of this relation is given later as part of the derivation of equation (3.8).

and the evolution of the fields is governed by Maxwell's equations

$$\nabla \cdot \boldsymbol{E} = \frac{\rho}{\varepsilon_0} \tag{2.47}$$

$$\nabla \cdot \boldsymbol{B} = 0 \tag{2.48}$$

$$\nabla \times \boldsymbol{E} = -\frac{\partial \boldsymbol{B}}{\partial t} \tag{2.49}$$

$$\nabla \times \boldsymbol{B} = \mu_0 \boldsymbol{J} + \mu_0 \varepsilon_0 \frac{\partial \boldsymbol{E}}{\partial t}. \tag{2.50}$$

Equations (2.45)-(2.50) fully describe the evolution of the plasma and the fields, but the combination of these equations will result in non-linear partial differential equations that cannot be solved analytically for arbitrary sources. We therefore invoke our assumptions and express the density as a sum of the initial density and a perturbation δn as

$$n(\boldsymbol{r}, t) = n_0 + \delta n(\boldsymbol{r}, t). \tag{2.51}$$

In addition, the plasma velocity $\boldsymbol{v}$ and the fields $\boldsymbol{E}$ and $\boldsymbol{B}$ are also treated as perturbations. Inserting equation (2.51) into (2.45) and (2.46) and keeping only terms that are first order in the perturbative quantities yields

$$\frac{\partial \delta n}{\partial t} = -n_0 \nabla \cdot \boldsymbol{v} \tag{2.52}$$

$$\frac{\partial \boldsymbol{v}}{\partial t} = -\frac{e}{m_\mathrm{e}} \boldsymbol{E}. \tag{2.53}$$

By taking a time derivative of equation (2.52) and divergence of (2.53), these equations can be combined into

$$\frac{\partial^2 \delta n}{\partial t^2} + \omega_\mathrm{p}^2 \delta n = -\omega_\mathrm{p}^2 n_\mathrm{b}, \tag{2.54}$$

where the plasma frequency is given by

$$\omega_\mathrm{p} = \sqrt{\frac{e^2 n_0}{\varepsilon_0 m_\mathrm{e}}}, \tag{2.55}$$

and the divergence of $\boldsymbol{E}$ has been eliminated using Gauss' law

$$\nabla \cdot \boldsymbol{E} = \frac{e}{\varepsilon_0}(\delta n + n_\mathrm{b}). \tag{2.56}$$

It is however more convenient to use the co-moving coordinate $\xi = z - ct$ instead of time, and equation (2.54) written in terms of ξ reads

$$\frac{\partial^2 \delta n}{\partial \xi^2} + k_\mathrm{p}^2 \delta n = -k_\mathrm{p}^2 n_\mathrm{b}, \tag{2.57}$$

where the plasma wave number is given by

$$k_\mathrm{p} = \sqrt{\frac{e^2 n_0}{\varepsilon_0 m_\mathrm{e} c^2}}. \tag{2.58}$$

Equation (2.57) describes a driven harmonic oscillation without a damping term, which means the plasma is non-dissipative. This is expected since we assumed that the plasma has zero temperature before interacting with the beam and is a collision-less perfect conductor.

Green's functions can be used to solve equation (2.57). The Green's function for the operator $\partial_\xi^2 + k_\mathrm{p}^2$ is

$$G(\xi' - \xi) = \frac{1}{k_\mathrm{p}} \sin(k_\mathrm{p}(\xi' - \xi))\Theta(\xi' - \xi), \tag{2.59}$$

where $\Theta(\xi)$ is the Heaviside step function. For a cylinder symmetric drive beam, the solution can then be written as

$$\boxed{\delta n(r, \xi) = -k_\mathrm{p} \int_\xi^\infty n_\mathrm{b}(r, \xi') \sin(k_\mathrm{p}(\xi' - \xi))\, \mathrm{d}\xi'.} \tag{2.60}$$

A comparison of the plasma density oscillation in the linear regime with QuickPIC simulation results is shown in figure 2.6.

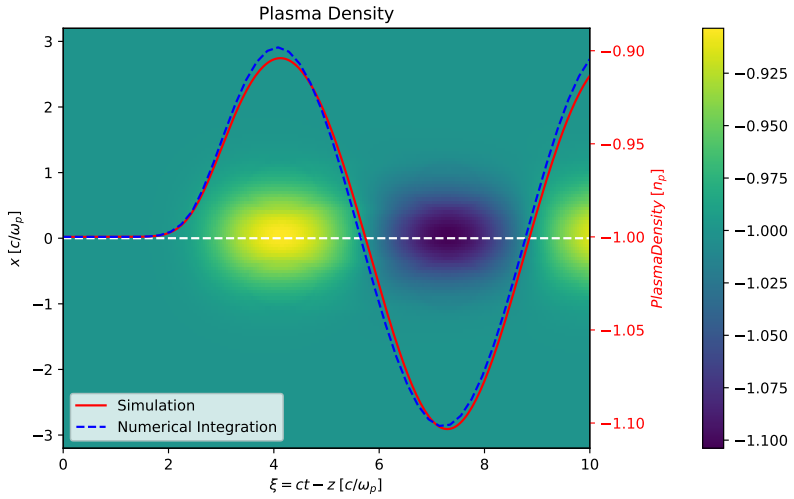

Figure 2.6: Linear plasma density oscillation calculated with QuickPIC simulation compared with the linear model.

2.2.3 Wakefields

We will now derive expressions for the electric fields due to the interaction between beam and plasma by using a similar approach as [61]. Taking the curl of Faraday's law, the time derivative of Ampère-Maxwell's law and using the vector identity

$$\nabla \times \nabla \times \boldsymbol{F} = \nabla(\nabla \cdot \boldsymbol{F}) - \nabla^2 \boldsymbol{F}, \tag{2.61}$$

we obtain

$$\nabla(\nabla \cdot \boldsymbol{E}) - \nabla^2 \boldsymbol{E} = -\mu_0 \left(\frac{\partial \boldsymbol{J}}{\partial t} + \varepsilon_0 \frac{\partial^2 \boldsymbol{E}}{\partial t^2} \right). \tag{2.62}$$

Applying Gauss' law to the first term and rearranging yields

$$\left(\nabla^2 - \frac{1}{c^2} \frac{\partial^2}{\partial t^2} \right) \boldsymbol{E} = \mu_0 \frac{\partial \boldsymbol{J}}{\partial t} + \frac{1}{\varepsilon_0} \nabla \rho. \tag{2.63}$$

The sources can be divided into components associated with the drive beam and plasma such that $\rho = -e(n_\mathrm{b} + n_0 + \delta n)$ and $\boldsymbol{J} = \boldsymbol{J}_\mathrm{b} + \boldsymbol{J}_\mathrm{p} = -e n_\mathrm{b} c \hat{\boldsymbol{z}} - e n_0 \boldsymbol{v}$. Furthermore, equation (2.53) can be used to obtain

$$\frac{\partial \boldsymbol{J}_\mathrm{p}}{\partial t} = -e n_0 \frac{\partial \boldsymbol{v}}{\partial t} = \varepsilon_0 \omega_\mathrm{p}^2 \boldsymbol{E}, \tag{2.64}$$

and finally also

$$\left(\nabla^2 - \frac{1}{c^2} \frac{\partial^2}{\partial t^2} - \frac{\omega_\mathrm{p}^2}{c^2} \right) \boldsymbol{E} = -\frac{e}{c\varepsilon_0} \frac{\partial n_\mathrm{b}}{\partial t} \hat{\boldsymbol{z}} - \frac{e}{\varepsilon_0} \nabla (n_\mathrm{b} + \delta n). \tag{2.65}$$

Transforming to the co-moving coordinate system, we obtain

$$(\nabla_\perp^2 - k_\mathrm{p}^2) \boldsymbol{E} = -\frac{e}{\varepsilon_0} (\nabla_\perp n_\mathrm{b} + \nabla \delta n), \tag{2.66}$$

where $\nabla_\perp$ is the transverse gradient operator. The longitudinal wakefield $\mathcal{W}_z$ that is used for particle acceleration, is given by the longitudinal component of equation (2.66) in linear wakefield theory since the Lorentz force has no longitudinal component in first order. Assuming cylindrical symmetry, the solution for the longitudinal component is [61]

$$\boxed{\mathcal{W}_z(r, \xi) = E_z(r, \xi) = \frac{e}{\varepsilon_0} \int_0^\infty \frac{\partial \delta n(r', \xi)}{\partial \xi} G_0(r, r') r' \mathrm{d}r',} \tag{2.67}$$

where

$$G_n(r, r') = I_n(k_\mathrm{p} r') K_n(k_\mathrm{p} r) \Theta(r - r') + I_n(k_\mathrm{p} r) K_n(k_\mathrm{p} r') \Theta(r' - r), \tag{2.68}$$

with I_n and K_n denoting n-th order modified Bessel functions of the first and second kind, respectively.

By taking the curl of equation (2.65) and using Faraday's law, we obtain

$$\left(\nabla^2 - \frac{1}{c^2} \frac{\partial^2}{\partial t^2} - \frac{\omega_\mathrm{p}^2}{c^2} \right) \boldsymbol{B} = \frac{e}{c\varepsilon_0} \nabla \times n_\mathrm{b} \hat{\boldsymbol{z}}, \tag{2.69}$$

which in co-moving cylindrical coordinate reads

$$(\nabla_\perp^2 - k_\mathrm{p}^2)\boldsymbol{B} = \frac{e}{c\varepsilon_0}\nabla \times n_\mathrm{b}\hat{\boldsymbol{z}}. \tag{2.70}$$

We now define the transverse wakefield as

$$\boldsymbol{\mathcal{W}}_\perp = \boldsymbol{E}_\perp + (\boldsymbol{v} \times \boldsymbol{B})_\perp. \tag{2.71}$$

Combining equation (2.66) and (2.70) gives

$$(\nabla_\perp^2 - k_\mathrm{p}^2)\boldsymbol{\mathcal{W}}_\perp = -\frac{e}{\varepsilon_0}\nabla_\perp \delta n, \tag{2.72}$$

which in the case of cylinder symmetry has the solution

$$\boxed{\mathcal{W}_r(r,\xi) = -\frac{e}{\varepsilon_0}\int_0^\infty \frac{\partial \delta n(r',\xi)}{\partial r'} G_1(r,r')r'\mathrm{d}r'.} \tag{2.73}$$

for the radial component $\mathcal{W}_r = E_r - cB_\varphi$ [61].

From equation (2.73) one can see the fundamental limitation of the linear regime. Since the transverse forces are proportional to the transverse wakefield, and $\mathcal{W}_r$ contains non-linear defocusing terms, the main beam beam size σ_r would have to be very small ($k_\mathrm{p}\sigma_r \ll 1$) in order to be affected only by the linear focusing part of the wakefield.

2.3 Non-linear plasma wakefield theory

Due to the fundamental limitation of the linear regime, non-linear plasma wakefield acceleration, also referred to as the blowout regime, is considered to be a much more reliable option. In the blowout regime, the drive beam has a density $n_\mathrm{DB} \gg n_0$, and creates non-linear plasma density perturbations. The plasma electrons are completely expelled from a region around the propagation axis, forming a thin sheath around an unshielded positive ion column. The much heavier plasma ions will still remain stationary during relevant time scales, and attract the plasma electrons back towards the axis, where they will overshoot and thus create a plasma density oscillation with plasma cavities completely devoid of plasma electrons. The blowout regime is illustrated in figure 2.7.

This section considers the theory for the blowout regime and examines its properties for electron acceleration. We will start the analysis using the Hamiltonian for a plasma electron to obtain a constant of motion, and then largely follow the derivations of [62] in SI units. The constant of motion is then combined with Maxwell's equations in the Lorenz gauge to derive an equation of motion for plasma electrons forming the electron sheath around the ion column. Lastly, expressions for the wakefields are presented, which will be used to model transverse beam dynamics in chapter 3.

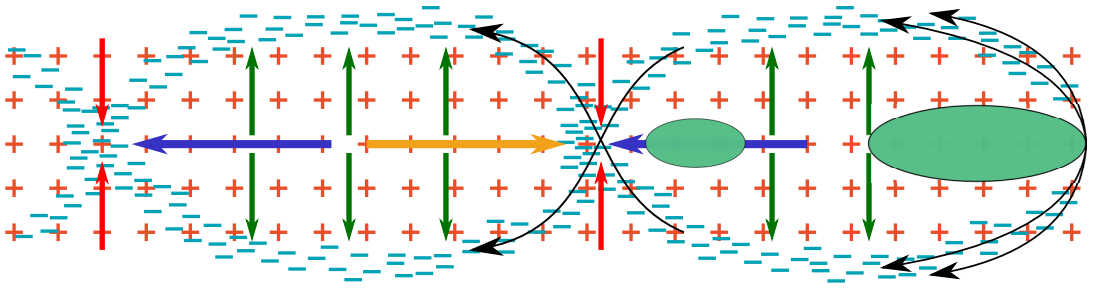

Figure 2.7: An illustration of the non-linear plasma acceleration scheme. A high-density ultra-relativistic electron beam expels all the plasma electrons from a region close to the beam axis to form plasma ion cavities that can be used to accelerate a trailing electron beam. Only positive plasma ions are left in the plasma ion cavities. The yellow arrow illustrates the decelerating fields for electrons in one of the decelerating regions for electrons, the blue arrows indicate the accelerating fields for electrons and the green and red arrows highlight the focusing and defocusing fields for electrons, respectively.

2.3.1 Hamiltonian mechanics and constant of motion

In canonical coordinates, the Poisson bracket for two functions $f(q, P, t)$ and $g(q, P, t)$ is defined as

$$\{f, g\} = \sum_i \left(\frac{\partial f}{\partial q_i} \frac{\partial g}{\partial P_i} - \frac{\partial f}{\partial P_i} \frac{\partial g}{\partial q_i} \right). \tag{2.74}$$

Let $f(q, P, t)$ be a function of the canonical coordinates q, P and time t. The total time derivative is then given by

$$\frac{\mathrm{d}f}{\mathrm{d}t} = \sum_i \left(\frac{\partial f}{\partial q_i} \dot{q}_i + \frac{\partial f}{\partial P_i} \dot{P}_i \right) + \frac{\partial f}{\partial t} \tag{2.75}$$

$$= \sum_i \left(\frac{\partial f}{\partial q_i} \frac{\partial H}{\partial P_i} + \frac{\partial f}{\partial P_i} \frac{\partial H}{\partial q_i} \right) + \frac{\partial f}{\partial t} \tag{2.76}$$

$$= \{f, H\} + \frac{\partial f}{\partial t}, \tag{2.77}$$

where we in the second line used Hamilton's equations

$$\dot{q}_i = \frac{\partial H}{\partial P_i}, \quad \dot{P}_i = -\frac{\partial H}{\partial q_i}. \tag{2.78}$$

We assume that the Hamiltonian depends on z and t through the co-moving coordinate ξ. It follows that

$$\frac{\partial H}{\partial t} = -c \frac{\partial H}{\partial \xi} = c \dot{P}_z, \tag{2.79}$$

and from equation (2.77) we have $\mathrm{d}H/\mathrm{d}t = \partial H/\partial t$, which leads to the constant of motion

$$\frac{\mathrm{d}}{\mathrm{d}t}(H - cP_z) = 0. \tag{2.80}$$

The Hamiltonian for a plasma electron is

$$H = \gamma m_\mathrm{e} c^2 - e\phi, \tag{2.81}$$

where ϕ is the scalar electric potential, and the canonical momentum is given by

$$\boldsymbol{P} = \boldsymbol{p} - e\boldsymbol{A}, \tag{2.82}$$

where $\boldsymbol{p} = \boldsymbol{p}_\perp + p_z\hat{\boldsymbol{z}}$ is the electron's momentum and $\boldsymbol{A}$ is the vector potential.

Before interacting with the beam, the plasma electron is at rest. Thus, we set the constant of motion equal to the electron's rest energy and insert the expressions for the Hamiltonian and the canonical momentum. This yields

$$\gamma m_\mathrm{e} c^2 - e\psi - cp_z = m_\mathrm{e} c^2, \tag{2.83}$$

where we have introduced the pseudo-potential

$$\psi = \phi - cA_z. \tag{2.84}$$

The constant of motion can also be rearranged into

$$\boxed{1 - \frac{v_z}{c} = \frac{1}{\gamma}\left(1 + \frac{e\psi}{m_\mathrm{e} c^2}\right),} \tag{2.85}$$

which is more convenient for later derivations.

By combining the constant of motion and

$$\gamma = \sqrt{1 + \frac{p_\perp^2 + p_z^2}{(m_\mathrm{e} c)^2}}, \tag{2.86}$$

it can be shown that

$$\gamma = \frac{1}{2(1 + e\psi/(m_\mathrm{e} c^2))}\left[1 + \left(\frac{p_\perp}{m_\mathrm{e} c}\right)^2 + \left(1 + \frac{e\psi}{m_\mathrm{e} c^2}\right)^2\right] \tag{2.87}$$

$$p_z = \frac{m_\mathrm{e} c}{2(1 + e\psi/(m_\mathrm{e} c^2))}\left[1 + \left(\frac{p_\perp}{m_\mathrm{e} c}\right)^2 - \left(1 + \frac{e\psi}{m_\mathrm{e} c^2}\right)^2\right], \tag{2.88}$$

which shows that once the transverse momentum $p_\perp$ and the pseudo-potential ψ are solved, γ and p_z are also known.

2.3.2 Equation of motion for a plasma electron

The forces acting on a plasma electron is given by Lorentz's force equation

$$\frac{\mathrm{d}\boldsymbol{p}}{\mathrm{d}t} = -e(\boldsymbol{E} + \boldsymbol{v} \times \boldsymbol{B}). \tag{2.89}$$

Using the quasi-static approximation and the constant of motion, the total time derivative can be written as

$$\frac{\mathrm{d}}{\mathrm{d}t} \approx \frac{\partial}{\partial t} + \frac{\partial}{\partial \xi}\frac{\mathrm{d}\xi}{\mathrm{d}t} \approx (v_z - c)\frac{\partial}{\partial \xi} = -\frac{c}{\gamma}\left(1 + \frac{e\psi}{m_\mathrm{e}c^2}\right)\frac{\partial}{\partial \xi}. \tag{2.90}$$

It follows that

$$\frac{\partial \boldsymbol{p}_\perp}{\partial \xi} = \frac{e\gamma}{c(1 + e\psi/(m_\mathrm{e}c^2))}(\boldsymbol{E}_\perp + (\boldsymbol{v} \times \boldsymbol{B})_\perp). \tag{2.91}$$

In order to eliminate $\boldsymbol{E}_\perp$ and $\boldsymbol{B}_\perp$, we now use Maxwell's equation in the Lorenz gauge

$$\nabla \cdot \boldsymbol{A} + \frac{1}{c^2}\frac{\partial \phi}{\partial t} = 0, \tag{2.92}$$

which can be written as

$$\left(\nabla^2 - \frac{1}{c^2}\frac{\partial^2}{\partial t^2}\right)\phi = -\frac{\rho}{\varepsilon_0} \tag{2.93}$$

$$\left(\nabla^2 - \frac{1}{c^2}\frac{\partial^2}{\partial t^2}\right)\boldsymbol{A} = -\mu_0 \boldsymbol{J}. \tag{2.94}$$

Again by transforming to the co-moving frame, Maxwell's equations can be written as

$$\nabla_\perp^2 \phi = -\frac{\rho}{\varepsilon_0} \tag{2.95}$$

$$\nabla_\perp^2 \boldsymbol{A} = -\mu_0 \boldsymbol{J}, \tag{2.96}$$

and can also be combined into a Poisson's equation for ψ

$$\nabla_\perp^2 \psi = \frac{1}{\varepsilon_0}\left(\frac{1}{c}J_z - \rho\right). \tag{2.97}$$

Assuming cylinder symmetry, we can write

$$\boldsymbol{E}_\perp + (\boldsymbol{v} \times \boldsymbol{B})_\perp = (E_r - v_z B_\varphi)\hat{\boldsymbol{r}} = \left(-\frac{\partial \phi}{\partial r} + (c - v_z)\frac{\partial A_r}{\partial \xi} + v_z \frac{\partial A_z}{\partial r}\right)\hat{\boldsymbol{r}}. \tag{2.98}$$

In order to substitute for the terms in equation (2.98), we solve equation (2.95) and (2.96) for $\sigma_r \ll r \leq r_\mathrm{b}$, where σ_r is the transverse size of the beam and $r_\mathrm{b} = r_\mathrm{b}(\xi)$ is the plasma bubble radius at ξ. This yields

$$\frac{\partial \phi}{\partial r} = \frac{e}{\varepsilon_0}\left(\frac{\lambda}{r} - \frac{1}{2}n_0 r\right) \tag{2.99}$$

$$\frac{\partial A_z}{\partial r} = \frac{e\lambda}{\varepsilon_0 c r}, \tag{2.100}$$

where $\lambda(\xi) = \int_0^r n_\mathrm{b}(r', \xi) r' \mathrm{d}r'$, and n_b is the number density of the beam. In order to substitute for $\partial_\xi A_r$, we will first solve equation (2.97). By assuming cylinder symmetry and using cylinder coordinates, it can be written as

$$\frac{1}{r}\frac{\partial}{\partial r}\left(r\frac{\partial \psi}{\partial r}\right) = \frac{1}{\varepsilon_0}\left(\frac{1}{c}J_{z\mathrm{e}} + en_\mathrm{e} - en_0\right), \tag{2.101}$$

where $J_{z\mathrm{e}}$ is the plasma electron axial current density, n_e is the plasma electron density and contributions from the ultra-relativistic beam to $J_z/c - \rho$ have been cancelled out. For $\sigma_r \ll r \leq r_\mathrm{b}$, only the contribution from the unshielded ion column remains, so equation (2.101) can be directly integrated to obtain

$$\psi(r, \xi) = \psi_0(\xi) - \frac{en_0}{4\varepsilon_0} r^2, \tag{2.102}$$

with $\psi_0(\xi) = \psi(r = 0, \xi)$ to be determined later. Lastly, the gauge condition can also be written as

$$\nabla_\perp \cdot \boldsymbol{A}_\perp = \frac{1}{c}\frac{\partial \psi}{\partial \xi}, \tag{2.103}$$

which then leads to $A_r = r/(2c)\mathrm{d}_\xi \psi_0$ and

$$\frac{\partial A_r}{\partial \xi} = \frac{r}{2c}\frac{\mathrm{d}^2 \psi_0}{\mathrm{d}\xi^2}. \tag{2.104}$$

Substituting equation (2.99), (2.100) and (2.104) into (2.98) leads to

$$E_r - v_z B_\varphi = \frac{en_0}{2\varepsilon_0} r - \left(1 - \frac{v_z}{c}\right)\frac{e}{\varepsilon_0}\frac{\lambda}{r} + \left(1 - \frac{v_z}{c}\right)\frac{r}{2}\frac{\mathrm{d}^2 \psi_0}{\mathrm{d}\xi^2}, \tag{2.105}$$

and invoking equation (2.85) yields

$$E_r - v_z B_\varphi = \frac{en_0}{2\varepsilon_0} r - \left(1 + \frac{e\psi}{m_\mathrm{e}c^2}\right)\frac{e}{\gamma\varepsilon_0}\frac{\lambda}{r} + \left(1 + \frac{e\psi}{m_\mathrm{e}c^2}\right)\frac{r}{2\gamma}\frac{\mathrm{d}^2 \psi_0}{\mathrm{d}\xi^2}. \tag{2.106}$$

The radial momentum of a plasma electron can be written as

$$p_r = \gamma m_\mathrm{e} v_r = \gamma m_\mathrm{e}\frac{\mathrm{d}r}{\mathrm{d}t} = -m_\mathrm{e}c\left(1 + \frac{e\psi}{m_\mathrm{e}c^2}\right)\frac{\partial r}{\partial \xi}, \tag{2.107}$$

so that the equation of motion for a plasma electron following the innermost trajectory $r = r_\mathrm{b}(\xi)$, which defines the inner boundary of the bubble, is

$$m_\mathrm{e}c^2\frac{\partial}{\partial \xi}\left[\left(1 + \frac{e\psi}{m_\mathrm{e}c^2}\right)\frac{\mathrm{d}r_\mathrm{b}}{\mathrm{d}\xi}\right] = -\frac{e^2 n_0}{2\varepsilon_0}\frac{\gamma}{1 + e\psi/(m_\mathrm{e}c^2)} r_\mathrm{b} + \frac{e^2}{\varepsilon_0}\frac{\lambda}{r_\mathrm{b}} - \frac{e}{2}\frac{\mathrm{d}^2 \psi_0}{\mathrm{d}\xi^2} r_\mathrm{b}. \tag{2.108}$$

By eliminating γ, we can obtain an equation of motion fully specified by ψ. Inserting equation (2.107) into (2.87), we obtain an expression for γ dependant only on ψ and r_b:

$$\gamma = \frac{1}{2(1+e\psi/(m_\mathrm{e}c^2))}\left[1+\left(1+\frac{e\psi}{m_\mathrm{e}c^2}\right)^2\left(\frac{\mathrm{d}r_\mathrm{b}}{\mathrm{d}\xi}\right)^2+\left(1+\frac{e\psi}{m_\mathrm{e}c^2}\right)^2\right]. \tag{2.109}$$

This enables the trajectory of the innermost plasma electrons to be fully specified by $\psi(r_\mathrm{b}(\xi),\xi)$ through

$$\boxed{\begin{aligned} m_\mathrm{e}c^2\frac{\partial}{\partial\xi}\left[\left(1+\frac{e\psi}{m_\mathrm{e}c^2}\right)\frac{\mathrm{d}r_\mathrm{b}}{\mathrm{d}\xi}\right] = -\frac{e^2n_0}{4\varepsilon_0}r_\mathrm{b}\left[\frac{1}{(1+e\psi/(m_\mathrm{e}c^2))^2}+\left(\frac{\mathrm{d}r_\mathrm{b}}{\mathrm{d}\xi}\right)^2+1\right] \\ +\frac{e^2}{\varepsilon_0}\frac{\lambda}{r_\mathrm{b}}-\frac{e}{2}\frac{\mathrm{d}^2\psi_0}{\mathrm{d}\xi^2}r_\mathrm{b}. \end{aligned}} \tag{2.110}$$

ψ_0 remains to be specified in order to obtain a closed equation of motion. Reference [62] reported that the results are very insensitive to the $\rho - J_z/c$ profile, and chose a simplified profile such that

$$\rho-\frac{1}{c}J_z = \begin{cases} en_0 & 0<r\le r_\mathrm{b} \\ -en_0n_\Delta & r_\mathrm{b}<r<r_\mathrm{b}+\Delta \\ 0 & r_\mathrm{b}+\Delta<r \end{cases}, \tag{2.111}$$

where

$$n_\Delta(\xi) = \frac{r_\mathrm{b}^2(\xi)}{(r_\mathrm{b}(\xi)+\Delta)^2-r_\mathrm{b}^2(\xi)} \tag{2.112}$$

and $\Delta = \Delta_s + \Delta_L$ is the thickness of the plasma electron sheath, as outlined in figure 2.8.

Now we invert equation (2.101) and set $\psi(r,\xi)=0$ for $r\to\infty$ to obtain

$$\psi_0(\xi) = \frac{1}{\varepsilon_0}\int_0^\infty\frac{1}{r}\int_0^r\left(\rho-\frac{1}{c}J_z\right)r'\mathrm{d}r'\mathrm{d}r, \tag{2.113}$$

and by applying the simplified profile, we obtain

$$\psi_0(\xi) = \frac{en_0}{4\varepsilon_0}\kappa(\xi)r_\mathrm{b}^2(\xi), \tag{2.114}$$

where

$$\kappa = \frac{(1+\Delta/r_\mathrm{b})^2\ln(1+\Delta/r_\mathrm{b})^2}{(1+\Delta/r_\mathrm{b})^2-1}. \tag{2.115}$$

In the ultra-relativistic limit, $\Delta \ll r_\mathrm{b}$ so that $\kappa\to 1$ except at the back of the bubble. In this limit, equation (2.110) reduces to

$$\boxed{r_\mathrm{b}\frac{\mathrm{d}^2r_\mathrm{b}}{\mathrm{d}\xi^2}+2\left(\frac{\mathrm{d}r_\mathrm{b}}{\mathrm{d}\xi}\right)^2+1=\frac{4\lambda}{n_0r_\mathrm{b}^2},} \tag{2.116}$$

which is often referred to as Lu's equation.

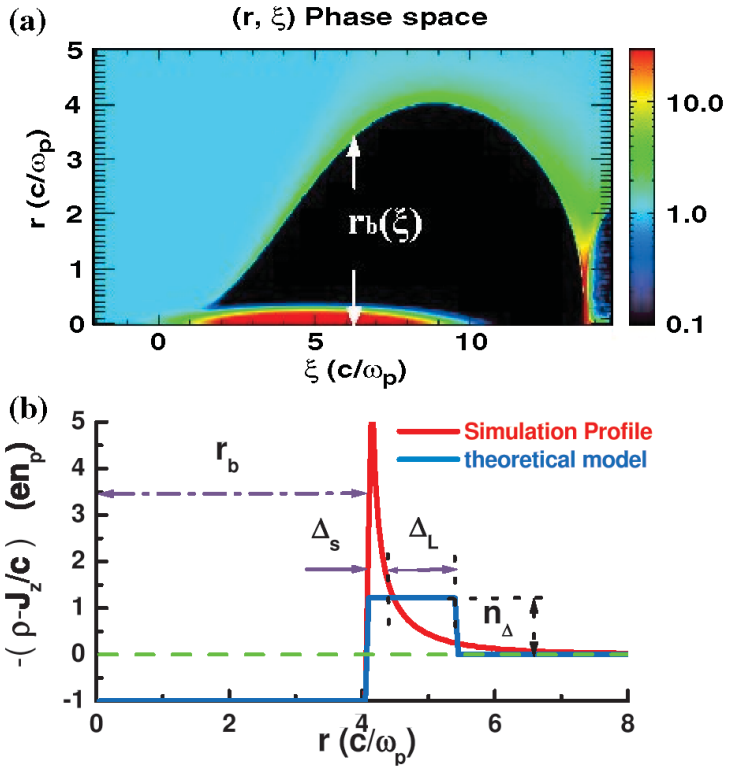

Figure 2.8: (a) Electron density with bubble radius $r_\mathrm{b}(\xi)$. (b) $\rho - J_z/c$ profile. The figures are adapted from reference [62].

2.3.3 Wakefields

The electric field is given by

$$\boldsymbol{E} = -\nabla\phi - \frac{\partial \boldsymbol{A}}{\partial t}. \tag{2.117}$$

Assuming $\partial_s E_z \ll \partial_\xi E_z$, i.e. that the longitudinal component does not evolve significantly over the propagation distance s, the longitudinal component can be written as

$$E_z = -\frac{\partial\phi}{\partial\xi} + c\frac{\partial A_z}{\partial\xi} = -\frac{\partial\psi}{\partial\xi}. \tag{2.118}$$

In the ultra-relativistic limit,

$$\psi(r,\xi) = \frac{en_0}{4\varepsilon_0}(r_\mathrm{b}^2(\xi) - r^2). \tag{2.119}$$

We then obtain an expression for the longitudinal wakefield from an ultra-relativistic drive beam in the non-linear regime by substituting equation (2.119) into (2.118):

$$\mathcal{W}_z = E_z = -\frac{en_0}{2\varepsilon_0} r_\mathrm{b}\frac{\mathrm{d}r_\mathrm{b}}{\mathrm{d}\xi}. \tag{2.120}$$

Assuming cylinder symmetry, the transverse wakefield from an ultra-relativistic drive beam is given by

$$\mathcal{W}_{r\mathrm{D}} = E_r - cB_\varphi \tag{2.121}$$
$$= -\frac{\partial \phi}{\partial r} + c\frac{\partial A_z}{\partial r} \tag{2.122}$$
$$= -\frac{\partial \psi}{\partial r} \tag{2.123}$$
$$= \frac{en_0}{2\varepsilon_0} r, \tag{2.124}$$

which acts as a linear focusing force for electrons. This shows that the non-linear regime is ideal for electron acceleration, as $\mathcal{W}_z$ is independent of r, $\mathcal{W}_{r\mathrm{D}}$ provides linear focusing for electrons and is independent of ξ.

However, we have so far only considered beams that are aligned and centered at the plasma bubble axis. In the case of a transversely misaligned main beam, the total transverse wakefield consists of the drive beam transverse wakefield and the main beam intra-beam wakefield $\mathcal{W}_r$, which is excited by the beam head and similar to a dipole wake field in RF cavities.

We now assume that the transverse forces can be expressed using the wake function formalism [63, 59], which is used for describing the well-known beam breakup instability [59] in RF accelerators, and will allow for easier comparison with RF accelerators. In CLIC, single beam transverse wakefield for small distances between a driving particle located at ξ' and a witness particle located at ξ is modelled using [32, 60]

$$W_r(\xi' - \xi) = \frac{2}{\pi\varepsilon_0}\frac{\xi' - \xi}{a^4}\Theta(\xi' - \xi), \tag{2.125}$$

where a is the accelerating structure iris radius. The structure iris is however not well-defined for a plasma, but an effective structure iris [64, 65] can be defined by $a = r_\mathrm{b}(\xi') + \alpha k_\mathrm{p}^{-1}$. Here $r_\mathrm{b}(\xi')$ is the plasma bubble radius at the location of the driving particle, α a numerical coefficient on the order of one, and the plasma skin depth k_p^{-1} accounts for the penetration depth of the electromagnetic fields. Equation (2.125) along with the modification $a = r_\mathrm{b}(\xi') + \alpha k_\mathrm{p}^{-1}$ has been proposed for the PWFA blowout regime in reference [65].

$$\boxed{W_r(\xi' - \xi, \alpha) = \frac{2}{\pi\varepsilon_0}\frac{\xi' - \xi}{(r_\mathrm{b}(\xi') + \alpha k_\mathrm{p}^{-1})^4}\Theta(\xi' - \xi),} \tag{2.126}$$

We adopt this wake function, and use the value $\alpha = 0.75$, which is the same value used in reference [65]. A transverse wake function of the form given by equation (2.125) can in fact be derived from non-linear plasma wakefield theory. This is shown in appendix A.

The transverse wake intra-beam wakefield acting on a beam slice located at ξ after an elapsed propagation distance s is given by the convolution integral

$$\mathcal{W}_r(\xi, s) = -e \int_{\xi_\mathrm{H}}^{\xi} W_r(\xi' - \xi)\lambda(\xi')X(\xi', s)\,\mathrm{d}\xi' \tag{2.127}$$

where e is the elementary charge, ξ_H is the longitudinal position of the beam head, $\lambda(\xi)$ is the longitudinal number density of the main beam and $X(\xi, s)$ is the mean transverse offset of the beam slice located at ξ after an elapsed propagation distance s.

CHAPTER 3

Transverse Instabilities and Mitigation

For a transversely offset beam, the intra-beam transverse (dipole) wakefield excited by the head of the beam will act as a defocusing force and deflect the trailing part of the beam. This can build up resonantly along the beam and lead to beam breakup (BBU) instability in high-intensity RF linacs. This phenomenon was observed for the first time by Kelliher and Beadle in 1960 [66], and later by Panofsky and Bander, who also presented their theory on BBU instability [67].

A similar phenomenon called hose instability is considered one of the most important instabilities for intense beam-plasma interactions, and was first described by Whittum et al. [68]. Like BBU instability, the electron hose instability is usually seeded by a transverse beam offset. A transversely offset electron beam slice will perturb the plasma electron blow-out trajectory and displace the ion channel, which responds like a harmonic oscillator and deflects the subsequent portion of beam. If left unmitigated, the coupling between beam and plasma will result in amplification of beam slice centroid transverse displacement during propagation in plasma.

The effect of hose instability and mitigation mechanisms must be taken into account in the parameter study of a PWFA linear collider. The main difference between BBU instability in RF cavities and hose instability in plasma is RF cavities being rigid structures, while ion channels in plasma can be displaced. Thus, for small perturbations, the hose instability is similar to BBU instabilities. In this chapter, we utilise the wakefield formalism used in conventional accelerator studies to study the transverse instabilities in the main beam with a simplified quasi-static model. The simplified quasi-static model is then combined with QuickPIC to perform a parameter study of a TeV-scale PWFA

linear accelerator in the non-linear regime, where the restriction on efficiency imposed by transverse instabilities is taken into account. Part of the findings are also outlined in reference [69].

3.1 Simplified quasi-static model

The total time derivative can be written as

$$\frac{\mathrm{d}}{\mathrm{d}t} = \frac{\partial}{\partial t} + \frac{\mathrm{d}z}{\mathrm{d}t}\frac{\partial}{\partial z} \tag{3.1}$$

$$= -c\frac{\partial}{\partial \xi} + c\frac{\partial}{\partial s} + \frac{\mathrm{d}\xi}{\mathrm{d}t}\frac{\partial}{\partial \xi} \tag{3.2}$$

$$= c\frac{\partial}{\partial s}. \tag{3.3}$$

Newton's second law of motion for a beam electron with transverse position $X = X(\xi, s)$ in the x-direction can thus be written as

$$F_x = \frac{\mathrm{d}p_x}{\mathrm{d}t} = c\frac{\partial}{\partial s}\left(\gamma m_\mathrm{e}\frac{\mathrm{d}X}{\mathrm{d}t}\right). \tag{3.4}$$

For an ultra-relativistic beam electron focused by the background ion force and deflected by the transverse intra-beam wakefield, the equation reads

$$\frac{\partial}{\partial s}\left(\gamma\frac{\partial X}{\partial s}\right) = \frac{F_x}{m_\mathrm{e}c^2} \tag{3.5}$$

$$= -\frac{e}{m_\mathrm{e}c^2}\mathcal{W}_r - \frac{e^2 n_0}{2\varepsilon_0 m_\mathrm{e}c^2}X \tag{3.6}$$

$$= -\frac{e}{m_\mathrm{e}c^2}\mathcal{W}_r - \frac{1}{2}k_\mathrm{p}^2 X. \tag{3.7}$$

$$\boxed{\frac{\partial^2}{\partial s^2}X + \frac{1}{\gamma}\frac{\partial \gamma}{\partial s}\frac{\partial}{\partial s}X + k_\beta^2 X = -\frac{e}{\mathscr{E}}\mathcal{W}_r,} \tag{3.8}$$

where $\gamma = \gamma(\xi, s)$ is the Lorentz factor, $k_\beta = k_\beta(\xi, s) = 1/\beta(\xi, s) = k_\mathrm{p}/\sqrt{2\gamma(\xi, s)}$ is the betatron wave number, and $\mathscr{E} = \mathscr{E}(\xi, s) = \gamma(\xi, s)m_\mathrm{e}c^2$ is the electron energy of an electron located at ξ that has been accelerated by the longitudinal field $E_z(\xi)$ over a distance s.

Furthermore, since the forces depend on the charge to mass ratio, equation (3.8) is also valid for a beam slice macroparticle with mean transverse offset $X(\xi, s)$. The beam slices can be considered as rigid point charges with charge $-N(\xi)e$, where $N(\xi)$ is the number of particles in a beam slice located at ξ.

The driving term of equation (3.8) is attributed to the transverse wakefields. All beam slices preceding a reference slice located at ξ contribute to the driving force acting on

the reference slice through the wakefield $\mathcal{W}_r$. The interaction with the plasma and drive beam is represented by the wake function and the interaction with the total longitudinal wakefield $E_z(\xi)$. While $r_\mathrm{b}(\xi)$ and $E_z(\xi)$ can be estimated using non-linear wakfield theory, both $r_\mathrm{b}(\xi)$ and $E_z(\xi)$ were calculated numerically with QuickPIC [70]. Assuming that $r_\mathrm{b}(\xi)$ and $E_z(\xi)$ do not change significantly during propagation, these quantities only need to be calculated once in QuickPIC, and can then be used with equation (2.126), (2.127) and (3.8) to model transverse beam dynamics inside the plasma ion bubble. Note that this approach assumes that the transverse wakefields are not large enough to deflect the beam into the plasma ion bubble boundary during the propagation process.

Note that there are more complicated models for modelling transverse beam dynamics in PWFA that does not directly utilise the wakefield formalism. One of the earliest models was formulated by Whittum et al. to describe transverse instabilities through the coupled transverse displacement of beam centroid and plasma density perturbation centroid [68]. This was improved upon in reference [71], which accounted for relativistic sheath electrons, the ξ-dependence of the blowout radius and the beam current. Reference [72] made further improvements by accounting for the damping/amplification of the beam centroid oscillations due to relativistic mass gain/loss of beam electrons, in addition to including the damping effect of the centroid oscillations arising from energy chirp and sub-percent uncorrelated beam energy spread.

3.1.1 QuickPIC

While the theories outlined in chapter 2 are able to describe beam-plasma interactions in certain situations, numerical simulations are required in general to study plasma excitation and acceleration processes. In most cases of interest, the excitation process of wakefields is highly non-linear and results in non-laminar flows. Thus, a particle-based approach such as particle-in-cell (PIC) codes are required.

In a fully explicit PIC algorithm, all particles are represented by a large collection of macroparticles whose motions are calculated based on the electromagnetic fields calculated on a 3D grid of cells covering the simulation domain. The number of macroparticles must be large enough to suppress fluctuations of the electromagnetic fields on the grid points caused by the randomness of particle motion.

The calculation cycle in PIC-codes typically follows the steps

1. Weight the charge and current densities onto the grid points by using nearby macroparticles.

2. Solve Maxwell's equations to calculate the electromagnetic fields at the grid points.

3. Calculate the forces acting on the macroparticles by interpolating the electromagnetic fields to particle positions.

4. Update particle positions and velocities by integrating the equations of motion.

5. Repeat previous steps until end conditions are met.

For most plasma simulations, the grid cell size Δx has to be small compared to the Debye length in order to produce meaningful results. In PWFA, a cold plasma is assumed so that the simulation has to resolve the collisionless skin depth $k_\mathrm{p}^{-1} = c/\omega_\mathrm{p}$. In addition, the time step Δt between successive updates must be able to resolve characteristic timescales for plasma oscillations and satisfy the Courant condition $\Delta t < \Delta x/c$ (for 1D) to avoid numerical instabilities. For typical plasma densities $n_0 \sim 10^{16}\,\mathrm{cm}^{-3}$, $k_\mathrm{p}^{-1} \sim 10\,\mu\mathrm{m}$, while a typical simulation domain is on the order of mm^{-3}. This implies a minimum of $\sim 10^6$ grid cells, while it requires $\sim 10^{13}$ particle pushes to model a single GeV PWFA stage [70]. In addition, full PIC-codes can give rise to spurious Cherenkov radiation due to a non-ideal dispersion relation for electromagnetic waves in a full PIC-code. Thus, full PIC-codes are not feasible for simulating a full length TeV-scale plasma accelerator.

In order to reduce the computational cost, QuickPIC [70], which is a fully parallelised, fully relativistic, 3D PIC-code, utilises the quasi-static approximation to treat the evolution of the beam and plasma wake separately. Under the quasi-static approximation, the coordinate ξ corresponds to the fast timescale that a short ultra-relativistic beam needs to pass a plasma particle, and the timescale in which a plasma wake is developed in response to the beam. s then corresponds to the large timescale associated with the evolution of the beam. In QuickPIC, the plasma response and wakefields are only updated once the beam has been propagated and evolved, as illustrated in figure 3.1.

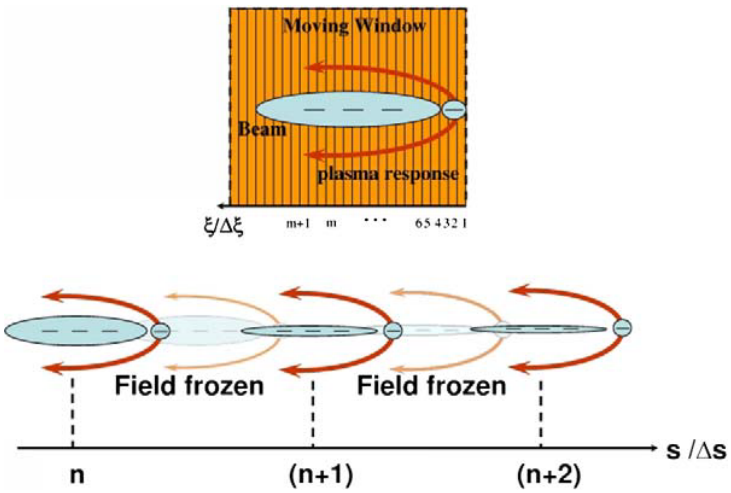

Figure 3.1: Schematics of the update routine of beam and plasma response in QuickPIC. The figure is adapted from reference [70].

Using this approximation, QuickPIC has achieved a speed-up of several orders of magnitudes, while maintaining a good agreement compared to full PIC-codes such as OSIRIS. A comparison of radial electric and azimuthal magnetic fields for an electron drive beam between QuickPIC and Osiris can be seen in figure 3.2. Furthermore, Cherenkov radiation does not develop in codes using the quasi-static approximation, as the quasi-static approximation does not describe radiation.

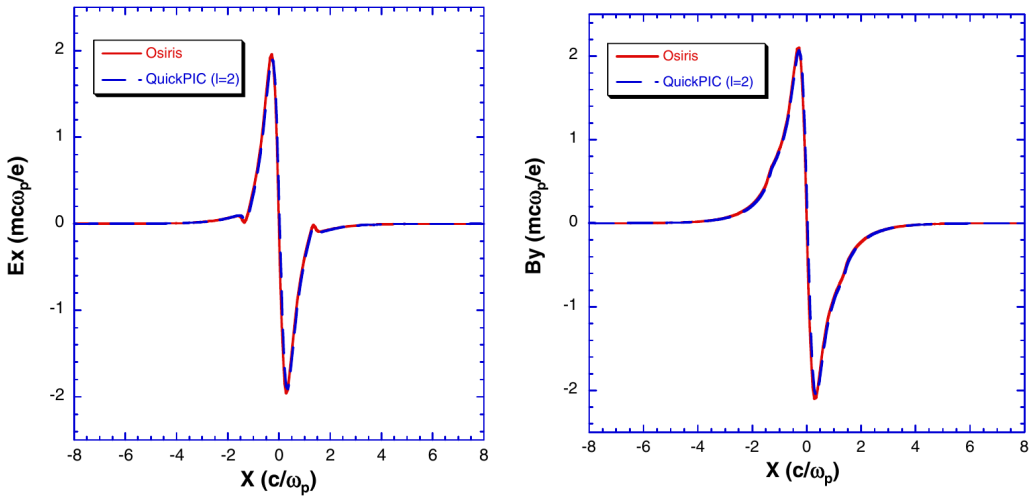

Figure 3.2: Comparison of radial electric and azimuthal magnetic fields for an electron drive beam between QuickPIC and Osiris. The figures are adapted from reference [70].

Due to $\sqrt{2\gamma} \gg 1$ in the studied cases, a quasi-static code such as QuickPIC is suitable for modelling beam-plasma interactions. However, at even higher energies, radiation phenomena such as betatron radiation may become more significant.

3.1.2 Benchmarking the wakefield model with QuickPIC

In order to satisfy the assumption of non-evolving $E_z(\xi)$ and $r_\mathrm{b}(\xi)$, we performed all benchmarking using a set of parameters based on the FACET-II parameters [73], where the energy of the beams was increased to 100 GeV to avoid any significant head erosion [74] of the drive beam, and hence also avoid significant changes in $E_z(\xi)$ and $r_\mathrm{b}(\xi)$. σ_r was also modified to match the beams to a plasma with density $n_0 = 4 \cdot 10^{16}\,\mathrm{cm}^{-3}$. Relevant benchmarking parameters are given in table 3.1.

Equation (2.127) gives the transverse wakefield along the main beam after a propagation length s, as is illustrated in figure 3.3a-3.3d, where the transverse wakefield calculated using equation (2.126) and (2.127) is compared against the corresponding fields extracted from QuickPIC simulations at several values of s. As already mentioned, inside the ion bubble, the transverse fields acting on the main beam consist of the background ion focusing and intra-beam wakefields, which are similar to dipole fields. To avoid noise and to eliminate the contribution from the background ion focusing, the dipole fields extracted from QuickPIC were measured on axis. The particle number in the beam slices is given by $N(\xi)$ extracted from QuickPIC, which is also plotted for reference.

	Drive beam	**Main beam**
$\mathscr{E}_0$ [GeV]	100	100
Q [nC]	-1.6	-0.5
σ_r [µm]	2.05	2.05
σ_z [µm]	12.77	6.38

Table 3.1: Modified FACET-II beam parameters used for benchmarking. $\mathscr{E}_0$ is the initial beam energy, Q is the beam charge, σ_r is the rms transverse beam size and σ_z is the rms beam length.

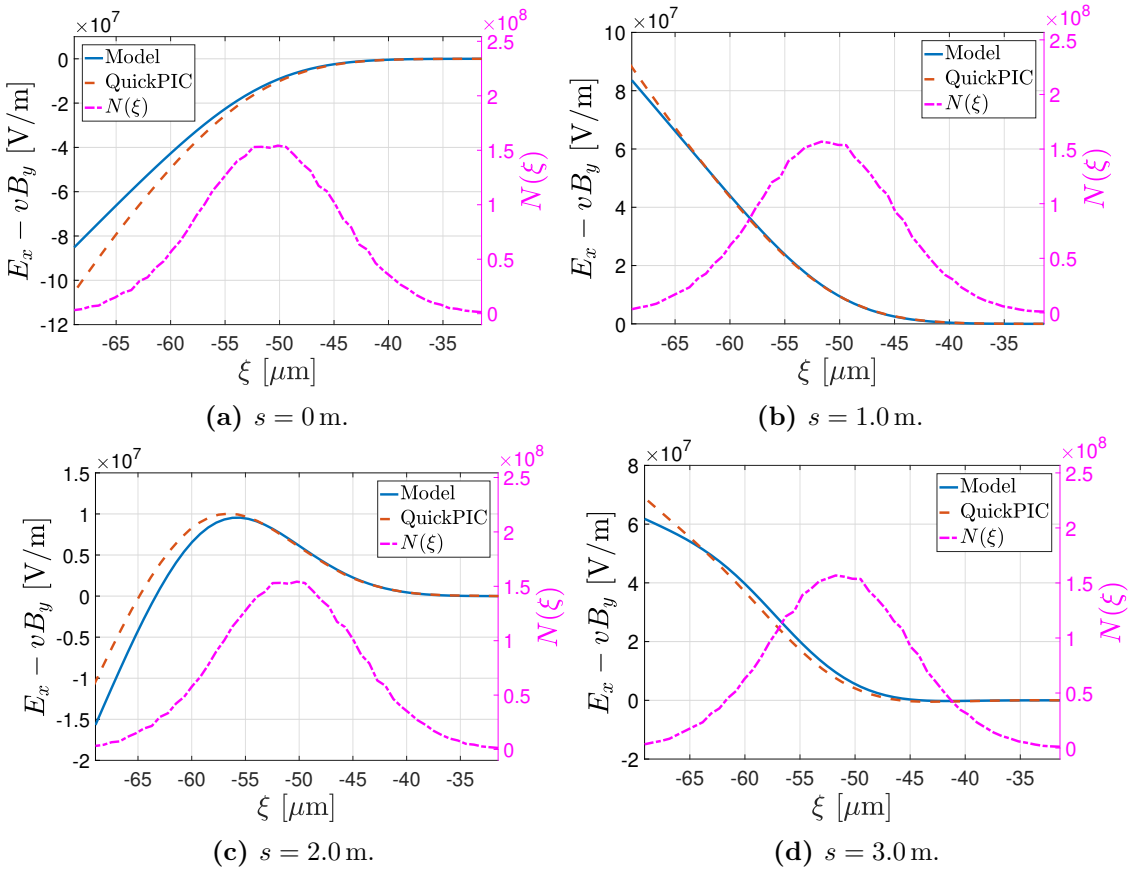

(a) $s = 0\,\mathrm{m}$. **(b)** $s = 1.0\,\mathrm{m}$. **(c)** $s = 2.0\,\mathrm{m}$. **(d)** $s = 3.0\,\mathrm{m}$.

Figure 3.3: The transverse wakefield calculated using equation (2.126) and (2.127). $N(\xi)$ is the beam particle number at ξ, and is extracted from QuickPIC simulation results along with $X(\xi, s)$. The model is compared to corresponding fields extracted from QuickPIC simulations at several propagation distances s.

In addition, the evolution of the transverse force in s is benchmarked against QuickPIC simulation results for three beam slices. $\lambda(\xi)$ and $X(\xi)$ in equation (2.127) are extracted from QuickPIC simulations, and the transverse force predicted by the convolution integral is then compared against the corresponding fields extracted from QuickPIC results. Figure 3.4a-3.4c show the evolution of the transverse wake on beam slices located 0-2 σ_z behind the main beam center.

The transverse wakefield given by equation (2.126) and (2.127) tends to slightly overestimate positive oscillation amplitudes and underestimate negative oscillation amplitudes, but achieves a good overall agreement with simulations.

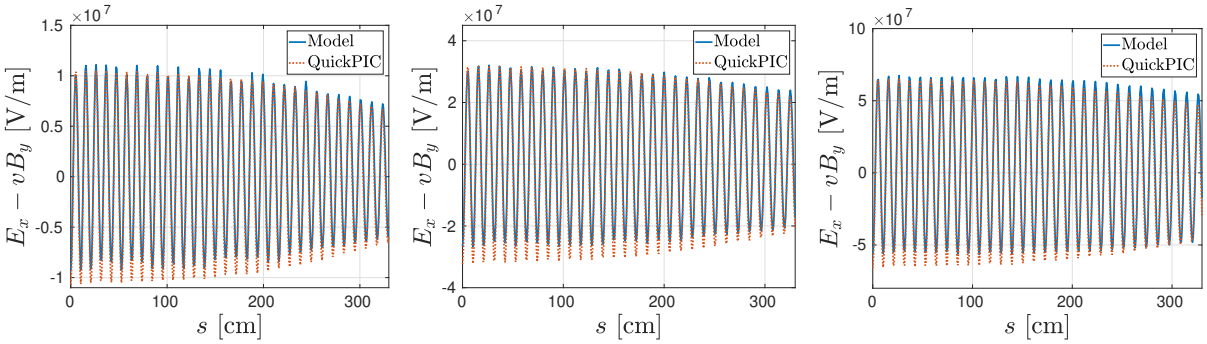

(a) Beam centre.

(b) One σ_z behind the beam centre.

(c) $2\sigma_z$ behind the beam centre.

Figure 3.4: Evolution of the transverse wake field at various positions along the beam. The fields extracted from QuickPIC are measured on axis.

For comparison, we also considered the wake function from reference [64]

$$W_r(\xi' - \xi) = \frac{2}{\pi\varepsilon_0} \frac{\xi' - \xi}{r_\mathrm{b}(\xi) r_\mathrm{b}^3(\xi')} \Theta(\xi' - \xi), \tag{3.9}$$

where ξ' and ξ are defined in the same way as in equation (2.126) and $r_\mathrm{b}(\xi')$ and $r_\mathrm{b}(\xi)$ are the plasma bubble radius at the driving particle and trailing particle's locations, respectively. The corresponding benchmarking results are displayed in figure 3.5a-3.5d, which exhibit a significantly larger disagreement with simulations than the results obtained with Stupakov's wake function.

3.1.3 Benchmarking the simplified quasi-static model with QuickPIC

Equation (2.127) and (3.8) were solved numerically with the quasi-static approximation, where the main beam is evolved in s, alternating between propagation with frozen transverse forces and interaction with the plasma ion bubble through equation (2.127) and (2.125), where the transverse forces were updated.

This model was benchmarked against QuickPIC by comparing the mean transverse offset of several beam slices with initial transverse offset X_0. The results are shown in figure 3.6a-3.6e. The simplified model agrees very well with the simulation results both in phase and amplitude as long as the main assumptions are valid. As expected, the transverse deflection grows along the beam so that slices towards the beam tail are deflected more violently as the beam propagates along s, while the wakefield close to the front of the beam is too weak to perturb the betatron oscillations significantly.

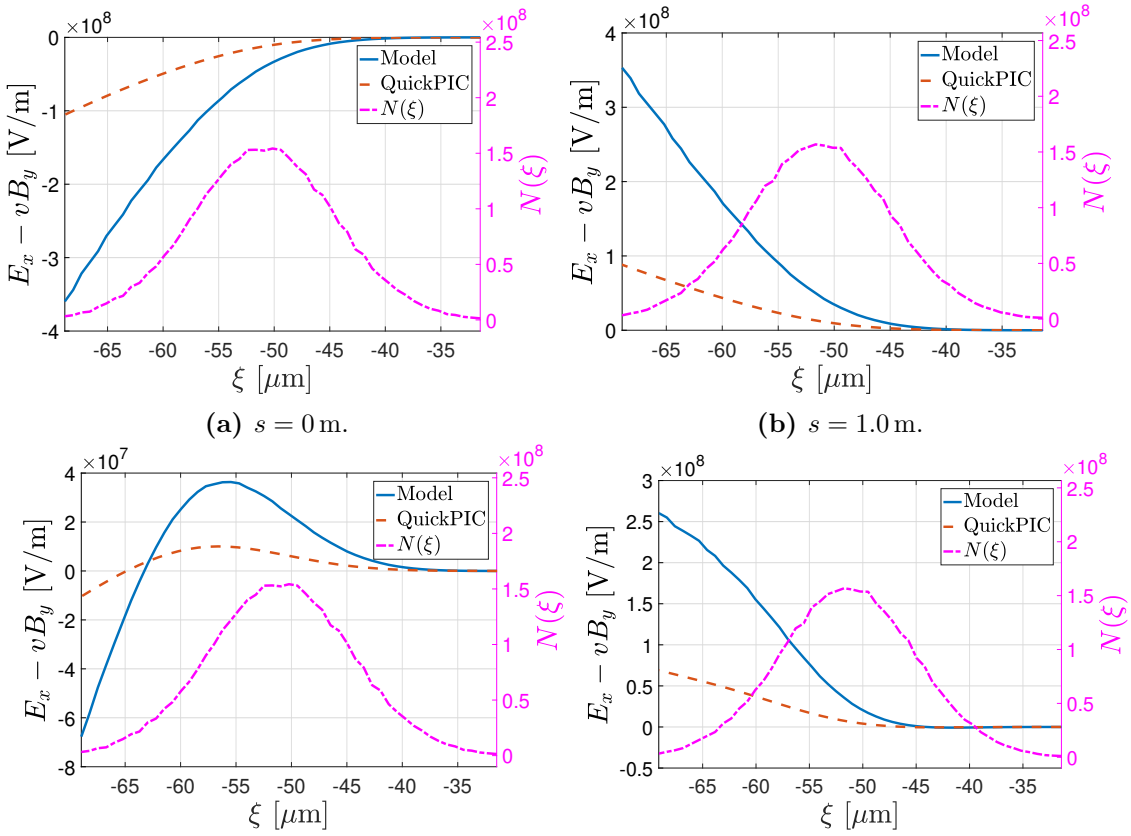

(a) $s = 0\,\mathrm{m}$. **(b)** $s = 1.0\,\mathrm{m}$.

(c) $s = 2.0\,\mathrm{m}$. **(d)** $s = 3.0\,\mathrm{m}$.

Figure 3.5: The transverse wakefield calculated using equation (3.9) and (2.127). $N(\xi)$ is the beam particle number at ξ, and is extracted from QuickPIC simulation results along with $X(\xi, s)$. The model is compared to corresponding fields extracted from QuickPIC simulations at several propagation distances s.

This benchmarking also indicates the significant speed-up achieved using the simplified model. In order to obtain results for the benchmarking shown in figure 3.6a-3.6e, calculations in QuickPIC required ~ 650 CPU hours, while calculations using the simplified model only required ~ 80 CPU seconds.

3.2 Damping mechanisms

In the design of CLIC [27], beam breakup due to short range wakefields are known to put a constrain on the maximum beam charge and consequently also limits efficiency and luminosity. Thus, understanding of the transverse instabilities and relevant mitigation mechanisms is one of the main components towards obtaining an improved estimate of the efficiency of a PWFA linear collider. In this section, we will give a brief outline of some relevant mitigation mechanisms.

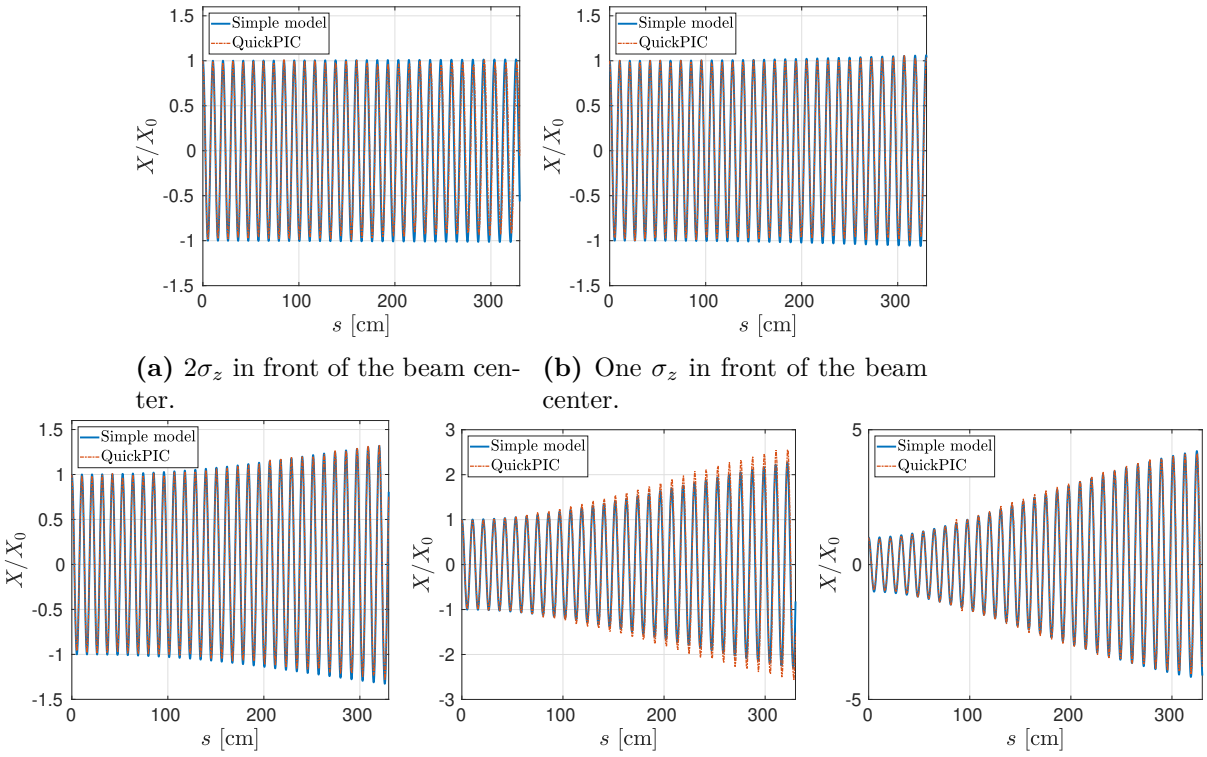

(a) $2\sigma_z$ in front of the beam center.

(b) One σ_z in front of the beam center.

(c) Beam center.

(d) One σ_z behind the beam center.

(e) $2\sigma_z$ behind the beam center.

Figure 3.6: Comparison of QuickPIC simulations results against simplified model calculations of the mean transverse position of main beam slices located at various positions.

3.2.1 Adiabatic damping

As the energy of the beam increases, the beam becomes more rigid, and less susceptible to being kicked transversely by the transverse wakefield. This phenomenon is termed adiabatic damping, and is outlined in reference [59] for metallic cavities. For simplicity, we consider a two-particle model where each macroparticle has charge $-Ne/2$ and are separated by $\Delta\xi$. In the case of no acceleration, equation (3.8) gives

$$\frac{\partial^2}{\partial s^2}X_2(s) + k_\beta^2 X_2(s) = \frac{Ne^2 W_r(\Delta\xi)}{2\mathscr{E}}X_1(s), \tag{3.10}$$

where X_i is the transverse offset of slice i. The leading macroparticle is not affected by any transverse wakefield and thus undergoes a free betatron oscillation

$$X_1(s) = X_0\cos(k_\beta s), \tag{3.11}$$

while the trailing macroparticle sees a transverse wakefield generated by the leading macroparticle. The solution for equation (3.10) is then

$$X_2(s) = X_0\cos(k_\beta s) + Y(s)X_0\sin(k_\beta s), \tag{3.12}$$

where the second term describes the resonant response of the trailing particle to the transverse wakefield, and has an amplitude that grows linearly with s described by the

dimensionless growth parameter

$$Y(s) = \frac{Ne^2 W_r(\Delta\xi)}{4k_\beta \gamma m_\mathrm{e} c^2} s. \tag{3.13}$$

Assuming uniform acceleration rate

$$\gamma = \gamma_0 \left(1 - \frac{eE_z}{\gamma_0 m_\mathrm{e} c^2} s\right) = \gamma_0 (1 - g_\gamma s) \tag{3.14}$$

with initial Lorentz factor γ_0, the equations of motion for the macroparticles become

$$\frac{\partial^2}{\partial u^2} X_1 + \frac{1}{u}\frac{\partial}{\partial u} X_1 + \left(\frac{k_\beta}{g_\gamma}\right)^2 X_1 = 0 \tag{3.15}$$

$$\frac{\partial^2}{\partial u^2} X_2 + \frac{1}{u}\frac{\partial}{\partial u} X_2 + \left(\frac{k_\beta}{g_\gamma}\right)^2 X_2 = \frac{Ne^2 W_r(\Delta\xi)}{2\gamma_0 m_\mathrm{e} c^2 g_\gamma^2 u} X_1, \tag{3.16}$$

where we have performed the substitution $u = 1 - g_\gamma s$.

In most cases of interest, $k_\beta \gg g_\gamma$ [i], and it can be shown [59] that

$$X_1 \approx \frac{X_0}{\sqrt{1 - g_\gamma s}} \cos(k_\beta s) \tag{3.17}$$

$$X_2 \approx \frac{X_0}{\sqrt{1 - g_\gamma s}} \left(\cos(k_\beta s) - \frac{Ne^2 W_r(\Delta\xi)}{4k_\beta \gamma_0 m_\mathrm{e} c^2 g_\gamma} \ln(1 - g_\gamma s) \sin(k_\beta s)\right), \tag{3.18}$$

with the growth parameter now given by

$$Y = -\frac{Ne^2 W_r(\Delta\xi)}{4k_\beta \gamma_0 m_\mathrm{e} c^2 g_\gamma} \ln \frac{\gamma(s)}{\gamma_0}, \tag{3.19}$$

which shows that in addition to damping the unperturbed betatron motion with a factor $1/\sqrt{1 - g_\gamma s}$, the oscillation amplification compared to the leading particle now grows logarithmically instead of linearly with s. Note that this expression can also be derived from equation (3.13) by replacing s/γ with $\int_0^s \mathrm{d}s'/\gamma(s')$.

3.2.2 BNS damping

A common mitigation technique for the BBU instability is BNS (Balakin, Novokhatsky and Smirnov) damping [75], where additional focusing is introduced along a beam in order to change the betatron frequency of each longitudinal slice of the beam. This will then mitigate the resonant build-up of transverse oscillations. We consider a slice at ξ with

[i] For instance, for $E_z = 10\,\mathrm{GV/m}$, $\gamma_0 = 48924$, $n_0 = 2 \cdot 10^{16}\,\mathrm{cm}^{-3}$ and $\gamma = 5.87 \cdot 10^6$, $g_\gamma/k_\beta = 0.05$.

betatron wave number $k_{\beta\mathrm{H}} + \Delta k_\beta$. For simplicity, we consider a case without acceleration so that $\partial_s \gamma = 0$. The driven harmonic oscillation equation (3.8) yields

$$\frac{\partial^2}{\partial s^2} X(\xi, s) + (k_{\beta\mathrm{H}} + \Delta k_\beta)^2 X(\xi, s) = -\frac{e}{\mathscr{E}(\xi)} \mathcal{W}_r(\xi, s). \tag{3.20}$$

The first slice does not experience any driving force, and undergoes a betatron oscillation $X(\xi_\mathrm{H}, s) = x_0 \cos(k_{\beta\mathrm{H}} s)$. We want the BNS damping to mitigate the resonant build-up, so that the entire beam undergoes the same betatron oscillation as the first slice. The main idea of the BNS damping mechanism is to introduce a stronger betatron focusing strength at the back of the beam in order to compensate the beam breakup mechanism of the beam head resonantly driving the beam tail. Physically, the stabilisation is due to the additional external focusing force compensating for the defocusing dipole deflection force caused by the wake field left behind by the preceding particles.

Under the BNS condition, all slices exhibit the same betatron oscillation. Our desired solution to equation (3.20) is therefore $X(\xi, s) = X(s) = x_0 \cos(k_{\beta\mathrm{H}} s)$, which yields

$$-k_{\beta\mathrm{H}}^2 + (k_{\beta\mathrm{H}} + \Delta k_\beta)^2 = \frac{e^2}{\mathscr{E}} w \tag{3.21}$$

$$\frac{1}{2} \left(\frac{\Delta k_\beta}{k_{\beta\mathrm{H}}} \right)^2 + \frac{\Delta k_\beta}{k_{\beta\mathrm{H}}} = \frac{e^2 w}{2 k_{\beta\mathrm{H}}^2 \mathscr{E}}, \tag{3.22}$$

where

$$w(\xi) = \int_{\xi_\mathrm{H}}^{\xi} W_r(\xi' - \xi) \lambda(\xi') \, \mathrm{d}\xi'. \tag{3.23}$$

Assuming $\Delta k_\beta / k_{\beta\mathrm{H}} \ll 1$, we obtain the BNS focusing criteria

$$\frac{\Delta k_\beta}{k_{\beta\mathrm{H}}}(\xi) = \frac{e^2 w(\xi)}{2 k_{\beta\mathrm{H}}^2 \mathscr{E}(\xi)} = \frac{e^2}{2 k_{\beta\mathrm{H}}^2 \mathscr{E}(\xi)} \int_{\xi_\mathrm{H}}^{\xi} W_r(\xi' - \xi) \lambda(\xi') \, \mathrm{d}\xi'. \tag{3.24}$$

This additional focusing effectively compensates for the defocusing dipole deflection force caused by the transverse wakefield left behind by the preceding particles.

In addition to providing BNS damping by using focusing components that changes its strength as the beam pass by, BNS damping can also be achieved by introducing an energy spread along the beam in which the tail of the beam gains less energy than the head. This can be accomplished by placing the beam at an appropriate phase of the longitudinal wakefield, such that the beam tail is accelerated by a weaker field than the head.

In practice, an uncorrelated energy spread along the beam can also have a damping effect. Furthermore, in addition to adiabatic damping and BNS damping, moderate amount of ion motion has also been proposed as a damping mechanism for mitigating hose instability [76, 77], as well as using a tailored plasma density transition before the acceleration stage [77]. More recent models can be found in reference [71, 72].

3.3 Parameter study using beam loading

Several conceptual parameter sets for a PWFA linear collider have been proposed to identify the main challenges and base parameters, one example being the Snowmass parameter set [78, 41]. The PWFA linear collider concept outlined in reference [41] represents an attempt to propose a reasonable preliminary design that can be used to identify the critical parameters and necessary R&D to address their feasibility. The design takes advantage of the extensive studies that has been performed for conventional RF linear colliders such as ILC and CLIC.

However, in contrast to CLIC, the effect of transverse wakefields on efficiency has so far not been taken into account in PWFA linear collider parameter studies, even though Lebedev et al. have studied the relationship between efficiency and instability, and derived an analytical expression [64]

$$\eta_\mathrm{t} \approx \frac{\eta_\mathrm{p}^2}{4(1-\eta_\mathrm{p})}, \tag{3.25}$$

where η_t is the ratio of the transverse wake deflecting force to the focusing force and η_p is the power transfer efficiency from a drive to a trailing beam. In deriving this expression, it was however assumed that both the drive beam and trailing beams have trapezoidal current profiles, which result in constant longitudinal fields according to beam-loading theory [79].

In this section, we will conduct a parameter study of the efficiency of a 1.5 TeV plasma wakefield linac using the Snowmass parameter set [78] as a basis. A summary of the Snowmass parameter set with transformer ratio $T = 1$ is shown in table 3.2. This study will take into account transverse wakefields and the damping effect of non-linear energy spread caused by a loaded longitudinal wakefield, using the approach of a parameter scan with Gaussian beam profiles.

The range of the parameter scan is $2 \cdot 10^9 \leq N \leq 10^{10}$, $160\,\mu\mathrm{m} \leq \Delta\xi \leq 210\,\mu\mathrm{m}$, while the range for σ_z was adjusted for different N in order to localise the minimum energy spread in the σ_z–$\Delta\xi$ plane. For each combination of N, σ_z and $\Delta\xi$, the main beam parameter scan only used results from the first time step of QuickPIC simulation as input, where the main beam was initially transversely offset by $X_0 = 3.65\,\mu\mathrm{m}$. From the QuickPIC results, we extracted $E_z(\xi)$ to accelerate the main beam and calculate the associated energy spread. Furthermore, $r_\mathrm{b}(\xi)$ and $\lambda(\xi)$ were extracted to calculate the transverse wakefield using

Parameter	Symbol	Unit	Value
Plasma density	n_0	$10^{16}\,\mathrm{cm}^{-3}$	2
Drive beam particle number	N_{DB}	10^9	20
rms drive beam beam length	$\sigma_{z\mathrm{DB}}$	µm	40
Main beam particle number	N	10^9	10
rms main beam beam length	σ_z	µm	20
Beam separation distance	$\Delta\xi$	µm	187
Matched rms horizontal beam size	σ_x	µm	0.69
Matched rms vertical beam size	σ_y	µm	0.69
Normalised horizontal emittance	$\gamma\varepsilon_x$	mm mrad	2
Normalised vertical emittance	$\gamma\varepsilon_y$	mm mrad	2
Initial Lorentz factor	γ_0		48924
Efficiency	η	%	50

Table 3.2: Summary of Snowmass $T = 1$ parameters.

equation (2.126) and (2.127). Equation (3.8) was then solved to model the main beam transverse dynamics and evolve the transverse wakefield using equation (2.127). In the parameter study, we made the optimistic assumption that no additional perturbation are introduced between the acceleration stages, so that all acceleration stages can be merged together and treated as a single stage.

3.3.1 Evaluation of the Snowmass parameter set

Figure 3.7 compares results from a QuickPIC simulation against the simplified model using the Snowmass parameter set. The QuickPIC results show that the Snowmass parameter set produced a highly unstable main beam, and eventually caused the tail of the main beam to come into contact with the bubble boundary. It can be seen that the simplified model and QuickPIC were in good agreement until the beam tail penetrated the plasma at $s \approx 140\,\mathrm{cm}$, as is depicted in figure 3.8, after which the transverse motion of the beam could not be described by equation (3.8). Such unstable cases are however irrelevant for this study, as the objective is to find a set of parameters for a stable main beam, and not to model highly unstable oscillations.

Nonetheless, because of the unstable beam, the Snowmass parameter set has to be modified in order to achieve stable propagation with high efficiency and low energy spread. This is done in subsequent sections, where we conduct a parameter study of a 1.5 TeV plasma wakefield accelerator using the Snowmass parameter set as a basis.

3.3.2 Energy spread

By varying the number of particles N, rms beam length σ_z and the separation distance $\Delta\xi$ between drive beam and main beam, the beam loading effect will lead to a loaded E_z

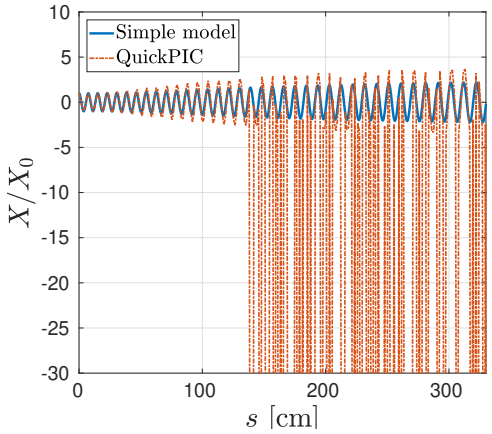

Figure 3.7: Comparison of QuickPIC simulations results against simplified model calculations of the mean transverse position of the main beam slice located at the centre of the beam. The Snowmass parameters were used in this simulation, and resulted in a highly unstable main beam after the beam tail came into contact with the bubble boundary at $s \approx 140\,\text{cm}$, as seen in figure 3.8. The transverse motion for $s > 140\,\text{cm}$ can thus not be described with equation (3.8).

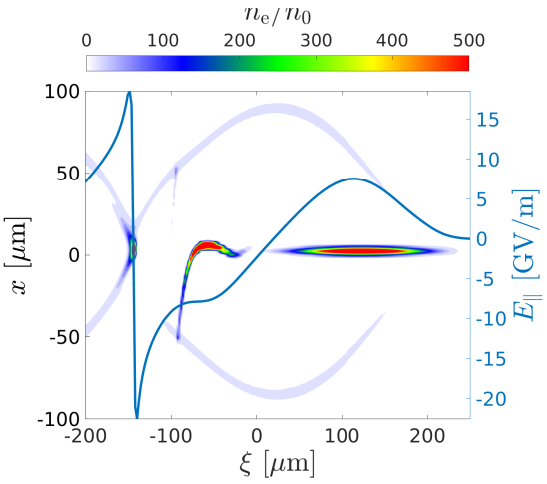

Figure 3.8: Electron number density n_e per unit initial plasma density n_0 and the longitudinal electric field at $s \approx 140\,\text{cm}$ obtained from QuickPIC simulation with Snowmass parameters. The plasma electron density has been increased by a factor 10 in order to highlight the bubble boundary.

with different shapes, and hence also a different energy spread. This is demonstrated in figure 3.9a-3.9i.

Using $E_z(\xi)$ obtained from QuickPIC, we can obtain the energy spread as a function of propagation distance s if we assume that the longitudinal field E_z remain unchanged during the entire acceleration process. For a beam with N particles divided into n

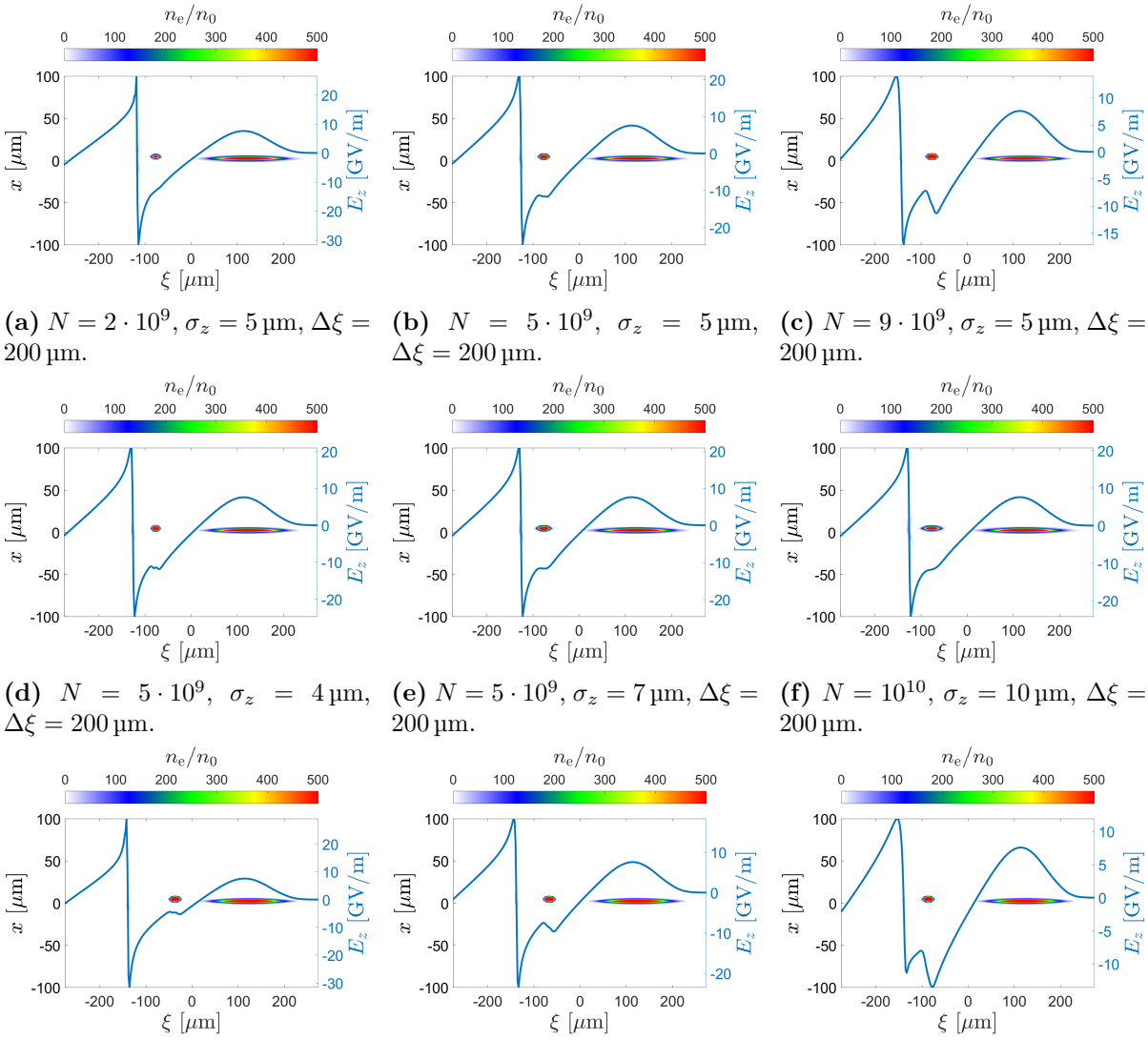

(a) $N = 2 \cdot 10^9$, $\sigma_z = 5\,\mu\text{m}$, $\Delta\xi = 200\,\mu\text{m}$. **(b)** $N = 5 \cdot 10^9$, $\sigma_z = 5\,\mu\text{m}$, $\Delta\xi = 200\,\mu\text{m}$. **(c)** $N = 9 \cdot 10^9$, $\sigma_z = 5\,\mu\text{m}$, $\Delta\xi = 200\,\mu\text{m}$.

(d) $N = 5 \cdot 10^9$, $\sigma_z = 4\,\mu\text{m}$, $\Delta\xi = 200\,\mu\text{m}$. **(e)** $N = 5 \cdot 10^9$, $\sigma_z = 7\,\mu\text{m}$, $\Delta\xi = 200\,\mu\text{m}$. **(f)** $N = 10^{10}$, $\sigma_z = 10\,\mu\text{m}$, $\Delta\xi = 200\,\mu\text{m}$.

(g) $N = 8 \cdot 10^9$, $\sigma_z = 5\,\mu\text{m}$, $\Delta\xi = 160\,\mu\text{m}$. **(h)** $N = 8 \cdot 10^9$, $\sigma_z = 5\,\mu\text{m}$, $\Delta\xi = 190\,\mu\text{m}$. **(i)** $N = 8 \cdot 10^9$, $\sigma_z = 5\,\mu\text{m}$, $\Delta\xi = 210\,\mu\text{m}$.

Figure 3.9: QuickPIC simulations with different combinations of main beam particle number N, rms beam length σ_z and separation distance $\Delta\xi$ between drive beam and main beam. The electron density n_e is plotted together with the longitudinal field E_z. Beams such as those shown in figure 3.9b, 3.9d and 3.9e have flattened E_z over large parts of the beam through beam loading, and have low energy spreads.

longitudinal slices, the weighted average longitudinal field is given by

$$\langle E_z \rangle = \frac{1}{N} \sum_{i=1}^{n} N_i E_{zi}, \tag{3.26}$$

where N_i is the number of particles in slice i and E_{zi} is the longitudinal electric field experienced by a particle in slice i.

The energy of an electron in slice i is given by

$$\mathscr{E}_i = -eE_{zi}s + \mathscr{E}_{0i}, \tag{3.27}$$

where $\mathscr{E}_{0i}$ is the initial energy. The mean single particle energy is then given by

$$\langle\mathscr{E}\rangle = \frac{1}{N}\sum_{i=1}^{n} N_i\mathscr{E}_i = -e\langle E_z\rangle s + \langle\mathscr{E}_0\rangle. \tag{3.28}$$

The variance of energy is

$$\sigma_{\mathscr{E}}^2 = \frac{1}{N}\sum_{i=1}^{n} N_i\left(\mathscr{E}_i - \langle\mathscr{E}\rangle\right)^2 = \frac{1}{N}\sum_{i=1}^{n} N_i\left(-eE_{zli}s + e\langle E_z\rangle s + \mathscr{E}_{0i} - \langle\mathscr{E}_0\rangle\right)^2, \tag{3.29}$$

and for an initially monochromatic beam, $\mathscr{E}_{0i} = \langle\mathscr{E}_0\rangle$, this reduces to

$$\sigma_{\mathscr{E}}^2 = \frac{e^2s^2}{N}\sum_{i=1}^{n} N_i\left(\langle E_z\rangle - E_{zi}\right)^2. \tag{3.30}$$

The relative rms energy spread is given by

$$\frac{\sigma_{\mathscr{E}}}{\langle\mathscr{E}\rangle} = \frac{es}{\langle\mathscr{E}_0\rangle - e\langle E_z\rangle s}\sqrt{\frac{1}{N}\sum_{i=1}^{n} N_i\left(\langle E_z\rangle - E_{zi}\right)^2}. \tag{3.31}$$

Lastly, we obtain the final energy spread independent of the initial energy by letting $s \to \infty$

$$\frac{\sigma_{\mathscr{E}}}{\langle\mathscr{E}\rangle} = -\frac{1}{\langle E_z\rangle}\sqrt{\frac{1}{N}\sum_{i=1}^{n} N_i\left(\langle E_z\rangle - E_{zi}\right)^2}. \tag{3.32}$$

Thus, by using equation (3.32), the final energy spread can be extrapolated from the initial longitudinal field $E_z(\xi)$, assuming that $E_z(\xi)$ and the longitudinal particle number density $\lambda(\xi)$ do not change significantly during propagation. By extracting $E_z(\xi)$ from QuickPIC simulation results using various combinations of main beam particle number N, rms main beam beam length σ_z and beam separation distance $\Delta\xi$, we obtained a series of contour plots for $2 \cdot 10^9 \leq N \leq 10^{10}$ that provide an overview over the effect of N, σ_z and $\Delta\xi$ on the energy spread. These contour plots are shown in figure 3.10a-3.10i. This overview reveals the region of minimum energy spread in the σ_z–$\Delta\xi$ plane for various charges, which is crucial for the study of accelerator parameters. The distance between data points in the σ_z-direction is 1 µm, and 10 µm in the $\Delta\xi$-direction. This applies to all contour plots in this parameter study.

In the non-linear regime, Gaussian beams often behave similarly to a flat-top beam in terms of beam-loading [79]. From beam-loading theory [79], a flat-top beam achieves optimal beam-loading if its longitudinal particle density λ is given by

$$\lambda = \frac{n_0 R_{\mathrm{b}}^4}{8r_{\mathrm{bH}}^2}, \tag{3.33}$$

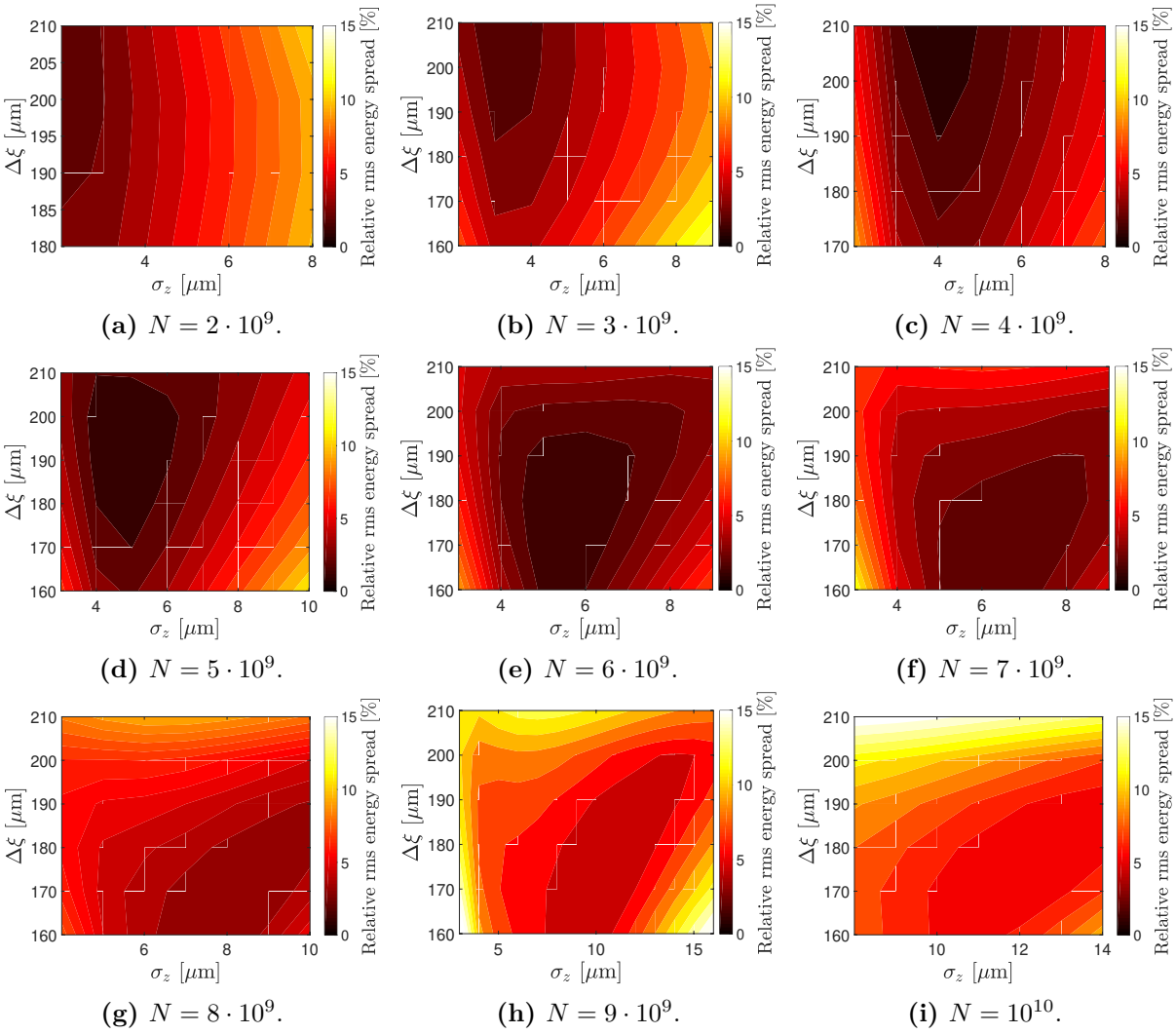

(a) $N = 2 \cdot 10^9$. **(b)** $N = 3 \cdot 10^9$. **(c)** $N = 4 \cdot 10^9$.

(d) $N = 5 \cdot 10^9$. **(e)** $N = 6 \cdot 10^9$. **(f)** $N = 7 \cdot 10^9$.

(g) $N = 8 \cdot 10^9$. **(h)** $N = 9 \cdot 10^9$. **(i)** $N = 10^{10}$.

Figure 3.10: Relative rms energy spread vs. beam separation distance $\Delta\xi$ and the rms beam length σ_z for main beams with various particle numbers N. The rest of the parameters are from the Snowmass parameter set.

where R_b is the maximum bubble radius and r_bH is the bubble radius at the head of the beam. Since r_bH increases with decreasing $\Delta\xi$, equation (3.33) implies that λ has to be reduced when the main beam is loaded close to the drive beam. If N is held constant, this requires that σ_z must be reduced in order to maintain optimal beam-loading and hence also minimal energy spread. This approximation seems to only hold partially for small N. E.g. for $N = 4 \cdot 10^9$ we see that to stay on the same level of energy spread when $\Delta\xi$ is reduced, one can increase σ_z. This however only holds for up to $\sigma_z = 4\,\mu\mathrm{m}$, after which σ_z has to be increased in order to maintain the same level of energy spread. Similar patterns can be seen in other sub figures in figure 3.10 for $2 \cdot 10^9 \leq N \leq 6 \cdot 10^9$.

3.3.3 Normalised amplitude

We now transform x and x' into normalised coordinates x_{N} and x'_{N} using the transformation

$$\begin{pmatrix} x_{\mathrm{N}}(s) \\ x'_{\mathrm{N}}(s) \end{pmatrix} = \sqrt{\frac{\gamma(s)}{\beta_x(s)\varepsilon_{\mathrm{N}x}}} \begin{pmatrix} 1 & 0 \\ \alpha_x(s) & \beta_x(s) \end{pmatrix} \begin{pmatrix} x(s) \\ x'(s) \end{pmatrix}. \tag{3.34}$$

By performing the inverse transformation

$$\begin{pmatrix} x(s) \\ x'(s) \end{pmatrix} = \sqrt{\frac{\varepsilon_{\mathrm{N}x}}{\gamma(s)\beta_x(s)}} \begin{pmatrix} \beta_x(s) & 0 \\ -\alpha_x(s) & 1 \end{pmatrix} \begin{pmatrix} x_{\mathrm{N}}(s) \\ x'_{\mathrm{N}}(s) \end{pmatrix} \tag{3.35}$$

and substituting x and x' into equation (2.13), we obtain

$$x_{\mathrm{N}} + x'_{\mathrm{N}} = 1. \tag{3.36}$$

This shows that the particle trajectory in phase space in normalised coordinates is a circle with radius 1 when considering a conservative system. Thus, the phase space trajectory for an unperturbed betatron motion in normalised coordinates is also a circle with radius 1.

For our cases of interest, $\alpha_x x \ll \beta_x x'$. Thus, for a beam divided into n slices each with transverse centroid position X_i and angle X'_i, the normalised amplitude defined as

$$\Lambda(s) = \sum_{i=1}^{n} (X_{\mathrm{N}i}(s)^2 + X'_{\mathrm{N}i}(s)^2) = \sum_{i=1}^{n} \left[\left(\frac{X_i(s)}{\sigma_x(s)} \right)^2 + \left(\frac{X'_i(s)}{\sigma_{x'}(s)} \right)^2 \right], \tag{3.37}$$

where

$$\sigma_x(s) = \sqrt{\frac{\beta(s)\varepsilon_{\mathrm{N}x}}{\gamma(s)}}, \quad \sigma_{x'}(s) = \sqrt{\frac{\varepsilon_{\mathrm{N}x}}{\gamma(s)\beta(s)}} \tag{3.38}$$

should therefore remain constant in the absence of transverse wakefields. When transverse wakefields perturb the betratron oscillation, the normalised amplification factor

$$\frac{\Lambda(s)}{\Lambda_0} = \frac{\sum_{i=1}^{n} (X_{\mathrm{N}i}(s)^2 + X'_{\mathrm{N}i}(s)^2)}{\sum_{i=1}^{n} (X_{\mathrm{N}i}(0)^2 + X'_{\mathrm{N}i}(0)^2)} \tag{3.39}$$

can thus be used to quantify the amplification of the transverse jitter of the incoming beam. We propose $\Lambda/\Lambda_0 \lesssim 10$ to be an acceptable level of amplification, but this rough criteria should be investigated by studying e.g. emittance growth at a later stage.

Analogously to energy spread, we obtained an overview of Λ/Λ_0 for different combinations of N, σ_z and $\Delta\xi$ from the parameter scan. The results for Λ/Λ_0 corresponding to a 1.5 TeV acceleration process are shown in figure 3.11.

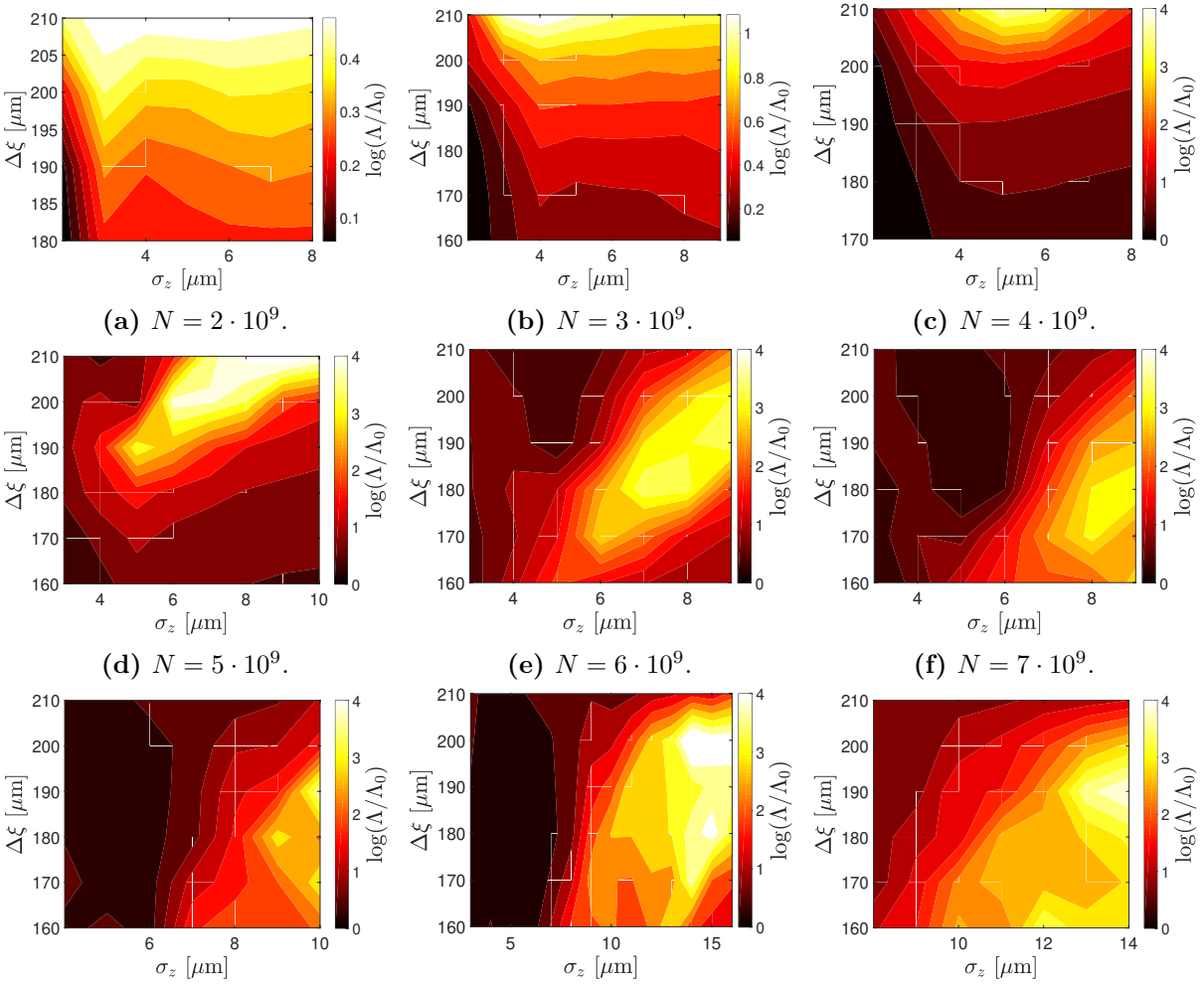

(a) $N = 2 \cdot 10^9$. **(b)** $N = 3 \cdot 10^9$. **(c)** $N = 4 \cdot 10^9$.

(d) $N = 5 \cdot 10^9$. **(e)** $N = 6 \cdot 10^9$. **(f)** $N = 7 \cdot 10^9$.

(g) $N = 8 \cdot 10^9$. **(h)** $N = 9 \cdot 10^9$. **(i)** $N = 10^{10}$.

Figure 3.11: Normalised amplification factor Λ/Λ_0 vs. beam separation distance $\Delta\xi$ and rms beam length σ_z for main beams with various particle numbers N. The rest of the parameters are from the Snowmass parameter set. The values of Λ/Λ_0 were extracted at the end of a 1.5 TeV acceleration process. Note that different colour scales have been used in some plots.

The effects from transverse wakefields are expected to become more apparent as N is increased. Since transverse wakefields grow along the beam, a long beam will lead to stronger perturbations of the betatron oscillations and a more unstable beam. Furthermore, larger values of $\Delta\xi$ implies smaller r_b, since the main beam is placed further towards the end of the bubble. This will then lead to smaller effective iris radii a and hence also stronger transverse wakefields and a more unstable beam. These patterns become evident for $N \geq 6 \cdot 10^9$, and the results in figure 3.11 are thus qualitatively consistent with theoretical considerations.

Note that we initially assumed that all parameters used in this parameter scan were able to generate main beams sufficiently stable to satisfy the basic assumptions for the simplified quasi-static model. As the procedure of this parameter scan did not terminate

beam propagation for the cases where the beam collided with the bubble boundary, large values of Λ/Λ_0 in figure 3.11 should be ignored.

For $N \geq 5 \cdot 10^9$, there are regions of large $\Delta\xi$ and small σ_z that can provide beam propagation with promising stability with $\log(\Lambda/\Lambda_0) \lesssim 1$. As will become evident in subsection 3.3.4, this region in the N–σ_z–$\Delta\xi$ parameter space can also provide high efficiency.

3.3.4 Efficiency

For a main beam with charge Q_{MB} accelerated in the wake excited by a drive beam with charge Q_{DB}, we define the drive beam to main beam efficiency as

$$\eta = \frac{\Delta\mathscr{E}_{\mathrm{MB}}}{\mathscr{E}_{\mathrm{DB}}} \frac{Q_{\mathrm{MB}}}{Q_{\mathrm{DB}}}, \tag{3.40}$$

where $\Delta\mathscr{E}_{\mathrm{MB}}$ is the energy gain of the main beam and $\mathscr{E}_{\mathrm{DB}}$ is the initial drive beam energy. This definition considers all the energy of the drive beam as spent regardless of how much energy has been extracted by the main beam. Assuming the drive beam's energy is fully depleted in a plasma of length L_{d}, the efficiency can also be written as

$$\eta = \frac{E_{\mathrm{A}} L_{\mathrm{d}}}{E_{\mathrm{D}} L_{\mathrm{d}}} \frac{Q_{\mathrm{MB}}}{Q_{\mathrm{DB}}} = T \frac{N_{\mathrm{MB}}}{N_{\mathrm{DB}}}, \tag{3.41}$$

where E_{D} is the peak decelerating field of the drive beam and E_{A} is the mean accelerating field of the main beam and $T = E_{\mathrm{A}}/E_{\mathrm{D}}$ is the transformer ratio.

Contour plots of the efficiency in the σ_z–$\Delta\xi$ plane for several N are shown in figure 3.12, which shows that regardless of N and σ_z, efficiency is increased by increasing $\Delta\xi$. This qualitatively agrees with theory, as the longitudinal field E_z is stronger towards the end of the plasma ion bubble.

It is therefore desirable to position the main beam as far behind in the bubble as possible in order to maximise the efficiency, but this will also lead to stronger transverse wakefields as explained earlier. Furthermore, placing the main beam at large $\Delta\xi$ may also lead to a large energy spread, as seen in figure 3.10.

3.3.5 Summary of parameter scan

An optimal set of parameters for an accelerator requires low values for $\sigma_{\mathscr{E}}/\langle\mathscr{E}\rangle$ and Λ/Λ_0, while high values of η are desirable. These requirements can be conflicting, as shown in figure 3.10, 3.11 and 3.12. In order to arrive at a reasonable compromise, the data for $\sigma_{\mathscr{E}}/\langle\mathscr{E}\rangle$, Λ/Λ_0 and η in the N–σ_z–$\Delta\xi$ parameter space are combined to obtain an overview shown in figure 3.13. The scatter plots in figure 3.13 summarise the results in figure 3.10, 3.11 and 3.12 to provide an overview of the relation between energy spread, stability and efficiency for several N.

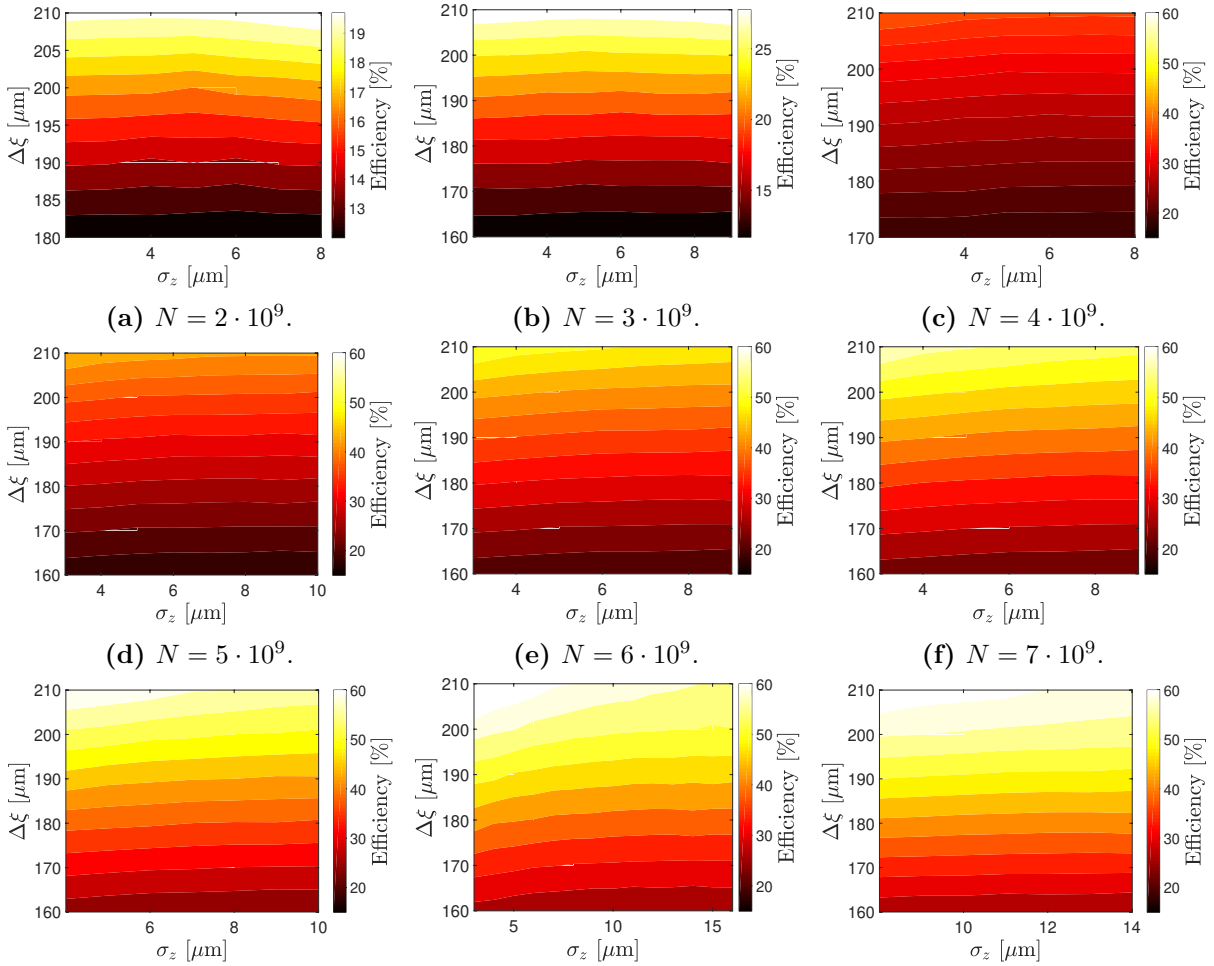

(a) $N = 2 \cdot 10^9$. **(b)** $N = 3 \cdot 10^9$. **(c)** $N = 4 \cdot 10^9$.

(d) $N = 5 \cdot 10^9$. **(e)** $N = 6 \cdot 10^9$. **(f)** $N = 7 \cdot 10^9$.

(g) $N = 8 \cdot 10^9$. **(h)** $N = 9 \cdot 10^9$. **(i)** $N = 10^{10}$.

Figure 3.12: Efficiency vs. beam separation distance $\Delta\xi$ and rms beam length σ_z for main beams with various particle numbers N. Note that different colour scales have been used in some plots.

For $N \geq 4 \cdot 10^9$, it is evident that good beam stability generally requires a large energy spread, and high efficiency combined with low energy spread tend to lead to an unstable beam. We can however find reasonable compromises, and our operating point of choice in figure 3.13d is marked with a red circle. The corresponding parameter set is summarised in table 3.3. The normalised emittances are based on the 3 TeV CLIC parameter set [27], where the normalised horizontal emittance has been increased proportionally due to the larger beam charge that is used here. Drive beam parameters are identical to the Snowmass $T = 1$ parameters summarised in table 3.2.

3.3.6 Performance improvements

The derived main beam parameters offer improvements over the Snowmass parameter set both in terms of energy spread and stability, but result in a lower efficiency. These parameters and results are summarised in table 3.4, where the energy spread for the

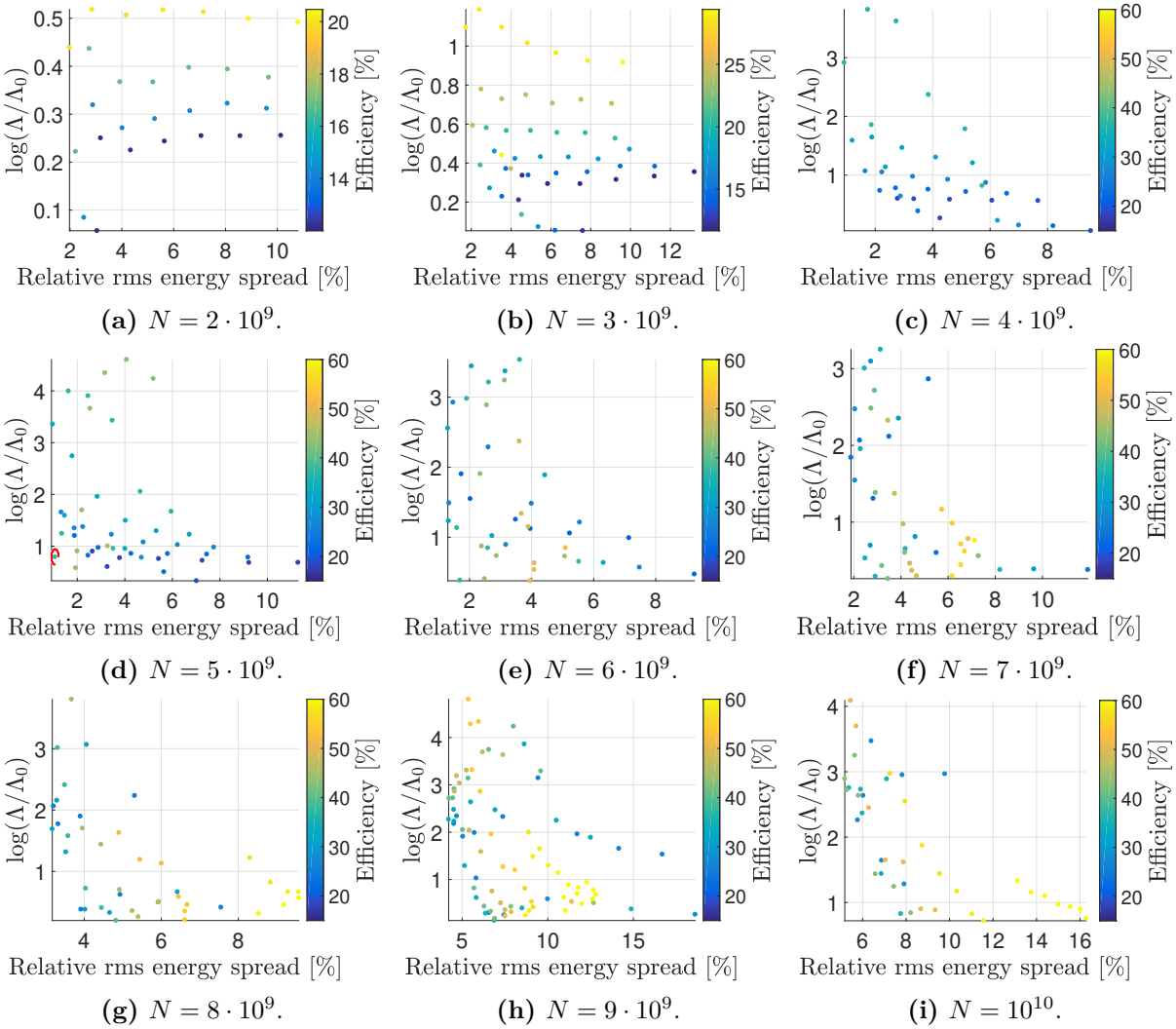

(a) $N = 2 \cdot 10^9$. **(b)** $N = 3 \cdot 10^9$. **(c)** $N = 4 \cdot 10^9$.

(d) $N = 5 \cdot 10^9$. **(e)** $N = 6 \cdot 10^9$. **(f)** $N = 7 \cdot 10^9$.

(g) $N = 8 \cdot 10^9$. **(h)** $N = 9 \cdot 10^9$. **(i)** $N = 10^{10}$.

Figure 3.13: Scatter plots displaying the relation between relative rms energy spread, normalised amplification factor and efficiency for main beams with several particle numbers. The chosen candidate for a main beam parameter set is marked with a red circle. Note that different colour scales have been used in some plots.

Snowmass parameter set has been re-calculated using the definition (3.32). The value for Λ/Λ_0 for the Snowmass parameters was obtained after accelerating the main beam to 1.5 TeV while ignoring the collision into the bubble boundary.

A PWFA multi-TeV accelerator can be envisioned being used as the main linac (linear accelerator) for a linear collider. A core metric of performance for a linear collider is luminosity per input power P_{AC}, which scales as

$$\mathcal{L}/P_{\mathrm{AC}} \propto \eta/\sqrt{\sigma_z} \tag{3.42}$$

when beamstrahlung has been taken into account. This scaling is shown in chapter 4. Assuming that the beam sizes can be appropriately adjusted (see chapter 4) for

Parameter	**Symbol**	**Unit**	**Value**
Plasma density	n_0	$10^{16}\,\mathrm{cm}^{-3}$	2.0
Particle number	N	10^9	5
rms beam length	σ_z	µm	5
Beam separation distance	$\Delta\xi$	µm	200
Normalised horizontal emittance	$\gamma\varepsilon_x$	mm mrad	0.887
Normalised vertical emittance	$\gamma\varepsilon_y$	mm mrad	0.02
Relative rms energy spread	$\sigma_{\mathscr{E}}/\langle\mathscr{E}\rangle$	%	1.1
Normalised amplification factor	Λ/Λ_0		6.2
Drive beam to main beam efficiency	η	%	37.5

Table 3.3: New parameter set for a 1.5 TeV PWFA linear e^- accelerator derived from the parameter scan.

	Unit	**Snowmass $T = 1$**	**New parameters**
N_{MB}	10^9	10.0	5.0
σ_z	µm	20.0	5.0
$\Delta\xi$	µm	187	200
$\sigma_{\mathscr{E}}/\langle\mathscr{E}\rangle$	%	12	1.1
Λ/Λ_0		670	6.2
η	%	50	37.5

Table 3.4: Comparison of the Snowmass $T = 1$ parameter set and the new parameter set.

the new parameter set, the luminosity per power is actually 1.5 times higher than the corresponding value provided by the Snowmass $T = 1$ parameters, even though the new parameter set offers a lower efficiency.

3.4 Parameter study using linear energy spread

In this section, we will present a parameter study for a PWFA electron accelerator that explores the potential for damping transverse instabilities using linear energy spread. The procedure is similar to section 3.3, where we scan over a range of N and σ_z, but instead of varying $\Delta\xi$ to change the shape of E_z using beam loading and consequently obtain a set of non-linear energy spread, we held $\Delta\xi$ constant and artificially introduced a linear longitudinal field of the form

$$E_z(\xi) = g(\xi - \xi_{\mathrm{H}}) + E_{z\mathrm{H}} \tag{3.43}$$

over the length of the main beam. Here ξ_{H} is the position of the beam head, $E_{z\mathrm{H}}$ is the longitudinal field at ξ_{H} and $g = \partial_\xi E_z$ is the slope of the longitudinal field.

In this parameter scan, we used energy spread as an input parameter and scanned over a

set of energy spread $0.5\% \leq \sigma_{\mathscr{E}}/\langle\mathscr{E}\rangle \leq 10\%$ for each combination of N and σ_z. g is then determined by the input energy spread as follows:

The mean E_z weighted by the number of particles in the beam slices is

$$\langle E_z\rangle = \frac{g}{N}\underbrace{\sum_{i=1}^{n} N_i(\xi_i - \xi_{\mathrm{H}})}_{S_1} + E_{z\mathrm{H}}. \tag{3.44}$$

The energy spread can be written as

$$\frac{\sigma_{\mathscr{E}}}{\langle\mathscr{E}\rangle} = -\frac{1}{\langle E_z\rangle}\sqrt{\frac{1}{N}\sum_{i=1}^{n} N_i(\langle E_z\rangle - E_{zi})^2} = -\frac{1}{gS_1/N + E_{z\mathrm{H}}}\sqrt{\frac{g^2}{N}\underbrace{\sum_{i=1}^{n}\left(\frac{S_1}{N} - \xi_i + \xi_{\mathrm{H}}\right)^2}_{S_2}}. \tag{3.45}$$

This can be rearranged to a quadratic equation in g,

$$\left[\left(\frac{S_1}{N}\frac{\sigma_{\mathscr{E}}}{\langle\mathscr{E}\rangle}\right)^2 - \frac{S_2}{N}\right] g^2 + 2E_{z\mathrm{H}}\frac{S_1}{N}\left(\frac{\sigma_{\mathscr{E}}}{\langle\mathscr{E}\rangle}\right)^2 g + \left(\frac{\sigma_{\mathscr{E}}}{\langle\mathscr{E}\rangle}E_{z\mathrm{H}}\right)^2 = 0, \tag{3.46}$$

which can be solved to obtain values for g corresponding to given beam slice particle distribution, $E_{z\mathrm{H}}$ and energy spread. For BNS damping, we choose the negative solution of equation (3.46) such that the beam tail gains less energy than the beam head.

The maximum beam separation distance in the QuickPIC data used in the parameter scan in section 3.3 is $\Delta\xi = 210\,\mu\mathrm{m}$, and we adopted this value throughout this parameter scan in order to maximise efficiency. For each combination of N and σ_z, we extracted $r_{\mathrm{b}}(\xi)$ and $E_{z\mathrm{H}}$ from the corresponding QuickPIC results to use as input in the simplified quasi-static model as before. An overview of g for different combinations of N, σ_z and $\sigma_{\mathscr{E}}/\langle\mathscr{E}\rangle$ is displayed in figure 3.14.

In contrast to the previous parameter study, here we terminated the beam dynamics calculations using the simplified quasi-static model if the beam collided into the plasma ion bubble boundary.

3.4.1 Results of parameter scan

An overview of the effects of N, σ_z and $\sigma_{\mathscr{E}}/\langle\mathscr{E}\rangle$ on Λ/Λ_0 is shown in figure 3.15. The distance between actual data points in the σ_z-direction is 1 µm, and 0.5 % in the $\sigma_{\mathscr{E}}/\langle\mathscr{E}\rangle$-direction. This applies to all contour plots in this parameter study.

There is an evident pattern of Λ/Λ_0 increasing with σ_z and decreasing with energy spread. As the transverse wakefield deflection is weaker for short beams, shorter beams can be

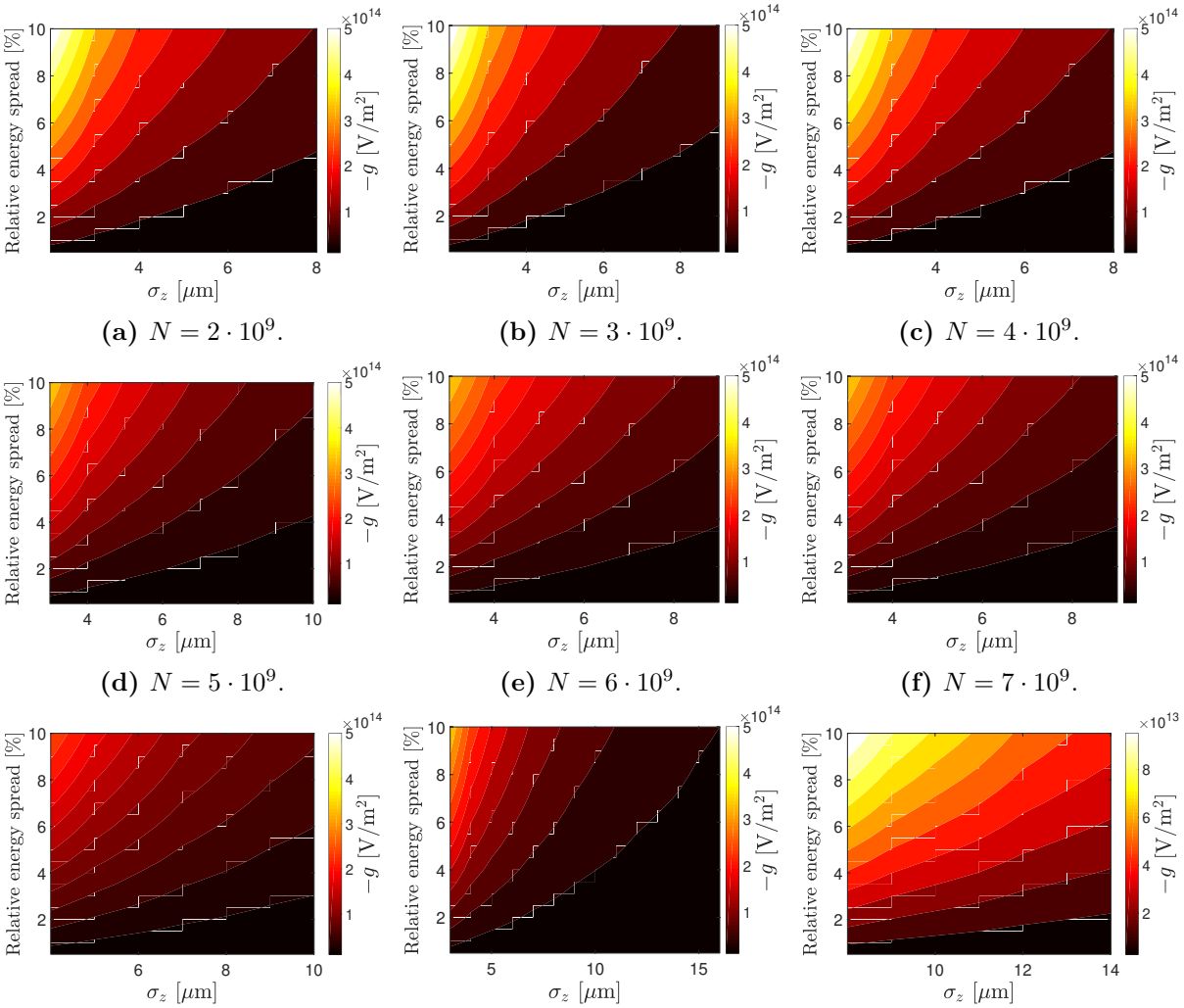

(a) $N = 2 \cdot 10^9$. **(b)** $N = 3 \cdot 10^9$. **(c)** $N = 4 \cdot 10^9$.

(d) $N = 5 \cdot 10^9$. **(e)** $N = 6 \cdot 10^9$. **(f)** $N = 7 \cdot 10^9$.

(g) $N = 8 \cdot 10^9$. **(h)** $N = 9 \cdot 10^9$. **(i)** $N = 10^{10}$.

Figure 3.14: An overview of the slope of the longitudinal field $g = \partial_\xi E_z$ for different combinations of beam particle number N, rms beam length σ_z and relative rms energy spread $\sigma_\mathscr{E}/\langle\mathscr{E}\rangle$. g is obtained using equation (3.46). Note that different colour scales have been used in some plots.

damped by a lower energy spread. This therefore results in the σ_z–$\sigma_\mathscr{E}/\langle\mathscr{E}\rangle$ plane being divided obliquely into a region with $\log(\Lambda/\Lambda_0) \lesssim 1$ and a region with $\log(\Lambda/\Lambda_0) \gtrsim 1$. As the transverse wakefield increases with N, the more stable $\log(\Lambda/\Lambda_0) \lesssim 1$ region also seems to become smaller, since a larger energy spread is required to damp the transverse oscillations.

Furthermore, the region $\log(\Lambda/\Lambda_0) \gtrsim 1$ corresponds to highly unstable main beams that all resulted in collision with the plasma ion bubble boundary. This is the cause for contours along the oblique boundary rising very steeply, and since the resolution in $\sigma_\mathscr{E}/\langle\mathscr{E}\rangle$ is 0.5 %, we see that stability is very sensitive to linear energy spread. For the $N = 10^{10}$ case, the parameter scan only returned unstable outcomes, but acceptable stability may

be possible with shorter beams.

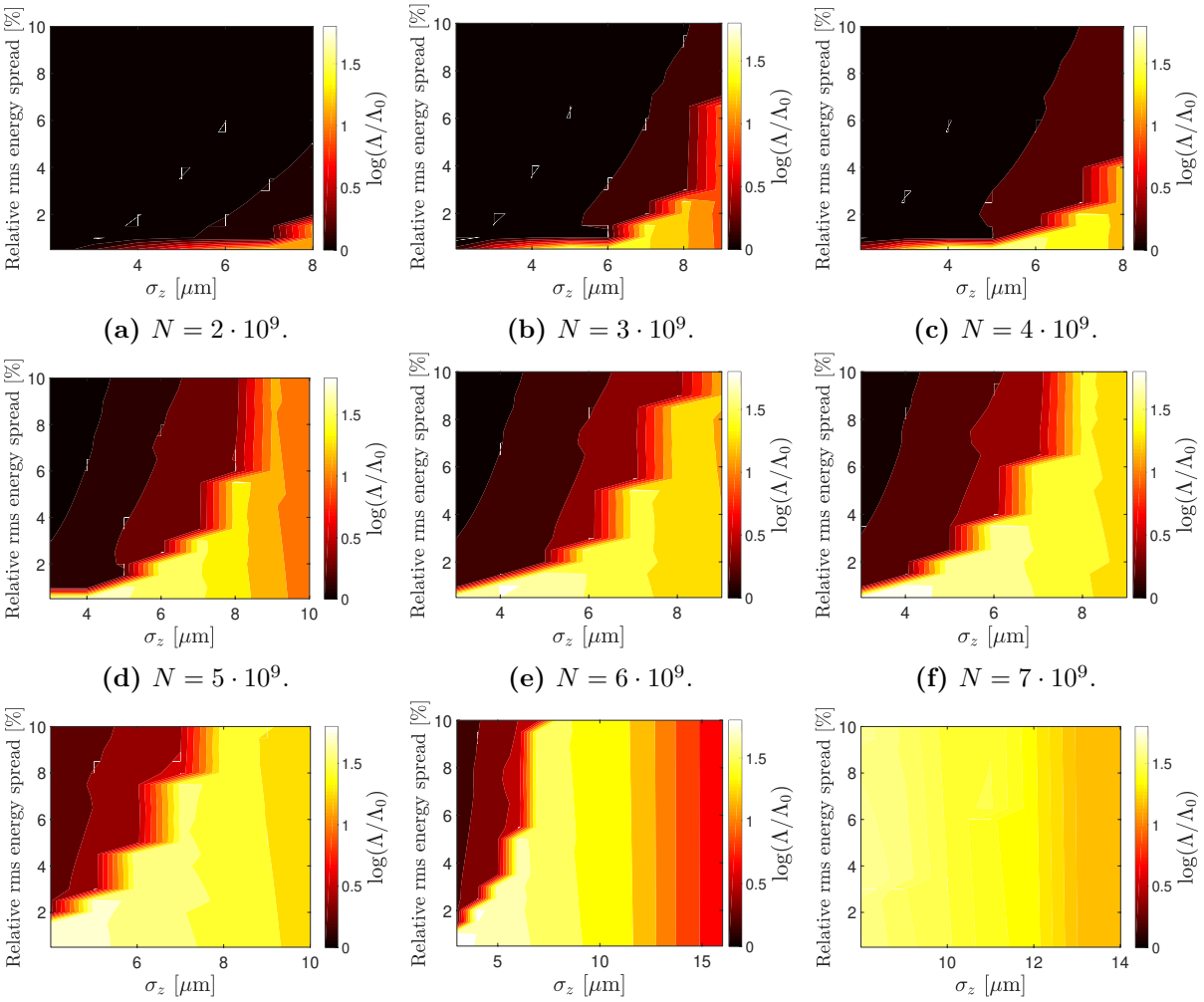

(a) $N = 2 \cdot 10^9$. **(b)** $N = 3 \cdot 10^9$. **(c)** $N = 4 \cdot 10^9$.

(d) $N = 5 \cdot 10^9$. **(e)** $N = 6 \cdot 10^9$. **(f)** $N = 7 \cdot 10^9$.

(g) $N = 8 \cdot 10^9$. **(h)** $N = 9 \cdot 10^9$. **(i)** $N = 10^{10}$.

Figure 3.15: Normalised amplification factor Λ/Λ_0 vs. relative rms energy spread and rms beam length σ_z for main beams with various particle numbers N.

For a fixed N, efficiency only depends on the average accelerating field, which in the case of linear energy spread mainly depends on the input energy spread and beam length. A smaller input energy spread and a shorter beam yield a stronger average accelerating field and hence also a higher efficiency. This can be partially seen in the scatter plots in figure 3.16, where data points with high values of efficiency are concentrated at low energy spread. The sharp boundary between acceptably stable and unstable propagation is also apparent in figure 3.16.

As in the parameter study in section 3.3, $N = 5 \cdot 10^9$ provides several high stability operating points with less than 2 % of energy spread and more than 30 % in efficiency. At larger N, it is possible to obtain operating points with good stability with less than 2 % of energy spread and even higher efficiency. $N = 7 \cdot 10^9$ can provide acceptably

stable propagation with low energy spread and $\eta \sim 60\,\%$, while $N = 9 \cdot 10^9$ can yield more than 70 % efficiency. However, figure 3.15h shows that the region for adequately stable beam and $\sigma_{\mathscr{E}}/\langle\mathscr{E}\rangle \leq 2\,\%$ is very small, so that the stability of operating points with $\sigma_{\mathscr{E}}/\langle\mathscr{E}\rangle \leq 2\,\%$ for $N = 9 \cdot 10^9$ should therefore be further verified.

Even though linear energy spread yields very promising results, it is not clear how to generate longitudinal fields of the form $E_z = g(\xi - \xi_{\mathrm{H}}) + E_{x\mathrm{H}}$ with $|g| \sim 10^{14}\,\mathrm{V/m^2}$, although a tuneable plasma dechirper with a maximum dechirping strength of 1.8 GeV/mm/m was successfully implemented in an experiment carried out at FLASHForward, DESY [80]. In the following chapters, we therefore focus on the parameter set in table 3.3.

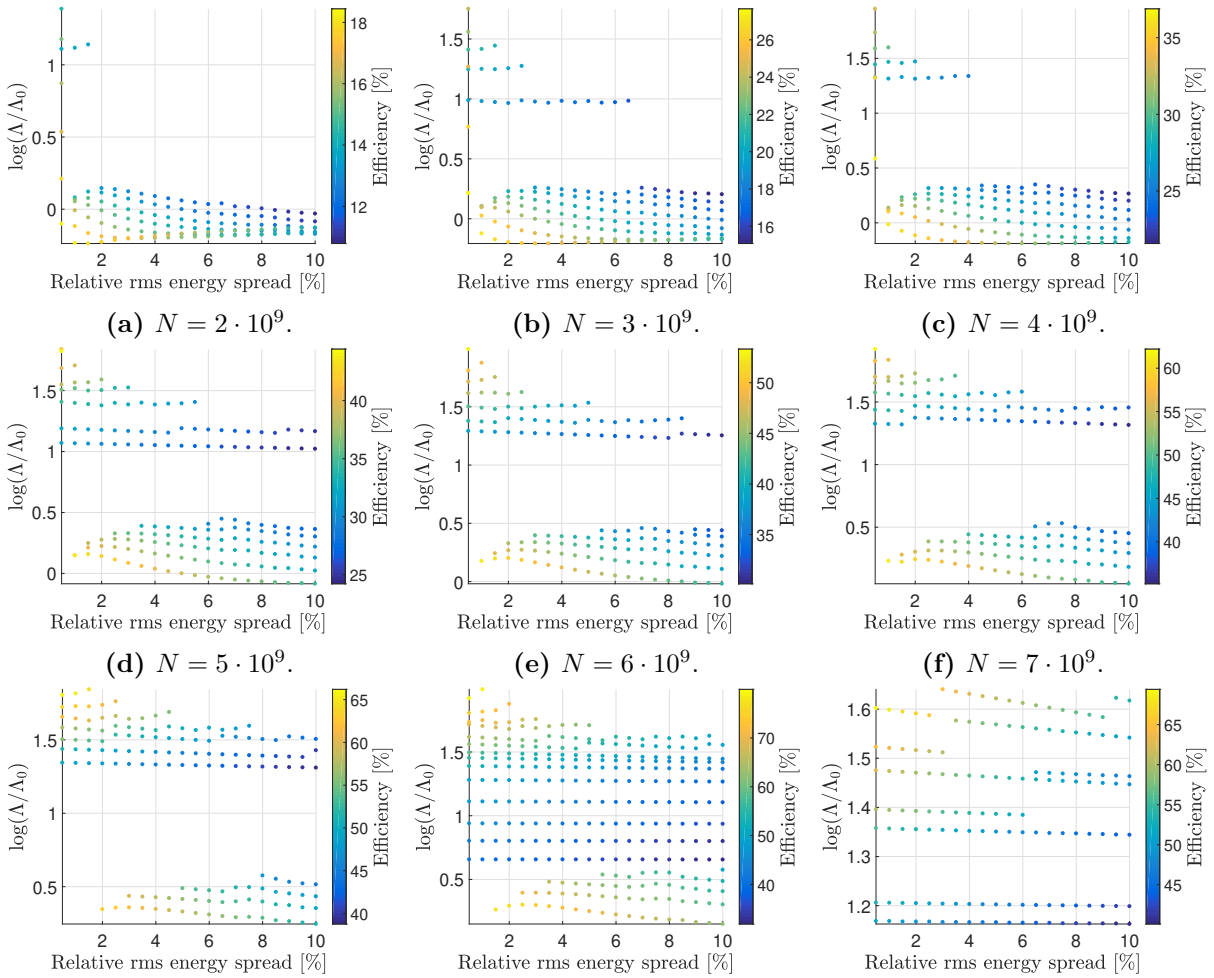

(a) $N = 2 \cdot 10^9$. **(b)** $N = 3 \cdot 10^9$. **(c)** $N = 4 \cdot 10^9$.

(d) $N = 5 \cdot 10^9$. **(e)** $N = 6 \cdot 10^9$. **(f)** $N = 7 \cdot 10^9$.

(g) $N = 8 \cdot 10^9$. **(h)** $N = 9 \cdot 10^9$. **(i)** $N = 10^{10}$.

Figure 3.16: Scatter plots showing the relation between relative rms energy spread, normalised amplification factor and efficiency for main beams with several particle numbers. Note that different colour scales have been used.

3.4.2 Comparison with the BNS damping requirement

Here we compare the energy spread threshold that gives acceptably stable propagation, seen in figure 3.15, to the BNS damping requirement given by equation (3.24). For most N-σ_z pairs, there is a minimum relative rms energy spread $\sigma_{\mathscr{E}}/\langle\mathscr{E}\rangle$ that gives an acceptable stability. These minimum values of $\sigma_{\mathscr{E}}/\langle\mathscr{E}\rangle$ form the sharp boundaries seen in figure 3.15.

In order to make the comparison, we first convert the boundary $\sigma_{\mathscr{E}}/\langle\mathscr{E}\rangle$ to a longitudinal field slope g using equation (3.46) for a given pair of N and σ_z. The head to tail energy spread is then given by

$$\frac{\Delta\gamma}{\gamma_{\mathrm{H}}} = \frac{\mathscr{E}(\xi_{\mathrm{T}}) - \mathscr{E}(\xi_{\mathrm{H}})}{\mathscr{E}(\xi_{\mathrm{H}})} = \frac{E_z(\xi_{\mathrm{T}}) - E_z(\xi_{\mathrm{H}})}{E_z(\xi_{\mathrm{H}})} = \frac{g}{E_{z\mathrm{H}}}(\xi_{\mathrm{T}} - \xi_{\mathrm{H}}), \tag{3.47}$$

where ξ_{T} is the longitudinal location of the beam tail. Lastly, this is converted into a betatron wave number spread through

$$\frac{\Delta k_\beta}{k_{\beta\mathrm{H}}} = \left(\frac{\Delta\gamma}{\gamma_{\mathrm{H}}} + 1\right)^{-1/2} - 1. \tag{3.48}$$

The comparison is shown in figure 3.17. Results for $N = 10^{10}$ are omitted, as no stable results were found for this charge in this parameter scan. The precision of this comparison is limited by factors such as the resolution of the parameter scan. Despite the $\sigma_{\mathscr{E}}/\langle\mathscr{E}\rangle$ resolution for the parameter scan being 0.5 %, we found reasonable agreement between the BNS damping requirement and the energy spread threshold for stability found in the parameter scan. Thus, for linear energy spread, equation (3.24) can be used to make estimates of minimum head to tail energy spread required for damping transverse instabilities.

In this chapter, we have presented possible working points for a 1.5 TeV PWFA linear electron accelerator. In particular, the parameter set derived in section 3.3 will be used in collider parameter studies in chapter 4 and 5. However, the parameter scans in this chapter are not exhaustive and the working points are expected to change in more detailed studies. In particular, damping from moderate ion motion is expected to affect the results significantly.

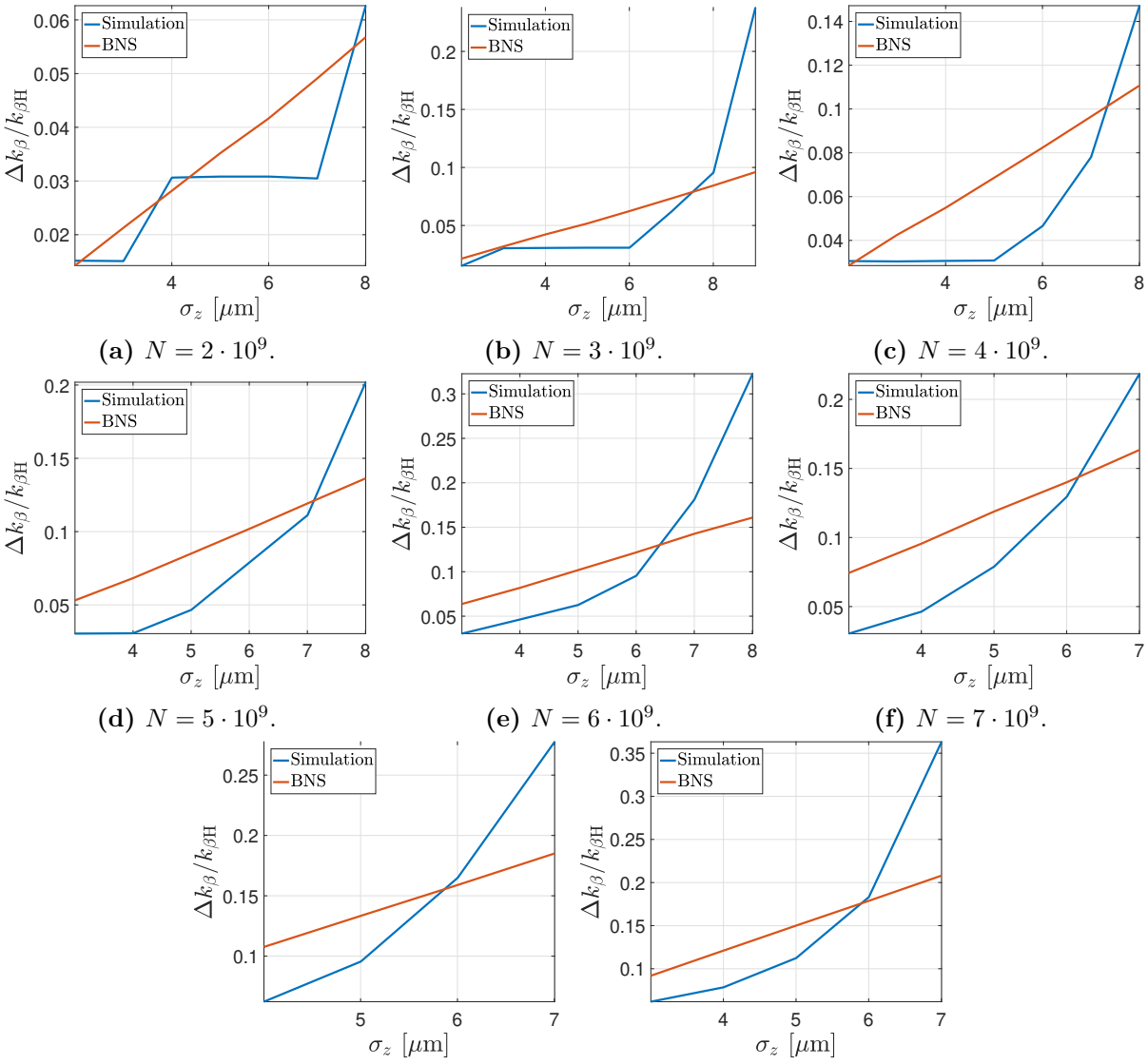

(a) $N = 2 \cdot 10^9$. **(b)** $N = 3 \cdot 10^9$. **(c)** $N = 4 \cdot 10^9$.

(d) $N = 5 \cdot 10^9$. **(e)** $N = 6 \cdot 10^9$. **(f)** $N = 7 \cdot 10^9$.

(g) $N = 8 \cdot 10^9$. **(h)** $N = 9 \cdot 10^9$.

Figure 3.17: Comparisons of the head to tail betatron wave number spread.

CHAPTER 4

PWFA e^+e^- Linear Collider Parameter Study

In this chapter we will first give a brief review of beamstrahlung theory and creation of unwanted particles due to beam-beam interactions to outline the constrain on luminosity imposed by beam-beam interactions. This is followed by a beam-beam parameter study for a TeV-scale e^+e^- PWFA linear collider based on the parameter set in table 4.2, where we optimised beam parameters at the interaction point (IP) in order to maximise luminosity and limit luminosity spread introduced by beam-beam effects. In particular, we studied the luminosity spectrum using GUINEA-PIG[i] [19] simulations for very short bunches, as favoured by PWFA linear accelerators. This preference of short beams in PWFA can be exploited to reduce the beam sizes accordingly without increasing the level of beamstrahlung, while achieving a higher luminosity. Some of the findings can be found in reference [81].

4.1 Beamstrahlung theory

We will here provide a brief review of beamstrahlung theory. More details can be found in reference [82].

Colliding beams in a linear collider are focused to small transverse dimensions in order to reach high luminosity. This gives rise to intense electromagnetic fields that will bend the trajectories of particles in the opposite beam, and cause the particles to emit radiation in the form of beamstrahlung, and hence lose energy. A large fraction of particles will therefore collide with a less than nominal energy, and form a luminosity spectrum. In

[i]Generator of Unwanted Interactions for Numerical Experiment Analysis – Programme Interfaced to GEANT.

this chapter, we define peak luminosity $\mathcal{L}_{0.01}$ to be luminosity in the energy band above 99% of nominal centre of mass energy. The luminosity spectrum for CLIC is shown in figure 4.1.

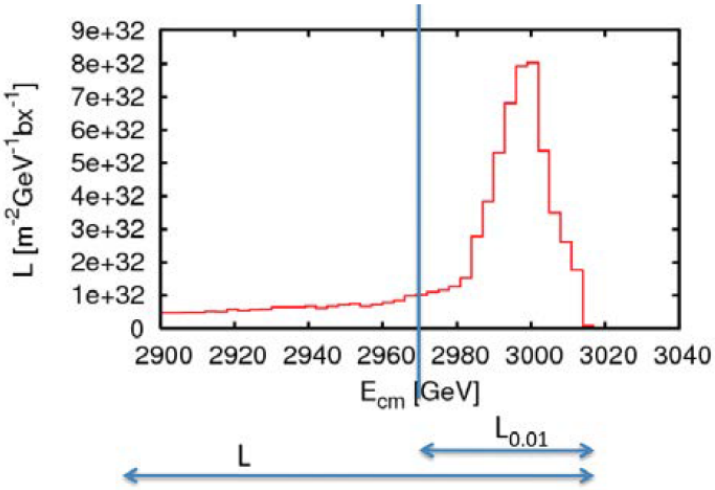

Figure 4.1: The luminosity spectrum of CLIC at 3 TeV given as integrated luminosity per energy band and beam crossing bx. Luminosity in the energy band above 99% of nominal centre of mass energy is defined as $\mathcal{L}_{0.01}$. Adapted from reference [83].

4.1.1 Beamstrahlung parameter

Beamstrahlung can be characterised by the critical energy defined at half power spectrum [19]

$$\mathscr{E}_\mathrm{c} = \hbar\omega_\mathrm{c} = \frac{3}{2}\frac{\hbar\gamma^3 c}{R}, \tag{4.1}$$

where γ is the Lorentz factor and R is the bending radius of the particle trajectory. It is however more convenient to use the dimensionless Lorentz invariant beamstrahlung parameter defined as

$$\Upsilon = \frac{e\hbar}{m_\mathrm{e}^3 c^3}(p_\mu F^{\mu\lambda} p^\nu F_{\lambda\nu})^{1/2}, \tag{4.2}$$

where p^μ is the four-momentum of the particle, and $F^{\mu\nu}$ is the electromagnetic field tensor of the beam field. The beamstrahlung parameter can also be written as

$$\Upsilon = \frac{2}{3}\frac{\hbar\omega_\mathrm{c}}{\mathscr{E}} = \gamma\frac{\langle E + cB\rangle}{B_\mathrm{c}}, \tag{4.3}$$

where $\mathscr{E}$ is the energy of a particle before emitting radiation and

$$B_\mathrm{c} = \frac{m_\mathrm{e}^2 c^2}{e\hbar} = 4.4140\,\mathrm{GT} \tag{4.4}$$

is the Schwinger critical field. Υ can be interpreted as a measure for the strength of the electromagnetic fields in the rest frame of the electron in units of B_c. Since fields above B_c are expected to cause nonlinear QED effects, $\Upsilon \ll 1$ is associated with the classical regime, while $\Upsilon \gg 1$ corresponds to the (deep) quantum regime.

Υ is not constant during collision. For Gaussian beams with N particles, rms beam length σ_z and whose horizontal and vertical beam sizes at the IP are σ_x^* and σ_y^* respectively, the average and maximum Υ can be approximated as

$$\langle\Upsilon\rangle \approx \frac{5}{6}\frac{Nr_e^2\gamma}{\alpha\sigma_z(\sigma_x^*+\sigma_y^*)} \quad \text{and} \quad \Upsilon_{\max} \approx \frac{12}{5}\langle\Upsilon\rangle, \tag{4.5}$$

where r_e is the classical electron radius and α is the fine structure constant.

4.1.2 Photon emission spectrum

The radiation equation describing photon emission for arbitrary Υ can be derived by solving the Dirac equation in a uniform magnetic field and compute the transition rates. This was first done by Sokolov-Ternov [84], and reads

$$\frac{\partial\dot{N}_\gamma}{\partial\omega} = \frac{\alpha}{\sqrt{3}\pi\gamma^2}\left[\int_q^\infty K_{5/3}(q')\,\mathrm{d}q' + \frac{\hbar\omega}{\mathscr{E}}\frac{\hbar\omega}{\mathscr{E}-\hbar\omega}K_{2/3}(q)\right], \tag{4.6}$$

where $K_{5/3}$ and $K_{2/3}$ are modified Bessel functions, and $q = \frac{\omega}{\omega_c}\frac{\mathscr{E}}{\mathscr{E}-\hbar\omega}$.

In order to obtain the expected number of emitted photons per unit time, we integrate the photon emission spectrum over the photon frequency up to $\mathscr{E}/\hbar$ to obtain

$$\frac{\mathrm{d}N_\gamma}{\mathrm{d}t} = \int_0^{\mathscr{E}/\hbar}\frac{\partial\dot{N}_\gamma}{\partial\omega}\,\mathrm{d}\omega = \frac{5}{2\sqrt{3}}\frac{\alpha^2 c\Upsilon}{r_e\gamma}U_0(\Upsilon), \tag{4.7}$$

with

$$U_0(\Upsilon) \approx \frac{1}{(1+\Upsilon^{2/3})^{1/2}}. \tag{4.8}$$

The average relative energy loss per unit time is

$$\left\langle -\frac{1}{\mathscr{E}}\frac{\mathrm{d}\mathscr{E}}{\mathrm{d}t}\right\rangle = \int_0^\infty\frac{\hbar\omega}{\mathscr{E}}\frac{\partial\dot{N}_\gamma}{\partial\omega}\,\mathrm{d}\omega = \frac{2}{3}\frac{\alpha^2 c\Upsilon^2}{r_e\gamma}U_1(\Upsilon), \tag{4.9}$$

where

$$U_1(\Upsilon) \approx \frac{1}{[1+(1.5\Upsilon)^{2/3}]^2}. \tag{4.10}$$

For Gaussian beams, the average number of emitted photons per electron during the collision can be approximated as

$$n_\gamma \approx 2.54\frac{\alpha^2\sigma_z}{r_e\gamma}\langle\Upsilon\rangle U_0(\langle\Upsilon\rangle), \tag{4.11}$$

while the relative beam particle energy loss can be approximated by

$$\delta_{\mathscr{E}} = \left\langle -\frac{\Delta\mathscr{E}}{\mathscr{E}} \right\rangle \approx 1.24\frac{\alpha^2\sigma_z}{r_e\gamma}\langle\Upsilon\rangle^2 U_1(\langle\Upsilon\rangle). \tag{4.12}$$

In order to keep $\delta_{\mathscr{E}} < 10\%$, most linear collider designs choose $\alpha^2\sigma_z\langle\Upsilon\rangle/(r_e\gamma) \sim 1$. We then also have $n_\gamma \sim 1$.

4.1.3 Beamstrahlung and luminosity

In the classical regime, $\Upsilon \ll 1$, $U_0 \approx U_1 \approx 1$, so that

$$n_\gamma \approx 2.54\frac{\alpha^2\sigma_z}{r_e\gamma}\langle\Upsilon\rangle = 2.12\frac{\alpha N r_e}{\sigma_x^* + \sigma_y^*}. \tag{4.13}$$

Since $\mathcal{L} \propto 1/(\sigma_x^*\sigma_y^*)$ and $n_\gamma \propto 1/(\sigma_x^* + \sigma_y^*)$, choosing a flat beam with $\sigma_x^* \gg \sigma_y^*$ can limit n_γ without sacrificing luminosity. This gives the following relation on σ_x^* and n_γ:

$$\sigma_x^* = 2.12\frac{\alpha r_e N}{n_\gamma}, \tag{4.14}$$

which leads to

$$\mathcal{L} = \frac{0.47 H_D}{4\pi\alpha}\frac{n_\gamma}{r_e\sigma_y^*}\frac{\eta P_{AC}}{\mathscr{E}_b}, \tag{4.15}$$

where we have used $N N_b f_r \mathscr{E}_b = \eta P_{AC}$. η is the total (wall-plug to beam) conversion efficiency, P_{AC} the wall-plug power for beam acceleration and $\mathscr{E}_b$ is the beam energy.

In the quantum regime with $\Upsilon \gg 1$, $U_0 \approx \Upsilon^{-1/3}$. This yields

$$n_\gamma \approx 2.54\frac{\alpha^2\sigma_z}{r_e\gamma}\langle\Upsilon\rangle^{2/3} = 2.25\left(\frac{\alpha^2\sqrt{r_e\sigma_z}N}{\sqrt{\gamma}(\sigma_x^* + \sigma_y^*)}\right)^{2/3}. \tag{4.16}$$

We can again use flat beams to mitigate beamstrahlung, which yields

$$\sigma_x^* = 3.38\frac{\alpha^2 N}{n_\gamma^{3/2}}\sqrt{\frac{r_e\sigma_z}{\gamma}}. \tag{4.17}$$

Inserting this into the equation for the total luminosity, we obtain

$$\boxed{\mathcal{L} = \frac{0.30 H_D}{4\pi\alpha^2}\sqrt{\frac{\gamma}{r_e\sigma_z}}\frac{n_\gamma^{3/2}}{\sigma_y^*}\frac{\eta P_{AC}}{\mathscr{E}_b}.} \tag{4.18}$$

Equation (4.17) shows that for $\Upsilon \gg 1$, a shorter beam can suppress beamstrahlung. This implies that σ_x^* can be reduced accordingly for a flat beam, as described by equation

(4.17), without increasing n_γ. Consequently, the luminosity can be increased for shorter beams, as outlined by equation (4.18). This is particularly advantageous for PWFA colliders, since short beams are preferred in PWFA due to the high plasma frequency. E.g. for a plasma with density $n_0 = 10^{16}\,\mathrm{cm}^{-3}$, the plasma wavelength is $\lambda_\mathrm{p} = 334\,\mu\mathrm{m}$. For comparison, $\lambda_\mathrm{RF} = 2.51\,\mathrm{cm}$ in CLIC.

Due to the optics of the beam delivery system (BDS), the design of the BDS of a linear collider will put a practical lower limit on β_y^*. Assuming that this practical limit can be overcome, the lower limit for β_y^* is set by the hourglass effect. If $\beta_y^* < \sigma_z$, the beam is focused to a small size, but only over a short length, which leads to a reduction in luminosity. In order to mitigate the luminosity reduction caused by the hourglass effect, one requires $\beta_y^* \geq \sigma_z$. Choosing $\beta_y^* = \sigma_z$, the luminosity for the classical regime can be written as

$$\mathcal{L} = \frac{0.47 H_\mathrm{D}}{4\pi\alpha} \frac{n_\gamma \sqrt{\gamma}}{r_\mathrm{e}\sqrt{\varepsilon_{\mathrm{N}y}\sigma_z}} \frac{\eta P_\mathrm{AC}}{\mathscr{C}_\mathrm{b}}, \tag{4.19}$$

where $\varepsilon_{\mathrm{N}y}$ is the normalised vertical emittance.

For the quantum regime, the luminosity is given by

$$\boxed{\mathcal{L} = \frac{0.30 H_\mathrm{D}}{4\pi\alpha^2} \frac{\gamma n_\gamma^{3/2}}{\sqrt{r_\mathrm{e}\varepsilon_{\mathrm{N}y}}\sigma_z} \frac{\eta P_\mathrm{AC}}{\mathscr{C}_\mathrm{b}},} \tag{4.20}$$

which still benefits short beams and is advantageous for PWFA colliders.

4.2 Background considerations

Beam-beam effects can give rise to a number of events that contribute to the background signal in the detectors that may potentially compromise the relevant measurements of the experiment. This includes the spent beams after collision and the creation of unwanted particles through beam-beam interactions.

4.2.1 Spent beam

The disruption of beam particles after collision is often described using the disruption parameter. For a flat Gaussian beam, one can define two disruption parameters in x and y as [85]

$$D_x = \frac{2N r_\mathrm{e}\sigma_z}{\gamma\sigma_x^*(\sigma_x^* + \sigma_y^*)}, \quad D_y = \frac{2N r_\mathrm{e}\sigma_z}{\gamma\sigma_y^*(\sigma_x^* + \sigma_y^*)}. \tag{4.21}$$

For $D_{x,y} \ll 1$, the beams will act as a thin lens with focal length $\sigma_z/D_{x,y}$ for a particle in the opposite beam. We can thus define a nominal disruption angle

$$\theta_\mathrm{D} = \frac{2 r_\mathrm{e} N}{\gamma(\sigma_x^* + \sigma_y^*)} = \frac{D_x\sigma_x^*}{\sigma_z} = \frac{D_y\sigma_y^*}{\sigma_z} \tag{4.22}$$

that characterises the disruption angle of a beam.

4.2.2 Coherent pairs

A photon can fluctuate into a virtual e^+e^- pair, and in a strong electromagnetic field, these virtual particles can be set onto their mass shells and thus become real. This process can be contributed both by the real beamstrahlung photons or by the virtual photons co-moving with the high-energy beam particles. For coherent pair creation sourced by beamstrahlung, the average number of e^+e^- pairs created per beam particle after collision can be calculated by folding the photon emission spectrum given in equation (4.6) with the probability of the photons to turn into pairs. The result is [86]

$$n^{\mathrm{r}}_{\mathrm{e^+e^-}} = \frac{4\sqrt{3}}{25\pi}\left(\frac{\alpha\sigma_z}{\lambda\!\!\!^{-}_{\mathrm{e}}\gamma}\Upsilon\right)^2 \Xi(\Upsilon), \tag{4.23}$$

where

$$\Xi(\Upsilon) = \frac{1}{2\Upsilon^2}\int_0^1 \left[\int_q^\infty K_{5/3}(q')\,\mathrm{d}q' + \frac{\hbar\omega}{\mathscr{E}}\frac{\hbar\omega}{\mathscr{E}-\hbar\omega}K_{2/3}(q)\right] K^2_{1/3}\left(\frac{4}{3y\Upsilon}\right)\frac{\mathrm{d}y}{y} \tag{4.24}$$

$$= \begin{cases} 0.5\exp(-16/(3\Upsilon)), & \Upsilon \ll 1 \\ 2.6\Upsilon^{-2/3}\ln\Upsilon, & \Upsilon \gg 1, \end{cases} \tag{4.25}$$

$y = \hbar\omega/\mathscr{E}$ and $\lambda\!\!\!^{-}_{\mathrm{e}}$ is the reduced electron Compton wavelength.

Contribution from virtual photons becomes significant for $\Upsilon \gg 1$. This process is often termed trident cascade, and the average number of coherent pairs created per primary particle is given by

$$n^{\mathrm{v}}_{\mathrm{e^+e^-}} = \frac{4\sqrt{3}}{25\pi}\left(\frac{\alpha\sigma_z}{\lambda\!\!\!^{-}_{\mathrm{e}}\gamma}\Upsilon\right)\Omega(\Upsilon) \tag{4.26}$$

$$\Omega(\Upsilon) \approx 2.6\alpha\ln\Upsilon, \quad \Upsilon \gg 1. \tag{4.27}$$

Coherent pairs are generally created with significantly lower energies than the beam particles, and will thus be deflected more severely than the high-energy primary particles. This can therefore potentially cause significant event reconstruction problems for high-energy physics experiments.

4.2.3 Incoherent pairs

In addition to coherent pairs, e^+e^- pairs can also be created through incoherent pair creation, which are caused by the interactions of real beamstrahlung photons, virtual photons accompanying an electron or positron or a combination of these. There are three incoherent processes [87]:

1. In the Breit-Wheeler process $\gamma\gamma \to e^+e^-$, two real beamstrahlung photons interact to produce an incoherent pair. The total cross section is given by [88]

$$\sigma_{\mathrm{BW}} = \frac{4\pi\hbar^2c^2\alpha^2}{s}\left[\left(1+\frac{4m_e^2c^4}{s}-\frac{8m_e^4c^8}{s^2}\right)\ln\frac{1+\beta}{1-\beta}-\left(1+\frac{4m_e^2c^4}{s}\right)\beta\right], \quad (4.28)$$

where $\beta = \sqrt{1-4m_e^2c^4/s}$.

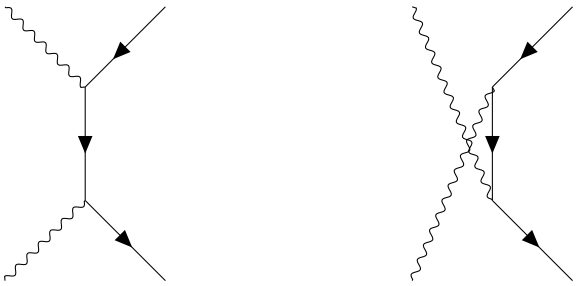

Figure 4.2: Breit-Wheeler process.

2. In the Bethe-Heitler process $e^\pm\gamma \to e^\pm e^+e^-$, a real photons interacts with a virtual photon to produce an incoherent pair. The total cross section can be approximated by [88]

$$\sigma_{\mathrm{BH}} \approx \frac{28\alpha r_e^2}{9}\left(\ln\frac{s}{m_e^2c^4}-\frac{109}{42}\right). \quad (4.29)$$

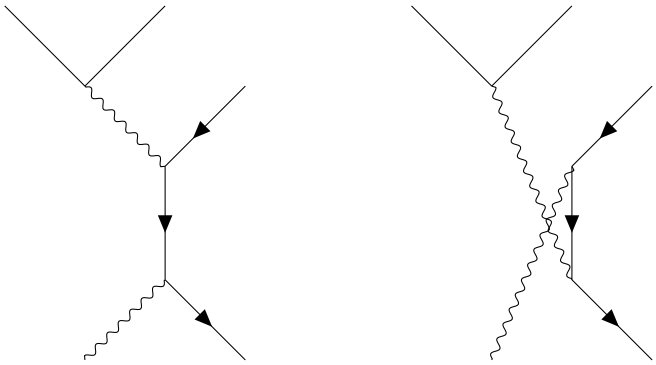

Figure 4.3: Bethe-Heitler process.

3. In the Landau-Lifshitz process $e^\pm e^\pm \to e^\pm e^\pm e^+e^-$, an e^+e^- pair is created by the interaction of two virtual photons. The total cross section can be found in reference [88]:

$$\sigma_{\mathrm{LL}} \approx \frac{\alpha^2 r_e^2}{\pi}\left(1.04\ln^3\frac{s}{m_e^2c^4}-6.59\ln^2\frac{s}{m_e^2c^4}-11.8\ln\frac{s}{m_e^2c^4}+104\right). \quad (4.30)$$

Most incoherent pairs have low energies and small angles, but some are created with large angles. Like coherent pairs, incoherent pairs deflected by the beam fields may cause significant background problems. This can be mitigated by using a solenoid field inside the detector to confine the unwanted particles.

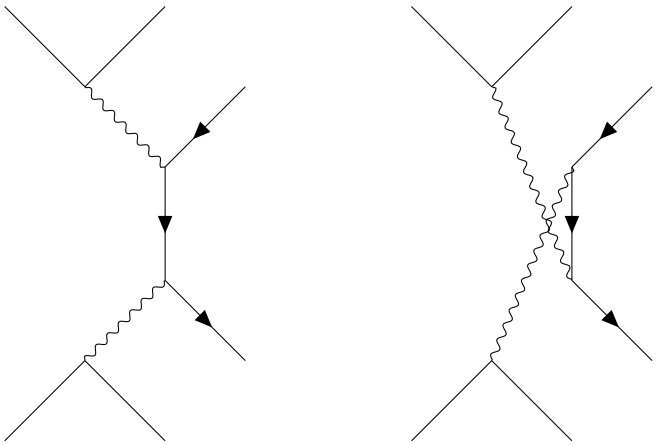

Figure 4.4: Landau-Lifshitz process.

4.2.4 Hadronic events

In addition to fluctuating into a virtual electron-positron pair, a photon can also fluctuate into a quark-antiquark pair. At energy scales of about 1 GeV, the virtual $q\bar{q}$ pair has sufficient time to evolve into a complicated hadronic state that cannot be described by using only perturbation theory [89]. This may occur in a direct scattering $\gamma\gamma \to q\bar{q}$ between two photons, which may put the $q\bar{q}$ pair on their mass shell. The majority of the secondary particles produced in such events have small transverse momenta and angles, but a small number of jets termed minijets have a large transverse momentum, which may impact the detector and provide an additional background complicating the re-construction of interesting events.

Moreover, the hadronic structure of the photons, which can be described as "internal" quark and gluon densities of the photon, can also undergo scattering. The scattering of these partons give rise to two additional processes that contribute to the hadronic background, see figure 4.5. In the once-resolved process, only one of the photons scatters via its partons, which produces an additional hadronic jet from the remnant part of the photon. In the twice-resolved process, the partons in both the photons undergo scattering, and produce two additional jets. These additional jets travel along the beam axis and are commonly named spectator jets.

4.2.5 Background mitigation using a solenoid field

If left unmitigated, particles with angles larger than the opening angle of the vertex detector will hit the detector. One of the simplest ways for reducing the number of hits is to introduce a solenoid field B_s inside the detector to trap the charged particles. A particle with transverse momentum $p_\perp$ will then travel along a helix with radius

$$r = \frac{p_\perp}{eB_s}. \tag{4.31}$$

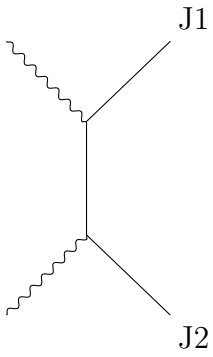

(a) Direct scattering.

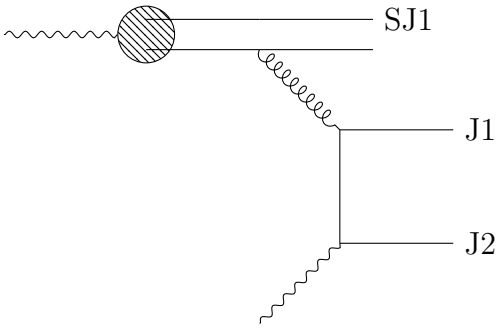

(b) Once-resolved scattering.

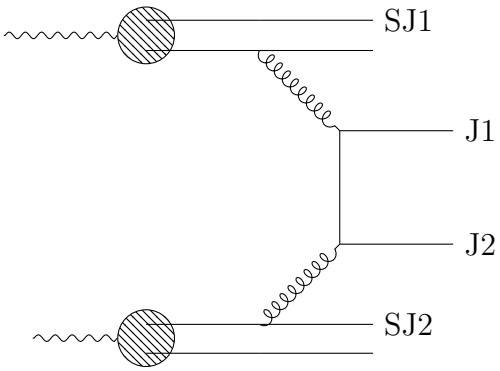

(c) Twice-resolved scattering.

Figure 4.5: Scattering processes resulting in minijets J and spectator jets SJ.

The particle's distance to the beam axis as a function of the longitudinal distance z to the IP is then given by [19]

$$a(z) = r\sqrt{2(1-\cos\varphi(z))} \tag{4.32}$$

$$\varphi(z) = \frac{z}{r}\tan\theta, \tag{4.33}$$

where θ is the particle's polar angle.

Let ℓ be the half length of the inner cylindrical part of the vertex detector, which is fixed by the vertex detector's opening angle θ_0 and inner radius R through $\ell = R/\tan\theta_0$. Particles that perform more than half a helix motion during the detector half length ℓ, i.e. particles with $\varphi(\ell) > \pi$, are trapped and cannot hit the detector if $2r < R$, where r is the helix radius of the particles, and R is the detector inner radius. Particles that undergo less than half a helix period during ℓ, will travel along a bent trajectory, where the helix motion has effectively reduced the particles' original polar angle θ, and may thus further reduce the number of hits depending on the particles' θ and $p_\perp$.

The detector parameters used for background considerations are summarised in table 4.1.

Parameter	Symbol	Value
Inner Radius	R	1.0 cm
Total angular coverage	$\lvert\cos\theta_0\rvert$	0.99
Distance from IP to exit	L	3.0 m
Solenoid field	B_s	4.0 T

Table 4.1: Detector parameters.

4.3 Luminosity optimisation results for equal e^+e^- beam charges

We performed beam-beam simulations using GUINEA-PIG, where we optimised collisions of e^+e^- beams with respect to luminosity spread by performing parameter scans over β_x^*, β_y^* and short σ_z's, as favoured by PWFA linear accelerators. In this study, we assumed that both the e^+ and the e^- beams have $N = 5 \cdot 10^9$ particles, as derived in chapter 3, and that β_y^* can be made arbitrarily small.

Results on luminosity optimised with respect to luminosity spread are presented followed by results on background study.

4.3.1 Luminosity optimisation results

We define the peak luminosity $\mathcal{L}_{0.01}$ as the part of the luminosity corresponding to centre of mass energy $\sqrt{s} > 0.99\sqrt{s_0}$, where $\sqrt{s_0}$ is the nominal centre of mass collision energy. The acceptable level of luminosity spread is chosen to be $\mathcal{L}_{0.01}/\mathcal{L} \approx 1/3$, where $\mathcal{L}$ is the total luminosity. Contour plots of the ratio of peak luminosity to total luminosity are plotted in the β_x^*–β_y^* plane for several σ_z in figure 4.6.

Both beams have $N = 5 \cdot 10^9$ particles, as derived in the PWFA parameter study in chapter 3, and were collided at $\sqrt{s_0} = 3\,\mathrm{TeV}$. For a given pair of β_y^* and σ_z, we used the result in figure 4.6 to find an optimal β_x^* that yields $\mathcal{L}_{0.01}/\mathcal{L} \approx 1/3$. This process was repeated for each pair of β_y^* and σ_z, where we only kept the results given by an optimal β_x^* that corresponds to the defined luminosity spread tolerance. The corresponding results for $\mathcal{L}$ and $\mathcal{L}_{0.01}$ are shown in figure 4.7 and 4.8, respectively. The unit bx^{-1} denotes "per beam crossing".

Assuming σ_x can be made sufficiently small to keep n_γ constant as σ_z is reduced, and that σ_y is kept constant, equation (4.18) gives the scaling $\mathcal{L} \propto 1/\sqrt{\sigma_z}$. The luminosity is plotted against σ_z for a selection of β_y^* along with the corresponding $\mathcal{L} \propto 1/\sqrt{\sigma_z}$ fits in figure 4.9.

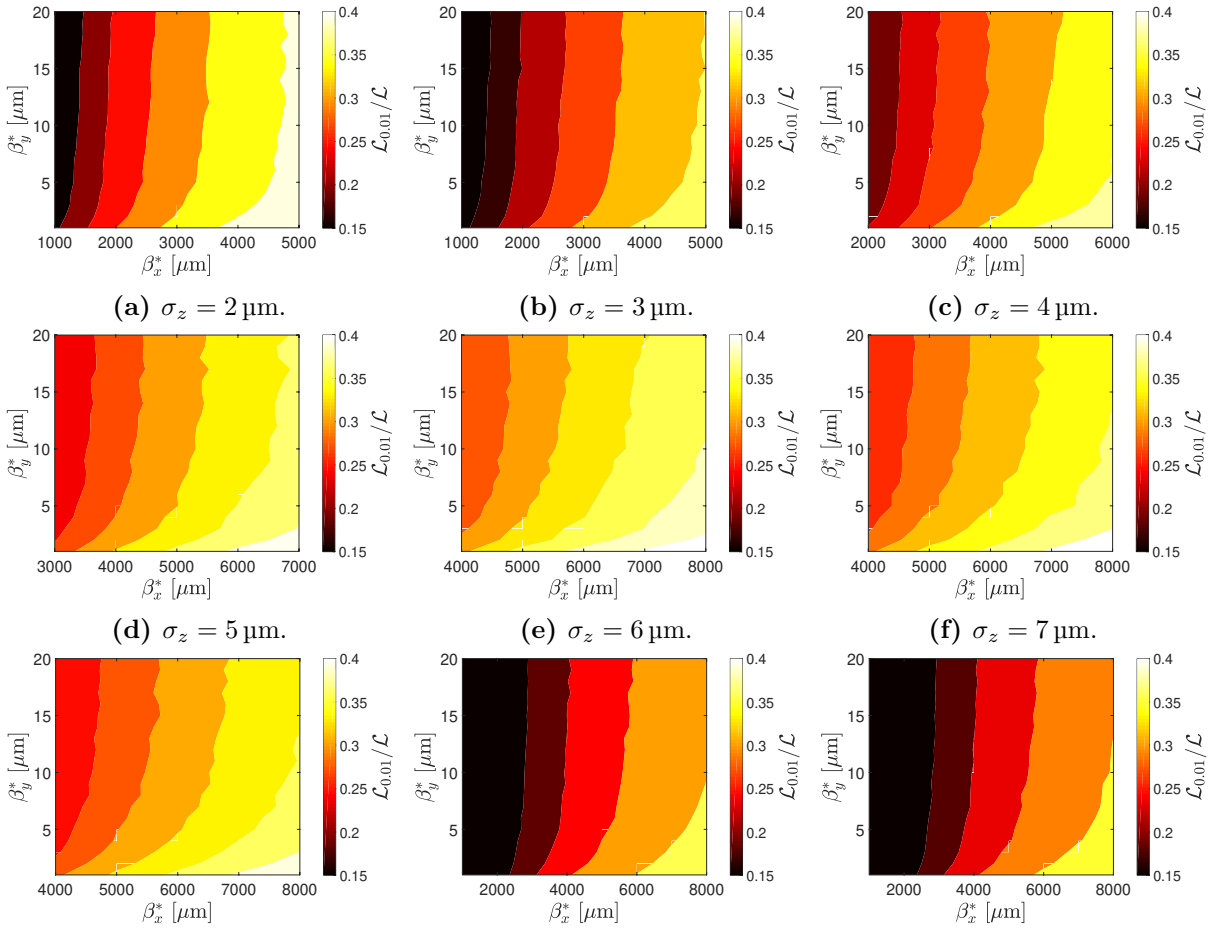

(a) $\sigma_z = 2\,\mu\text{m}$. **(b)** $\sigma_z = 3\,\mu\text{m}$. **(c)** $\sigma_z = 4\,\mu\text{m}$.

(d) $\sigma_z = 5\,\mu\text{m}$. **(e)** $\sigma_z = 6\,\mu\text{m}$. **(f)** $\sigma_z = 7\,\mu\text{m}$.

(g) $\sigma_z = 8\,\mu\text{m}$. **(h)** $\sigma_z = 9\,\mu\text{m}$. **(i)** $\sigma_z = 10\,\mu\text{m}$.

Figure 4.6: An overview of the ratio of peak luminosity to total luminosity for different combinations of rms beam length σ_z, horizontal beta function β_x^* and vertical beta function β_y^*.

The $1/\sqrt{\sigma_z}$-scaling agree very well with simulation results, especially for larger values of β_y^*. The disagreement at small β_y^* may be due to the hourglass effect, which imposes $\beta_y^* \geq \sigma_z$. When $\beta_y^* < \sigma_z$, a small beam size is only maintained over a small length, which reduces luminosity. Thus, using our range of σ_z-values, the luminosity appears to decrease faster than the $1/\sqrt{\sigma_z}$-scaling.

In chapter 3 we found a parameter set for the main beam with acceptable stability, energy spread and efficiency. We now consider beams with $N = 5 \cdot 10^9$ particles and a rms beam length of $\sigma_z = 5\,\mu\text{m}$ (table 3.3). The corresponding optimised results for a $N = 5 \cdot 10^9$ $\sigma_z = 5\,\mu\text{m}$ beam from this study are summarised in table 4.2 together with relevant results from chapter 3.

In deriving this parameter set, we did not consider optics constraints on the vertical beta function. The vertical beta function from the 3 TeV CLIC parameter set [27] represents what is currently achievable, which is about one order of magnitude larger than our

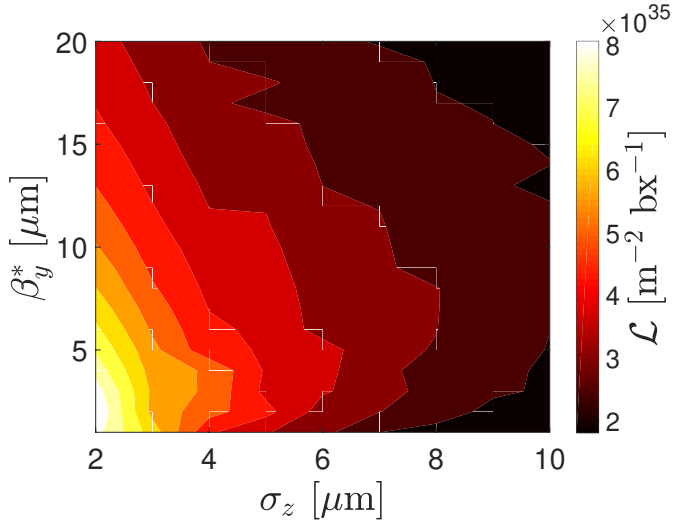

Figure 4.7: Contour plot of total luminosity $\mathcal{L}$ vs. beam length σ_z and vertical beta function β_y^*, where the horizontal β_x^* for each pair of σ_z and β_y^* has been chosen such that $\mathcal{L}_{0.01}/\mathcal{L} \approx 1/3$.

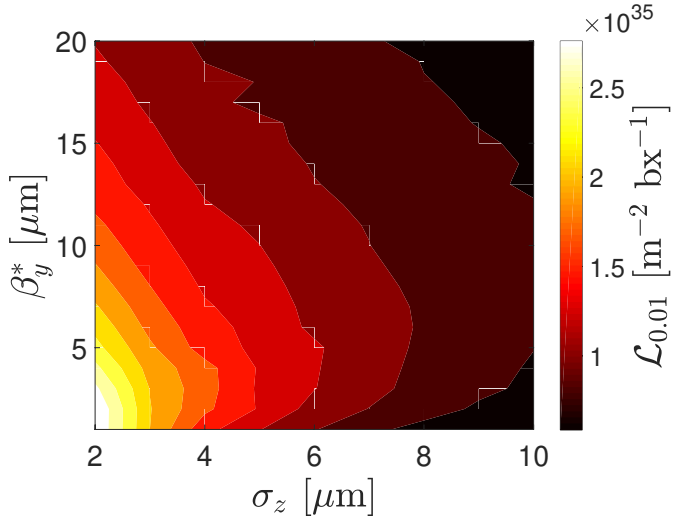

Figure 4.8: Contour plot of peak luminosity $\mathcal{L}_{0.01}$ vs. beam length σ_z and vertical beta function β_y^*, where the horizontal beta function β_x^* for each pair of σ_z and β_y^* has been chosen such that $\mathcal{L}_{0.01}/\mathcal{L} \approx 1/3$.

proposed values.

4.3.2 Background

In this background study, we will compare the GUINEA-PIG results for the derived parameter set against the background calculated using CLIC parameters. Note that in this thesis the calculations in GUINEA-PIG were done with $\beta_{x,y}^*$ that do not take non-linear effects into account and thus differ from the values given in reference [27]. When referring to 3 TeV CLIC parameters in this thesis, we use $\beta_x^* = 9.0\,\text{mm}$ and $\beta_y^* = 0.147\,\text{mm}$, which are matched to the spot sizes and emittances given in reference [27] at 3 TeV.

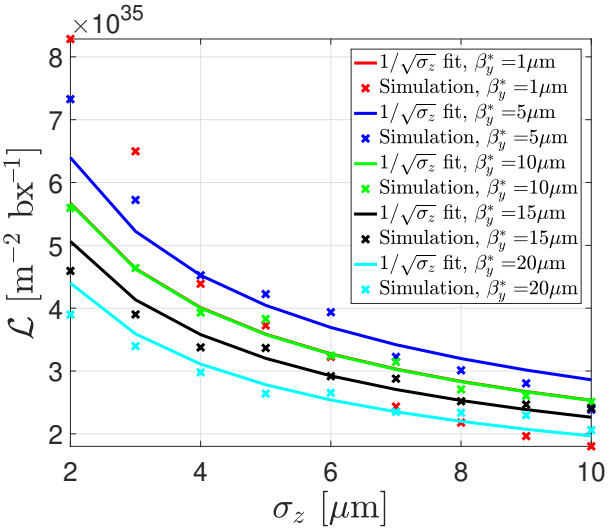

Figure 4.9: Total luminosity $\mathcal{L}$ vs. rms beam length σ_z for several vertical beta functions β_y^* along with corresponding theoretical $1/\sqrt{\sigma_z}$ fits. The red solid line is covered by the green solid line.

Parameter	**Symbol**	**Unit**	**Value**
Plasma density	n_0	$10^{16}\,\mathrm{cm}^{-3}$	2.0
Particle number	N	10^9	5
rms beam length	σ_z	µm	5
Horizontal beta function at IP	β_x^*	mm	5
Vertical beta function at IP	β_y^*	µm	5
Normalised horizontal emittance	$\gamma\varepsilon_x$	mm mrad	0.887
Normalised vertical emittance	$\gamma\varepsilon_y$	mm mrad	0.02
Relative rms energy spread	$\sigma_{\mathscr{E}}/\langle\mathscr{E}\rangle$	%	1.1
Normalised amplification factor	Λ/Λ_0		6.2
Drive beam to main beam efficiency	η	%	37.5
Beam power/beam	$P_\mathrm{b}/(f_\mathrm{r}N_\mathrm{b})$	kWs	1.2
Beamstrahlung photons/e^-	n_γ		2.3
Total luminosity/beam crossing	$\mathcal{L}$	$10^{35}\,\mathrm{m}^{-2}\,\mathrm{bx}^{-1}$	4.3
Peak 1% luminosity/beam crossing	$\mathcal{L}_{0.01}$	$10^{35}\,\mathrm{m}^{-2}\,\mathrm{bx}^{-1}$	1.4

Table 4.2: Parameters for a 3 TeV PWFA linear e^+e^- collider.

Contour plots of the polar angle-energy distribution for the spent beams are shown in figure 4.10. The spent beams in derived parameter set are expected to be more deflected due to a larger N and smaller $\sigma_{x,y}^*$ compared to the CLIC beams. Furthermore, we find very good agreement with the nominal disruption angle predicted by the equation (4.22) for both parameter sets.

The total number of coherent, trident and incoherent e^+e^- pairs produced per beam

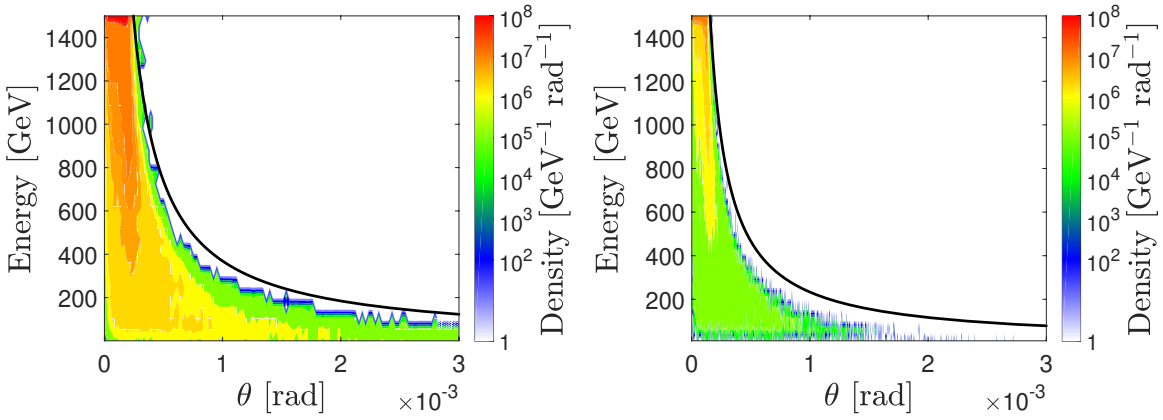

(a) Derived parameter set. **(b)** CLIC parameter set.

Figure 4.10: Polar angle-energy distribution of a spent beam for the derived parameter set given in table 4.2 and the CLIC parameter set. Black solid lines show the nominal disruption angle predicted by equation (4.22).

crossing are listed in table 4.3 along with the number of hadronic events per beam crossing with a centre of mass energy above 5 GeV. These are denoted N_{coh}, N_{tri}, N_{inc} and N_{H}, respectively. The total energies for these background particles are also listed. More background particles are produced with the derived parameter set compared to the CLIC parameter set, which is expected due to the larger beam particle density and more intense fields associated with the derived parameter set.

Parameter	Unit	Derived parameter set	CLIC parameter set
N_{coh}	10^8	41.45	7.33
$\mathscr{E}_{\text{coh}}$	10^{11} GeV	7.36	2.24
N_{tri}	10^7	21.62	0.68
$\mathscr{E}_{\text{tri}}$	10^9 GeV	12.08	1.29
N_{inc}	10^5	19.29	3.68
$\mathscr{E}_{\text{inc}}$	10^7 GeV	16.08	2.76
N_{H}		20.23	3.65

Table 4.3: Number of background particles and total energies per beam crossing.

The θ–$p_\perp$ distribution for various background particle types are shown in figure 4.11 and 4.12 for the derived and CLIC parameter sets, respectively. In both cases, there are a significant amount of incoherent pairs distributed at $\theta > 0.1$ rad. Using the detector parameters in table 4.1, we found that only coherent and incoherent pair particles will reach the vertex detector. 50000 coherent and 205818 incoherent particles reached the vertex detector in the PWFA collider, while only 10121 incoherent particles reached the detector for the CLIC parameter set.

Depending on the size of the detector exit aperture, some background particles will not

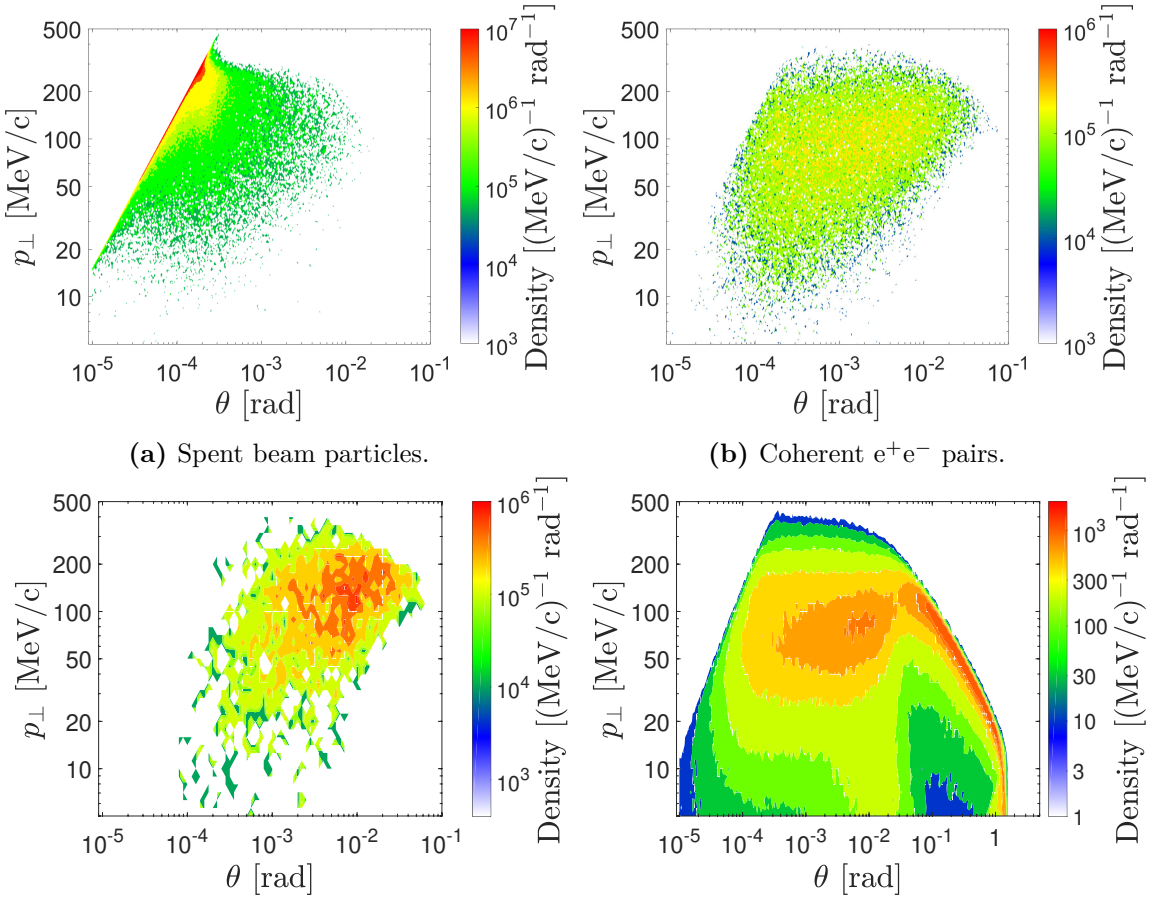

(a) Spent beam particles.

(b) Coherent e^+e^- pairs.

(c) Trident e^+e^- pairs.

(d) Incoherent e^+e^- pairs.

Figure 4.11: Polar angle-transverse momentum distribution of various particle types for the derived parameter set given in table 4.2. Note that different colour scales have been used.

pass through the opening and deposit their energy at the walls. The integrated energy deposited at the detector exit (located at $L = 3\,\text{m}$ downstream of the IP) for background particles (spent beam particles, coherent pairs and trident pairs) associated with the two colliding beams and energy deposited by the incoherent pairs are plotted as a function of detector opening radius in figure 4.13 for the two parameter sets.

Due to the stronger background associated with the derived parameter set, larger exit apertures are required to avoid the background particles compared to the background of the CLIC parameter set. In order to avoid all the spent beam particles, coherent pairs and trident pairs, a minimum opening radius of $\sim 180\,\text{mm}$ is required, while an even larger $\sim 210\,\text{mm}$ opening radius is required to avoid all the incoherent pairs for the derived parameter set. For the CLIC parameter set, minimum opening radii of $\sim 20\,\text{mm}$ and $\sim 70\,\text{mm}$ are required depending on the particle type.

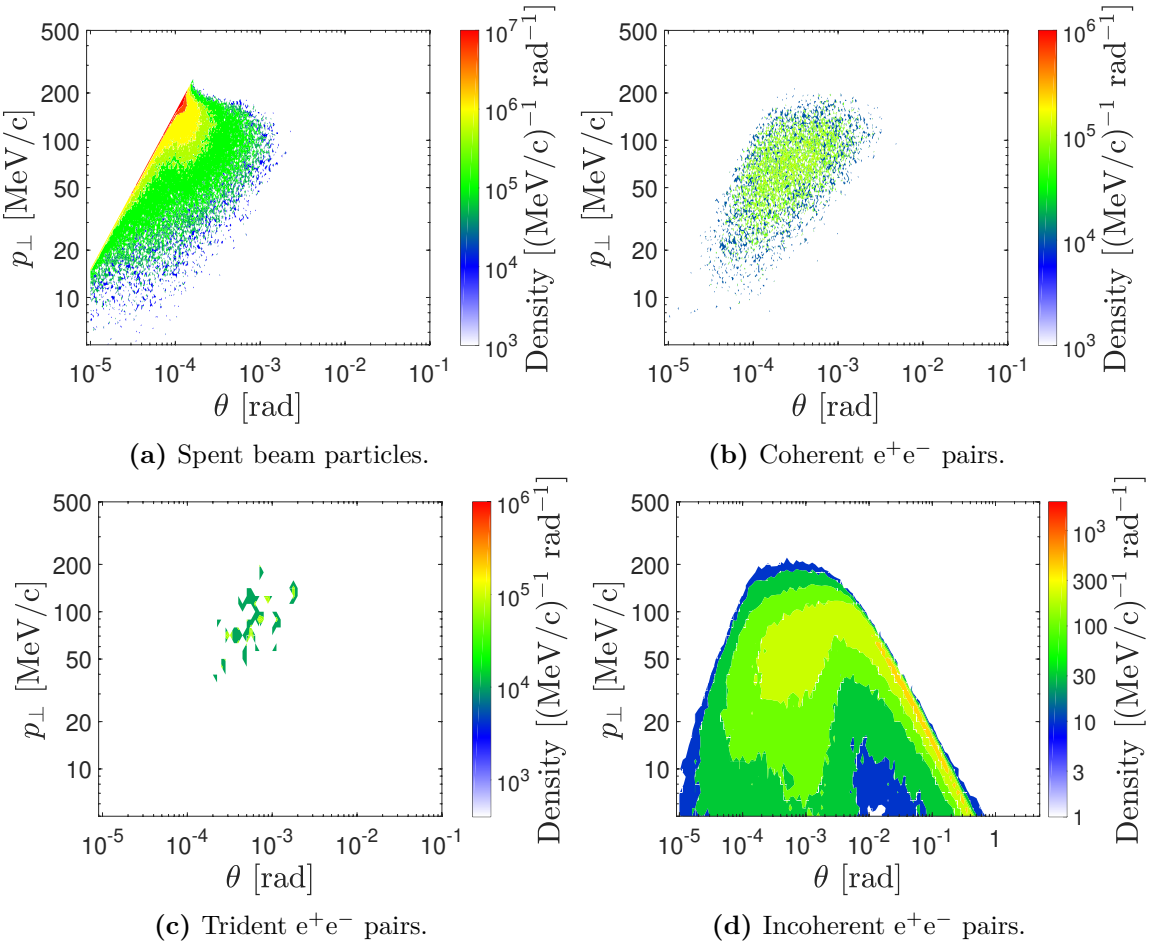

(a) Spent beam particles.

(b) Coherent e^+e^- pairs.

(c) Trident e^+e^- pairs.

(d) Incoherent e^+e^- pairs.

Figure 4.12: Transverse momentum-angle distribution of various particle types for CLIC parameters. Note that different colour scales have been used.

4.4 Impact of reduced positron beam charge

4.4.1 Luminosity performance at 3 and 14 TeV

In the blow-out regime of PWFA, an electron beam will be focused by the positive ion background, while a positron beam will be defocused. Different approaches such as hollow channel plasma [49] and the quasi-linear [90] regime have been studied, but positron acceleration remains one of the main challenges in PWFA, as there are currently no self-consistent scheme for positron acceleration in plasma that can simultaneously provide high efficiency, low preserved emittance and mitigation of transverse instabilities.

We therefore consider scenarios in which fewer positrons than electrons are accelerated, and examine the effects of asymmetric e^+e^- collisions on luminosity at two energy levels, where the number of particles N_{e^+} in the e^+ beam is only a fraction of the number of particles N_{e^-} in the e^- beam. Other beam parameters such as σ_z, $\beta^*_{x,y}$ and $\varepsilon_{Nx,y}$ are identical for the e^+e^- beams, and can be found in table 4.2. The results for three scenarios

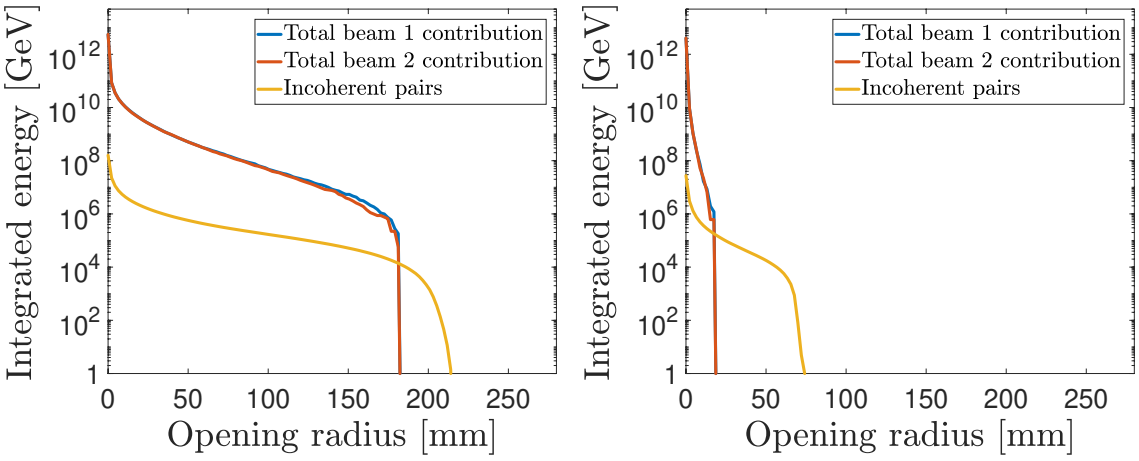

(a) Derived parameter set. **(b)** CLIC parameter set.

Figure 4.13: Integrated energy deposited at the detector exit for spent beam particles, coherent pairs and trident pairs associated with the two colliding beams in addition to energy deposited by the incoherent pairs vs. detector opening radius. The detector exit is located at $L = 3\,\mathrm{m}$ downstream of the IP.

are summarised in table 4.4 together with CLIC parameters [27].

Parameter	**Unit**	$N_{e^+} = N_{e^-}$	$N_{e^+} = 0.5N_{e^-}$	$N_{e^+} = 0.1N_{e^-}$	CLIC
N	10^9	5/5	2.5/5	0.5/5	3.72/3.72
$P_b/(f_r N_b)$	kWs	1.2	1.2	1.2	0.89
$\mathscr{E}_b$	TeV	1.5	1.5	1.5	1.5
$\mathcal{L}$	$10^{35}\,\mathrm{m}^{-2}\,\mathrm{bx}^{-1}$	4.26	1.89	0.32	0.38
$\mathcal{L}_{0.01}$	$10^{35}\,\mathrm{m}^{-2}\,\mathrm{bx}^{-1}$	1.41	0.80	0.17	0.13

Table 4.4: Parameter comparison at 3 TeV collision energy.

As a result of the reduced N_{e^+}, the total luminosity is reduced by approximately the same factor compared to cases where $N_{e^+} = N_{e^-}$. However, by reducing N_{e^+}, the beamstrahlung from the electron beam is also reduced, which results in a narrower luminosity spectrum. Alternatively, this can also be exploited to further reduce the horizontal beam size without increasing n_γ.

Even in the $N_{e^+} = 0.1N_{e^-}$ scenario, a PWFA linear collider using the parameter set in table 4.2 can still provide a comparable luminosity level per beam crossing compared to CLIC. Furthermore, the $N_{e^+} = 0.1N_{e^-}$ scenario shown in table 4.4 has a luminosity spread that is significantly better than our defined tolerance of $\mathcal{L}/\mathcal{L}_{0.01} \approx 1/3$, which indicates that the horizontal beam size can likely be reduced even further to increase the total luminosity.

The muon collider submission to the European Particle Physics Strategy [91] demon-

strated that a 14 TeV muon collider can provide a similar effective discovery potential as the 100 TeV FCC. For comparison, the same parameters for 14 TeV collision energy are shown in table 4.5. At 14 TeV, a common luminosity goal for linear colliders is $40 \cdot 10^{34}\,\mathrm{cm}^{-2}\,\mathrm{s}^{-1}$, which corresponds to $f_\mathrm{r} N_\mathrm{b} = 1.7 \cdot 10^3\,\mathrm{s}^{-1}$, $4 \cdot 10^3\,\mathrm{s}^{-1}$ and $25 \cdot 10^3\,\mathrm{s}^{-1}$ for the $N_{e^+} = N_{e^-}$, $N_{e^+} = 0.5N_{e^-}$ and $N_{e^+} = 0.1N_{e^-}$ cases, respectively. This implies that in order to achieve the target luminosity of $40 \cdot 10^{34}\,\mathrm{cm}^{-2}\,\mathrm{s}^{-1}$, total beam powers of 20 MW, 449 MW and 281 MW are required for the $N_{e^+} = N_{e^-}$, $N_{e^+} = 0.5N_{e^-}$ and $N_{e^+} = 0.1N_{e^-}$ scenarios, respectively. For comparison, the CLIC parameter set requires a total beam power of 90 MW to achieve this luminosity. However, note that none of the parameter sets in table 4.5 have been optimised for 14 TeV, which can be seen in the large luminosity spread. Furthermore, we also made the optimistic assumption that the same emittance levels and beta functions can be maintained for the two energy levels.

Parameter	**Unit**	$N_{e^+} = N_{e^-}$	$N_{e^+} = 0.5N_{e^-}$	$N_{e^+} = 0.1N_{e^-}$	CLIC
N	10^9	5/5	2.5/5	0.5/5	3.72/3.72
$P_\mathrm{b}/(f_\mathrm{r} N_\mathrm{b})$	kWs	5.61	5.61	5.61	4.17
$\mathscr{E}_\mathrm{b}$	TeV	7.0	7.0	7.0	7.0
$\mathcal{L}$	$10^{35}\,\mathrm{m}^{-2}\,\mathrm{bx}^{-1}$	23.49	9.95	1.58	3.71
$\mathcal{L}_{0.01}$	$10^{35}\,\mathrm{m}^{-2}\,\mathrm{bx}^{-1}$	5.99	3.44	0.77	0.57

Table 4.5: Parameter comparison at 14 TeV collision energy.

4.4.2 Background

Key figures for the background of the $N_{e^+} = 0.5N_{e^-}$ and $N_{e^+} = 0.1N_{e^-}$ cases at 3 TeV are summarised in table 4.6. The number 1 in the subscripts indicates that the background particles originated from the electron beam, while 2 indicates that the particles originated from the positron beam. The difference in number of beam particles creates an asymmetric background, where the background of the positron beam dominates. This asymmetry is likely linked to the stronger fields of the electron beam, which has a larger probability of converting photons from the positron beam into coherent and trident e^+e^- pairs.

Only the incoherent pairs are able to reach the detector. For the 3 TeV $N_{e^+} = 0.5N_{e^-}$ case, there are 82425 hits on the vertex detector, and 9391 hits for the 3 TeV $N_{e^+} = 0.1N_{e^-}$ case.

When the number of primary positrons are reduced, the number of background particles are also reduced. However, as the electron beam effectively acts as a lens with a smaller focal length compared to the reduced positron beams, the particles from the positron beam are deflected at larger angles, and this deflection becomes more asymmetric with decreasing N_{e^+}/N_{e^-} ratio. This is demonstrated in figure 4.13 and 4.14 for the 3 TeV cases, where the integrated energy deposited at the detector exits for the electron beam (beam 1) background is significantly more concentrated at small opening radius for small

Parameter	**Unit**	$N_{e+} = 0.5N_{e-}$	$N_{e+} = 0.1N_{e-}$
N_{coh1}	10^8	5.86	0.20
N_{coh2}	10^8	9.27	1.60
$\mathscr{E}_{coh1}$	10^{11} GeV	1.40	0.07
$\mathscr{E}_{coh2}$	10^{11} GeV	1.72	0.30
N_{tri1}	10^7	3.88	0.18
N_{tri2}	10^7	5.04	0.88
$\mathscr{E}_{tri1}$	10^9 GeV	3.36	0.40
$\mathscr{E}_{tri2}$	10^9 GeV	3.00	0.56
N_{inc}	10^5	8.00	1.16
$\mathscr{E}_{inc}$	10^7 GeV	6.80	0.88
N_H		7.47	0.85

Table 4.6: Background comparison at 3 TeV collision energy.

N_{e+}/N_{e-}. When N_{e-} is fixed, the deflection for the positron beam (beam 2) background particles remain unchanged, which allows these particles to reach a maximum exit radius of ~ 200 mm for the $N_{e+} = N_{e-}$, $N_{e+} = 0.5N_{e-}$ and $N_{e+} = 0.1N_{e-}$ cases.

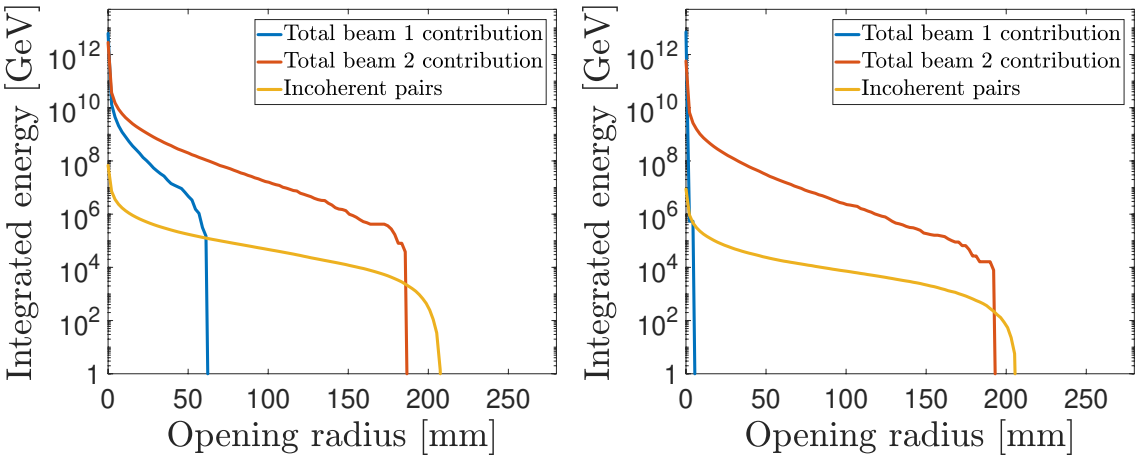

(a) The $N_{e+} = 0.5N_{e-}$ case. **(b)** The $N_{e+} = 0.1N_{e-}$ case.

Figure 4.14: Integrated energy deposited at the detector exit for spent beam particles, coherent pairs and trident pairs associated with the two colliding beams in addition to energy deposited by the incoherent pairs vs. detector opening radius. The detector exit is located 3 m downstream of the IP. $\sqrt{s} = 3$ TeV.

The same patterns are also found in the 14 TeV cases, which are evident from table 4.7 and figure 4.15. As in the 3 TeV cases, the positron beams with reduced beam charges produce a higher amount of coherent and trident pairs than the electron beams that are deflected significantly more than the background particles from the electron beams.

Comparing the 14 TeV cases to their 3 TeV counterparts, the total number of secondary

Parameter	**Unit**	$N_{e^+} = N_{e^-}$	$N_{e^+} = 0.5N_{e^-}$	$N_{e^+} = 0.1N_{e^-}$	CLIC
N_{coh1}	10^8	66.48	18.91	1.24	42.60
N_{coh2}	10^8	66.50	25.99	4.26	43.05
$\mathscr{E}_{coh1}$	10^{11} GeV	26.22	11.51	1.29	27.86
$\mathscr{E}_{coh2}$	10^{11} GeV	26.35	11.37	2.02	27.91
N_{tri1}	10^7	73.59	30.49	3.23	10.51
N_{tri2}	10^7	73.64	30.56	5.41	10.83
$\mathscr{E}_{tri1}$	10^9 GeV	49.80	36.45	10.70	24.45
$\mathscr{E}_{tri2}$	10^9 GeV	49.88	24.67	4.63	24.36
N_{inc}	10^5	92.52	37.81	5.49	22.12
$\mathscr{E}_{inc}$	10^7 GeV	322.47	143.46	19.17	64.15
N_H		175.84	62.10	7.07	44.63

Table 4.7: Background comparison at 14 TeV collision energy.

pairs, their total energies and the number of hadronic events are also about one order of magnitude higher compared to the same cases at 3 TeV. This leads to a larger number of hits in the vertex detector, which is summarised for all the eight scenarios in table 4.8. At 3 TeV, the PWFA parameter sets can lead to the total number of hits in the vertex detector being more than 10 times larger than the CLIC parameter set. This difference is even more significant at 14 TeV, where the $N_{e^+} = N_{e^-}$ case has more than a hundred times more hits than the CLIC case.

Parameter set	**Unit**	**Beam**	**Coh.**	**Tri.**	**Incoh.**
3 TeV					
$N_{e^+} = N_{e^-}$	10^4	0	5.0	0	20.6
$N_{e^+} = 0.5N_{e^-}$	10^4	0	0	0	8.2
$N_{e^+} = 0.1N_{e^-}$	10^4	0	0	0	0.9
CLIC	10^4	0	0	0	1.0
14 TeV					
$N_{e^+} = N_{e^-}$	10^4	0	1165.0	200.0	90.0
$N_{e^+} = 0.5N_{e^-}$	10^4	0	55.0	15.0	35.0
$N_{e^+} = 0.1N_{e^-}$	10^4	0	4.5	2.5	4.2
CLIC	10^4	0	3.7	0	5.9

Table 4.8: Total number of hits in the vertex detector from the spent beam (Beam), coherent pairs (Coh.), trident pairs (Tri.) and incoherent pairs (Incoh.) for the eight scenarios.

Overall, even though the derived PWFA parameter sets offer interesting improvements over the CLIC parameter set in terms of luminosity and beam power requirements, the PWFA parameter sets also lead to stronger backgrounds than the CLIC parameters both in terms of the total number of background particles and particle deflection. The deflection may result in more hits in the vertex detector, and also affect the requirement

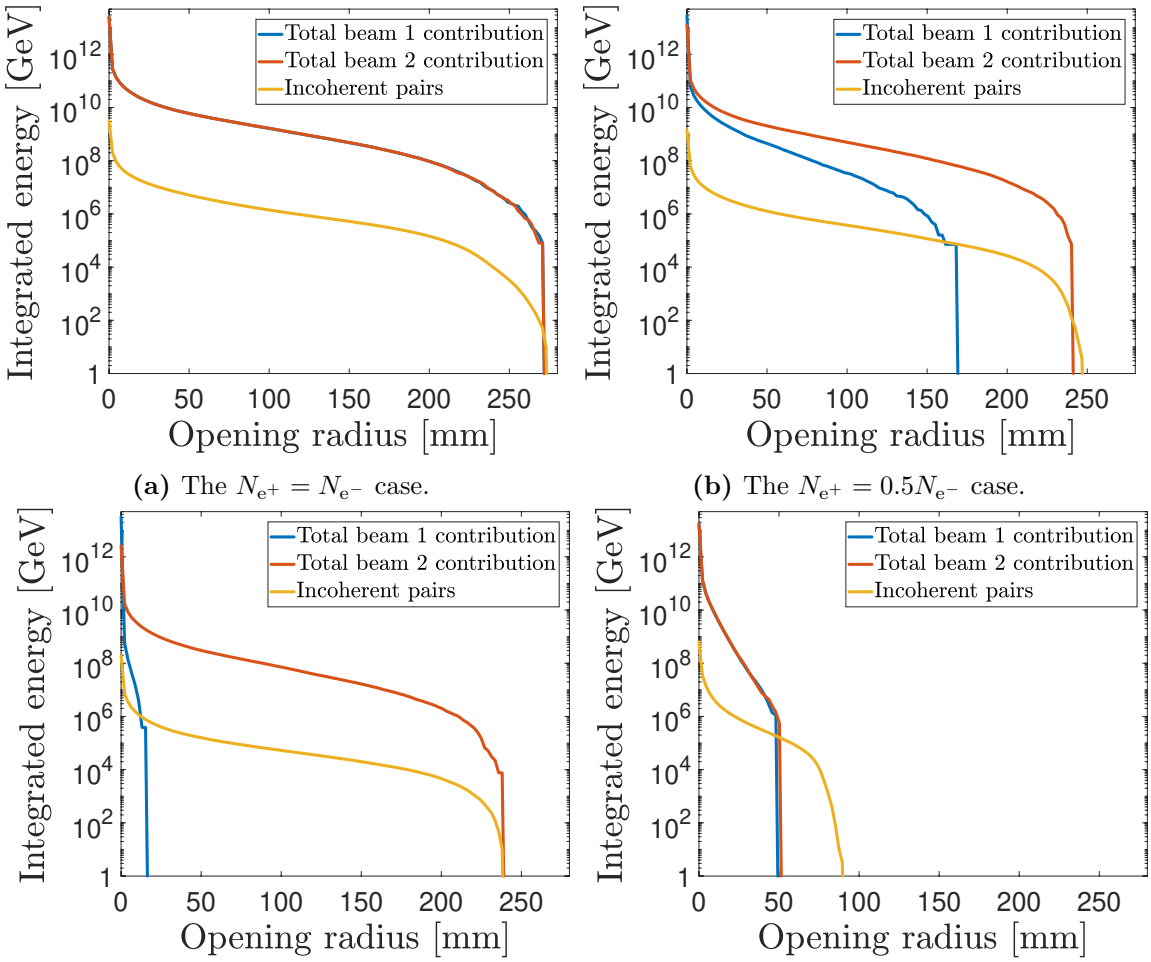

(a) The $N_{e^+} = N_{e^-}$ case.

(b) The $N_{e^+} = 0.5N_{e^-}$ case.

(c) The $N_{e^+} = 0.1N_{e^-}$ case.

(d) The CLIC case.

Figure 4.15: Integrated energy deposited at the detector exit for spent beam particles, coherent pairs and trident pairs associated with the two colliding beams in addition to energy deposited by the incoherent pairs vs. detector opening radius. The detector exit is located 3 m downstream of the IP. $\sqrt{s} = 14$ TeV.

for exit aperture design. In particular, collisions with asymmetric beam charges produce asymmetric backgrounds that need to be taken into account in the detector design.

4.5 Oide effect

In addition, the proposed parameter set has a vertical beta function that is an order of magnitude smaller than what is achievable with current BDS design [27]. Further studies on reducing beam sizes are thus required in order to achieve the luminosity goals. One major obstacle in achieving such a small vertical beta function is the Oide effect [92], which originates from synchrotron radition emitted by electrons traversing a quadrupole magnet in the final focusing system. This changes the energy of the particles and disrupts the focusing effect of the quadrupole magnet, which causes beam size growth. The beam

size growth contribution σ_{Oide} due to the Oide effect is added quadratically to the optical beam size $\sigma = \sqrt{\varepsilon\beta^*}$:

$$\sigma_{\text{tot}}^2 = \sigma^2 + \sigma_{\text{Oide}}^2. \tag{4.34}$$

For a quadrupole magnet with focusing gradient k, thickness L and focus located at a distance l^* from the front end, the Oide effect beam size contribution is [92]

$$\sigma_{\text{Oide}}^2 = \frac{110}{3\sqrt{6\pi}} \lambda\!\!\!^{-}_{\text{e}} r_{\text{e}} \gamma^5 F(\sqrt{k}L, \sqrt{k}l^*) \left(\frac{\varepsilon}{\beta^*}\right)^{5/2} \tag{4.35}$$

and

$$F(\sqrt{k}L, \sqrt{k}l^*) = \int_0^{\sqrt{k}L} |\sin\mu + \sqrt{k}l^* \cos\mu|^3 \left[\int_0^{\mu} (\sin\mu' + \sqrt{k}l^* \cos\mu')^2 \, \mathrm{d}\mu'\right]^2 \mathrm{d}\mu. \tag{4.36}$$

The total beam size is minimum when β^* is chosen as

$$\beta^* = \left[\frac{275}{3\sqrt{6\pi}} \lambda\!\!\!^{-}_{\text{e}} r_{\text{e}} \gamma^5 F(\sqrt{k}L, \sqrt{k}l^*)\right]^{2/7} \gamma \varepsilon_{\text{N}}^{3/7}, \tag{4.37}$$

which gives

$$\sigma_{\text{tot}}^{\text{min}} = \sqrt{\frac{7}{5}} \left[\frac{275}{3\sqrt{6\pi}} \lambda\!\!\!^{-}_{\text{e}} r_{\text{e}} F(\sqrt{k}L, \sqrt{k}l^*)\right]^{1/7} \varepsilon_{\text{N}}^{5/7}, \tag{4.38}$$

where ε_{N} is the normalised emittance.

With CLIC final quadrupole parameters $k = 0.115\,\text{m}^{-2}$, $L = 2.73\,\text{m}$, $l^* = 3.5\,\text{m}$ [27], equation (4.38) gives $\sigma_{y,\text{tot}} = 1.0\,\text{nm}$. Thus, even using properly chosen β_y^*, $\sigma_{\text{tot}}^{\text{min}}$ is still about one order of magnitude larger than the optical beam sizes $\sigma_y = 0.18\,\text{nm}$ for the 3 TeV case and $\sigma_y = 0.083\,\text{nm}$ for the 14 TeV case.

Possible mitigation methods for the Oide effect include reducing the vertical normalised beam emittance, or using weakly focusing thick lenses with large l^*. For the case where k is set to cancel the vertical optical function α_y just at the quadrupole opposite face to the IP, Blanco et al. have performed studies to minimise the Oide effect beam size contribution for CLIC 3 TeV design parameters. The parameters required for the small relative beam size increase is however out of reach for realistic final doublet designs [93]. Octupole magnets have also been proposed, where a simple scheme consisting of placing an octupole in front of the strong focusing quadrupole was able to reduce the Oide beam size contribution with 6% [93].

CHAPTER 5

PWFA Linear Photon Collider Parameter Study

Due to the challenges of accelerating positrons using PWFA, a $\gamma\gamma$ collider, where laser photons are scattered off ultra-relativistic electron beams accelerated by PWFA, has been proposed as an alternative to a PWFA e^+e^- linear collider. A $\gamma\gamma$ collider has the potential to provide a higher luminosity than an e^+e^- collider due to the absence of beamstrahlung in $\gamma\gamma$ collisions, while also offering an attractive discovery potential [56].

This chapter will first give a brief outline of $\gamma\gamma$ collider principles, before the results of the beam-beam study for a multi-TeV $\gamma\gamma$ collider are presented. This beam-beam study again used the electron main beam parameter set in table 3.3 as a basis to optimise parameters at the IP using GUINEA-PIG. Part of the results can also be found in reference [94].

5.1 $\gamma\gamma$ collider principles

The principles of a $\gamma\gamma$ collider are outlined in reference [95, 96]. We will here give a brief summary of the basic concepts.

Inverse Compton scattering of laser photons on relativistic electrons is considered the most efficient method to produce the required high-energy photons. A short distance before the IP, a high-energy electron beam collides with a laser beam in the conversion region. After the Compton scattering process, the back-scattered photons have acquired a large fraction of the incident electrons' energy, and follow the direction of the incident electrons to be collided in the IP with photons that have been back-scattered against the opposite electron beam. An outline of this process is shown in figure 5.1.

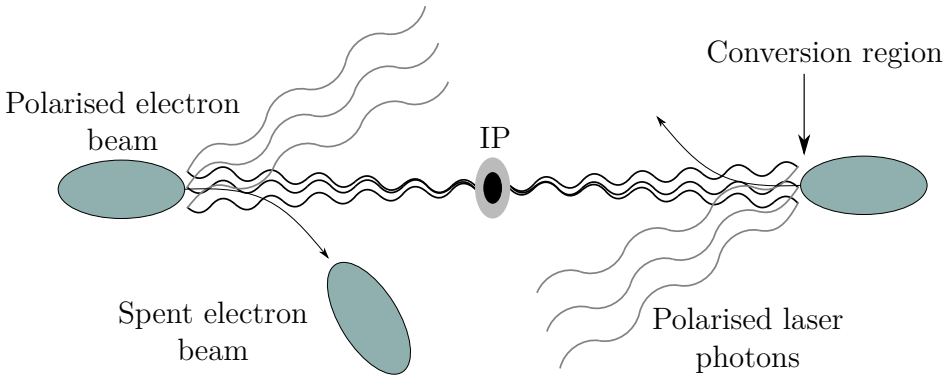

Figure 5.1: Outline of the production of the high-energy photons required for a $\gamma\gamma$ collider through inverse Compton scattering with a polarised electron beam. The conversion takes place in the conversion regions before the interaction point, and the back-scattered high-energy photons collide at the IP. The spent electron beams can either be deflected using a magnetic field or collided at the IP.

5.1.1 Inverse Compton scattering kinematics

Let the four-momentum of two colliding particles with mass m_1 and m_2 be denoted by p_1^μ and p_2^μ. The total four-momentum before collision is $P^\mu = p_1^\mu + p_2^\mu$, and the inner product is

$$P^\mu P_\mu = p_1^\mu p_{1\mu} + p_2^\mu p_{2\mu} + 2p_1^\mu p_{2\mu} = m_1^2c^2 + m_2^2c^2 + 2\left(\frac{\mathscr{E}_1\mathscr{E}_2}{c^2} - \boldsymbol{p}_1 \cdot \boldsymbol{p}_2\right), \tag{5.1}$$

where $\mathscr{E}_i$ and $\boldsymbol{p}_i$ are the energy and momentum of particle i, and we have used the metric tensor $\eta^{\mu\nu} = \mathrm{diag}(1, -1, -1, -1)$.

In the conversion region, laser photons are scattered off ultra-relativistic electrons at small collision angles θ_L as shown in figure 5.2. Before scattering, the electron has energy $\mathscr{E}_0$ and momentum $p_0 \approx \mathscr{E}_0/c$, while that of the photon are $\hbar\omega_0$ and $\hbar k_0$. Equation (5.1) can be written as

$$P^\mu P_\mu = m_\mathrm{e}^2c^2 + 2\left(\frac{\mathscr{E}_0\hbar\omega_0}{c^2} - p_0\hbar k_0\cos(\pi - \theta_\mathrm{L})\right) \tag{5.2}$$

$$\approx m_\mathrm{e}^2c^2 + \frac{4\mathscr{E}_0\hbar\omega_0}{c^2}\cos^2\frac{\theta_\mathrm{L}}{2}. \tag{5.3}$$

We define the dimensionless invariant energy parameter

$$x = \frac{4\mathscr{E}_0\hbar\omega_0}{(m_\mathrm{e}c^2)^2}\cos^2\frac{\theta_\mathrm{L}}{2} \tag{5.4}$$

that can be used as a measure for the energy of the electron-photon system. Since the Mandelstam variable s is defined as $s = (p_1^\mu + p_2^\mu)^2c^2 = \mathscr{E}_\mathrm{CM}^2$, x is related to the centre of mass energy by

$$s = m_\mathrm{e}^2c^4(1 + x). \tag{5.5}$$

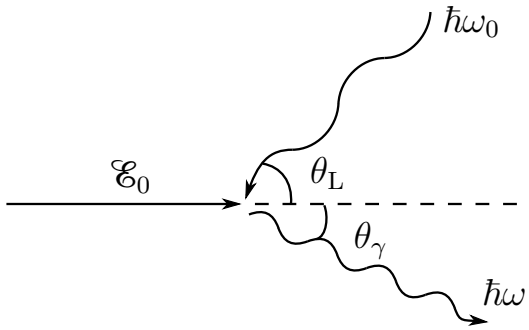

Figure 5.2: Inverse Compton scattering. A photon with energy $\hbar\omega_0$ scatters off an ultra-relativistic electron with energy $\mathscr{E}_0$. The photon's energy after scattering is $\hbar\omega$.

After collision, the majority of the back-scattered photons move in directions given by small angles θ_γ relative to the trajectory of the incoming electron. The frequency of the back-scattered photon is given by

$$\omega = \frac{\omega_{\mathrm{m}}}{1 + (\theta_\gamma/\vartheta_0)^2}, \tag{5.6}$$

where

$$\vartheta_0 = \frac{m_{\mathrm{e}}c^2}{\mathscr{E}_0}\sqrt{x+1} \tag{5.7}$$

and

$$\omega_{\mathrm{m}} = \frac{x}{x+1}\frac{\mathscr{E}_0}{\hbar} \tag{5.8}$$

is the maximum photon frequency, which corresponds to the photon being scattered in the same direction as the incoming electron.

5.1.2 Photon energy spectrum

Let $y = \hbar\omega/\mathscr{E}_0$. The energy spectrum of the back-scattered photons is determined by the quantity $(1/\sigma_{\mathrm{c}})(\mathrm{d}\sigma_{\mathrm{c}}/\mathrm{d}y)$, where σ_{c} is the total cross section of the Inverse scattering process. The differential cross section for the inverse Compton scattering process is given by [95]

$$\begin{aligned}\frac{\mathrm{d}\sigma_{\mathrm{c}}}{\mathrm{d}y} = \frac{2\pi r_{\mathrm{e}}^2}{x}\Bigg[&\frac{1}{1-y} + 1 - y - \frac{4y}{x(1-y)}\left(1 - \frac{y}{x(1-y)}\right)\\ &+\frac{2h_{\mathrm{e}}\Omega y}{1-y}\left(1 - \frac{2y}{x(1-y)}\right)(2-y)\Bigg],\end{aligned} \tag{5.9}$$

where h_{e} is the helicity of the electron and Ω is the polarisation of the initial photon. The total cross section can be written as

$$\begin{aligned}\sigma_{\mathrm{c}} = &\frac{2\pi r_{\mathrm{e}}^2}{x}\left[\left(1 - \frac{4}{x} - \frac{8}{x^2}\right)\ln(x+1) + \frac{1}{2} + \frac{8}{x} - \frac{1}{2(x+1)^2}\right]\\ &+ \frac{4\pi r_{\mathrm{e}}^2 h_{\mathrm{e}}\Omega}{x}\left[\left(1 + \frac{2}{x}\right)\ln(x+1) - \frac{5}{2} + \frac{1}{x+1} - \frac{1}{2(x+1)^2}\right].\end{aligned} \tag{5.10}$$

The sharpness of the photon energy spectrum strongly depends on the value of $2h_e\Omega$, which should ideally be -1. In practice, $2h_e\Omega \approx -0.8$ is a more realistic value, which we adopt in this study.

The energy of the back-scattered photons increases with increasing laser photon energy. However, the back-scattered photons and laser photons may scatter, and if their energy exceeds the threshold for e^+e^- pair creation, high-energy photons will be lost, and unwanted e^+e^- pairs will be created. The energy of the laser photons is thus restricted by e^+e^- pair creation. The total four-momentum before the collision between a back-scattered photon with energy $\hbar\omega_m$ and a laser photon with energy $\hbar\omega_0$ is $P^\mu = \hbar(\omega_m/c + \omega_0/c, \boldsymbol{k}_m + \boldsymbol{k}_0)$. At the threshold energy for the process $\gamma + \gamma \to e^+ + e^-$, the total four-momentum after the collision is $P'^\mu = (2m_e c, \mathbf{0})$. It follows that

$$m_e^2 c^4 = \hbar^2 \omega_m \omega_0. \tag{5.11}$$

Substituting for ω_m from equation (5.8) and using $x \approx 4\mathscr{E}_0\hbar\omega_0/(m_e c^2)^2$, we can find the upper limit for x:

$$xy_m > 4 \implies x < 2 + 2\sqrt{2} \approx 4.8. \tag{5.12}$$

This gives $y_m \approx 0.83$.

The energy spectrum for the back-scattered photons with $x = 4.8$ and various initial electron helicity and photon polarisation is shown in figure 5.3. From figure 5.3, it is evident that polarised laser and electron beams enhance the monochromaticity of the back-scattered photon beam, resulting in a sharper spectrum.

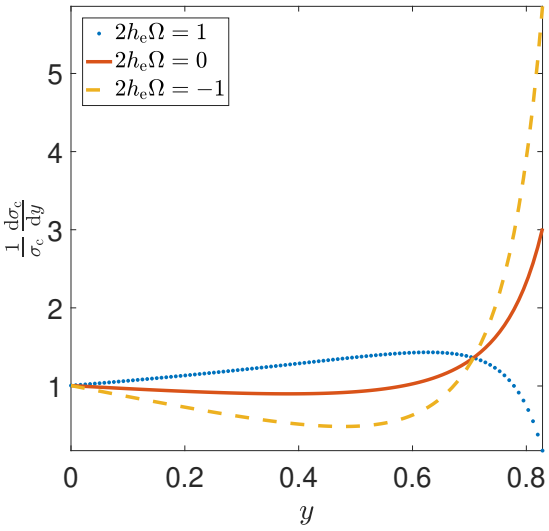

Figure 5.3: Normalised energy spectrum of back-scattered photons with $x = 4.8$ for various values of $2h_e\Omega$.

5.1.3 Conversion efficiency

The spectrum shown in figure 5.3 corresponds to a small conversion efficiency η_γ, which gives the average number of high-energy (back-scattered) photons N_γ per electron

$$\eta_\gamma = \frac{N_\gamma}{N_\mathrm{e}}, \tag{5.13}$$

where N_e is the total number of electrons in the incoming beam.

For $\eta_\gamma \ll 1$, the conversion efficiency for a scattering between an ultra-relativistic electron beam with density n_e and a laser beam with density n_L can be written as

$$\eta_\gamma = \frac{2c\sigma_\mathrm{c}}{N_\mathrm{e}} \int n_\mathrm{e} n_\mathrm{L} \,\mathrm{d}^3 r \mathrm{d}t. \tag{5.14}$$

Here $2c \approx |\boldsymbol{v}_\mathrm{e} - \boldsymbol{v}_\gamma|$ is the speed that the electrons and photons are approaching each other with.

At the conversion region, the rms radius of a Gaussian laser beam at a distance z from the focus is

$$\sigma_\mathrm{L} = a_\mathrm{L} \sqrt{1 + \left(\frac{z}{z_\mathrm{R}}\right)^2}, \tag{5.15}$$

where a_L is the focal spot radius and z_R is the Rayleigh length of the laser.

For a Gaussian laser beam with laser pulse energy A, the density of laser photons is given by

$$n_\mathrm{L} = \frac{A}{\pi \sigma_\mathrm{L}^2 \hbar \omega_0} \mathrm{e}^{-r^2/\sigma_\mathrm{L}^2} F_\mathrm{L}(z + ct), \tag{5.16}$$

with the linear density normalised by $\int F_\mathrm{L}(z)\,\mathrm{d}z = 1$.

Similarly, rms radius and density for a round electron beam are given by

$$\sigma_\mathrm{e} = a_\mathrm{e} \sqrt{1 + \left(\frac{d}{\beta_r}\right)^2} \tag{5.17}$$

$$n_\mathrm{e} = \frac{N_\mathrm{e}}{\pi \sigma_\mathrm{e}^2} \mathrm{e}^{-r^2/\sigma_\mathrm{e}^2} F_\mathrm{e}(z - ct), \tag{5.18}$$

where d is the distance to the interaction point, β_r is the beta function at the interaction point, $\int F_\mathrm{e}(z)\,\mathrm{d}z = 1$ and we also assumed that the lengths l_e and l_L of the electron and laser beams are small compared to d, so that $\sigma_\mathrm{e} \approx$ const. in the conversion region.

For a head-on collision with the centres of both beams passing through the focus simultaneously, integrating equation (5.14) over r gives [96]

$$\eta_\gamma = \frac{A}{A_0} \tag{5.19}$$

$$A_0 = \frac{\pi\hbar\omega_0}{J}\frac{\sigma_\mathrm{e}^2 + a_\mathrm{L}^2}{\sigma_\mathrm{c}} \tag{5.20}$$

$$J = 2c\int \frac{F_\mathrm{e}(z-ct)F_\mathrm{L}(z+ct)}{1+z^2/z_\mathrm{R}^2(1+\sigma_\mathrm{e}^2/a_\mathrm{L}^2)}\,\mathrm{d}z\mathrm{d}t. \tag{5.21}$$

In order to achieve a high photon density at the laser focus during the collision with the electron beam, the laser beam should have the length $l_\mathrm{L} > l_\mathrm{e}$. In the limit $l_\mathrm{L} \gg l_\mathrm{e}$, $2z_\mathrm{R}\sqrt{1+\sigma_\mathrm{e}^2/a_\mathrm{L}^2}$, equation (5.20) and (5.21) are reduced to

$$A_0 = \frac{\hbar c}{2\sigma_\mathrm{c}F_\mathrm{L}(0)}\sqrt{1+\left(\frac{\sigma_\mathrm{e}}{a_\mathrm{L}}\right)^2} \approx \frac{\hbar c l_\mathrm{L}}{2\sigma_\mathrm{c}} \tag{5.22}$$

$$J = 2\pi z_\mathrm{R}F_\mathrm{L}(0)\sqrt{1+\left(\frac{\sigma_\mathrm{e}}{a_\mathrm{L}}\right)^2}. \tag{5.23}$$

We have so far been considering a low collision probability for the electrons, which corresponds to $A \ll A_0$. The conversion efficiency can also be interpreted as the number of electrons that scatter at least once. For $A \gtrsim A_0$, the probability of no scattering is $\exp(-A/A_0)$. The conversion efficiency is thus given by

$$\eta_\gamma = 1 - \mathrm{e}^{-A/A_0}. \tag{5.24}$$

Large laser pulse energies implies a larger number of high-energy photons, but since electrons have an increased chance of multiple scatterings, this will also lead to more low-energy photons. This will enhance the low-energy part of the spectrum, which can be seen from figure 5.4, where the low-energy part of the spectrum is significantly enhanced for high laser pulse energies. This enhancement exceeds the values predicted by the cross section alone, which corresponds to the case where all electrons will scatter only once. Thus, there will be a trade-off between the total luminosity and the sharpness of the luminosity spectrum.

5.1.4 Distance between conversion region and interaction point

The angle of a back-scattered photon with respect to the direction of the initial electron is determined by the photon energy as [95]

$$\theta_\gamma = \frac{m_\mathrm{e}c^2}{\mathscr{E}_0}\sqrt{\frac{x-(x+1)y}{y}} = \vartheta_0\sqrt{\frac{y_\mathrm{m}}{y}-1}, \tag{5.25}$$

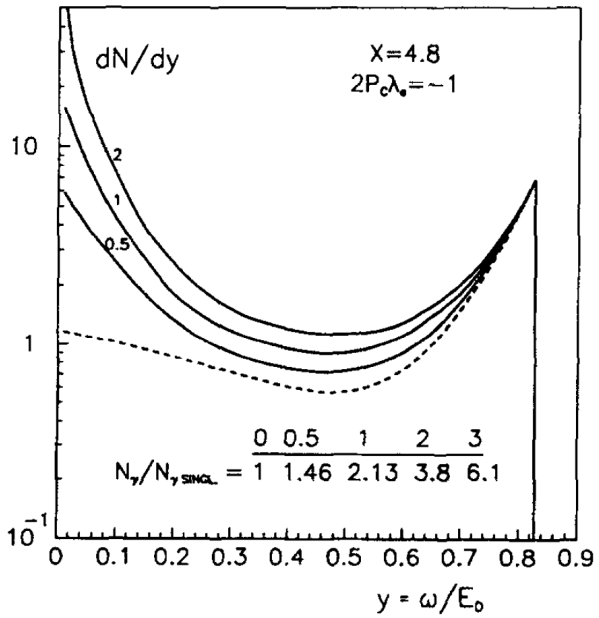

Figure 5.4: Energy spectrum (normalised to maximum) of back-scattered photons with $x = 4.8$ and $2h_e\Omega = -1$ for different values of A/A_0 (marked on the solid curves). The dashed curve is the spectrum corresponding to all electrons scattering only once. Figure is taken from [95].

which decreases with increasing photon energy.

Thus, the contribution to the luminosity from low-energy photons decreases faster over distance compared to high-energy photons. The luminosity spectrum will depend on the distance d between the conversion region and the interaction point. For large distances, the luminosity spectrum will be sharply peaked at high energies, but the total luminosity will decrease. Hence, this represents another trade-off between the total luminosity and the sharpness of the luminosity spectrum.

The dimensionless parameter

$$\varrho = \frac{d}{\gamma\sigma_y^*} \tag{5.26}$$

is often used to describe the distance between the conversion region and the IP.

5.2 Parameter study results

5.2.1 Luminosity optimisation

We initially performed a parameter scan in GUINEA-PIG for a photon collider using electron beam parameters from table 3.3. In particular, we used the parameters $N = 5 \cdot 10^9$, $\mathscr{E}_b = 1.5\,\text{TeV}$, $\gamma\varepsilon_x = 0.887\,\text{mm mrad}$, $\gamma\varepsilon_y = 0.020\,\text{mm mrad}$, $\sigma_z = 2\,\mu\text{m}$, $5\,\mu\text{m}$ and $10\,\mu\text{m}$ and $1\,\mu\text{m} \leq \beta_{x,y}^* \leq 10\,\mu\text{m}$ to assess the σ_z-$\beta_{x,y}^*$-dependence of the luminosity.

The other parameters used in this parameter scan are $x = 4.8$, $2h_e\Omega = -0.8$, $A/A_0 = 1.0$ and $\varrho = 1.0$.

Plots of the total luminosity $\mathcal{L}$ and the peak luminosity $\mathcal{L}_{\text{peak}}$ per beam crossing (bx) are shown in figure 5.5 and 5.6 respectively. The peak luminosity $\mathcal{L}_{\text{peak}}$ is defined here as the part of the luminosity corresponding to centre of mass energy $\sqrt{s} > 0.80 y_m \sqrt{s_0}$, where $\sqrt{s_0}$ is the nominal centre of mass collision energy.

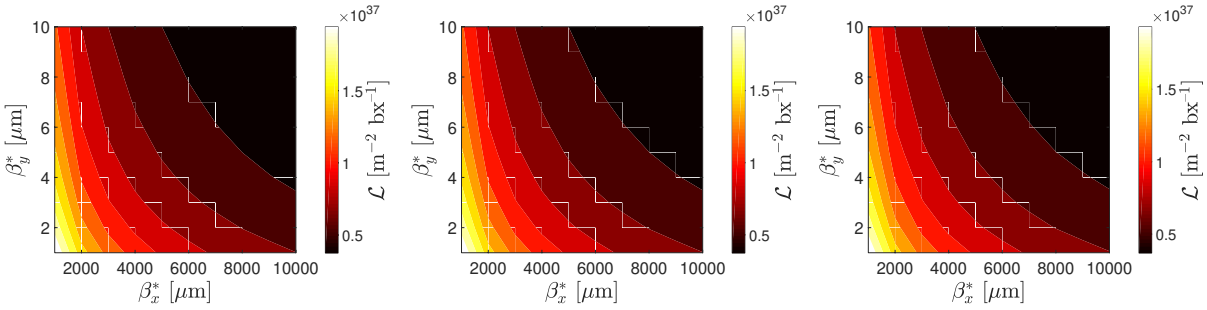

(a) $\sigma_z = 2\,\mu\text{m}$. **(b)** $\sigma_z = 5\,\mu\text{m}$. **(c)** $\sigma_z = 10\,\mu\text{m}$.

Figure 5.5: Contour plots of total luminosity $\mathcal{L}$ vs. horizontal and vertical beta function β_x^* and β_y^* at the interaction point.

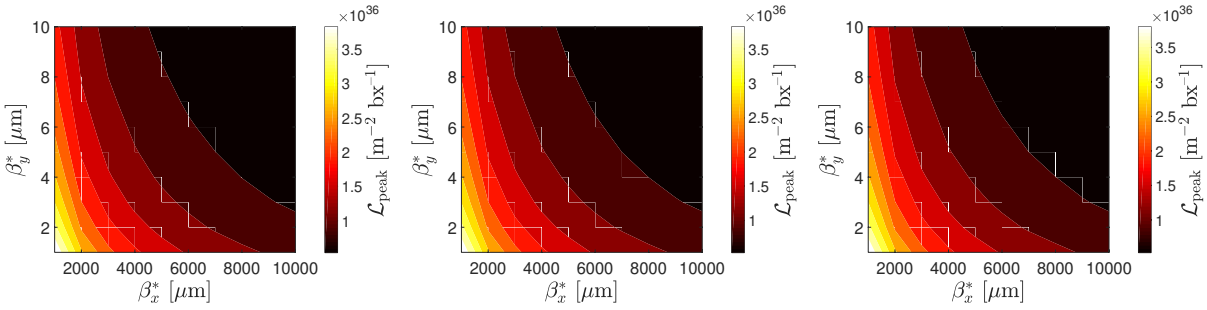

(a) $\sigma_z = 2\,\mu\text{m}$. **(b)** $\sigma_z = 5\,\mu\text{m}$. **(c)** $\sigma_z = 10\,\mu\text{m}$.

Figure 5.6: Contour plots of peak luminosity $\mathcal{L}_{\text{peak}}$ vs. horizontal and vertical beta function β_x^* and β_y^* at the interaction point.

These results indicate that the total luminosity $\mathcal{L}$ and the peak luminosity are independent of σ_z for short beams in the examined interval $2\,\mu\text{m} \leq \sigma_z \leq 10\,\mu\text{m}$ [i]. For e^+e^- collisions, a σ_z-dependence was introduced to the total luminosity through beamstrahlung limitation requirements. This requirement does not apply for $\gamma\gamma$ collisions, so the independence of σ_z is expected. Furthermore, both the luminosity and the sharpness of the spectrum are increased with decreasing β_x^* and β_y^* [ii].

Thus, the total and peak luminosity can be maximised by minimising β_x^* and β_y^*. The CLIC 3 TeV parameter set uses $\beta_x^* = 6.9\,\text{mm}$ and $\beta_y^* = 68\,\mu\text{m}$, which represent the small-

[i] The hourglass effect was avoided since $\beta_y^* \geq \sigma_z$.

[ii] At high energy and larger beam charges, conversion of high energy photons into coherent pairs in the fields of the opposing electron beam can however restrict the horizontal spot size [56].

est beta functions currently achievable. These values for $\beta^*_{x,y}$ however take into account non-linear effects and are not matched to the spot sizes and emittances given in reference [27], so we instead choose to assess the matched values $\beta^*_x = 9.0\,\text{mm}$ and $\beta^*_y = 0.147\,\text{mm}$ in this study. We performed additional GUINEA-PIG simulations for $\gamma\gamma$ collisions of photons scattered at electron beams with $N = 5 \cdot 10^9$ electrons, $\sigma_z = 5\,\mu\text{m}$, $\beta^*_x = 9.0\,\text{mm}$ and $\beta^*_y = 0.147\,\text{mm}$ to study the effect of A/A_0 and ϱ on the luminosity spectrum. The luminosity spectra are plotted against $\chi = \sqrt{s}/\sqrt{s_0}$ in figure 5.7 and 5.8.

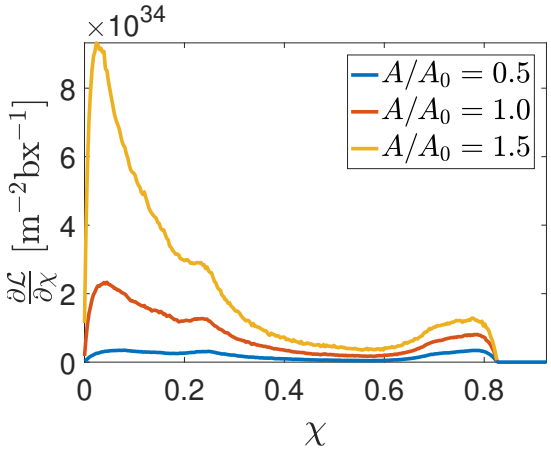

Figure 5.7: Luminosity spectra for $\gamma\gamma$ collisions for a laser with several target thicknesses A/A_0 and the distance $\varrho = 1$ between the conversion region and interaction point. $\chi = \sqrt{s}/\sqrt{s_0}$.

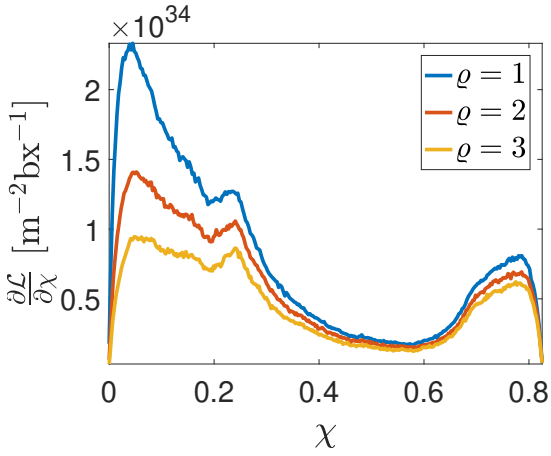

Figure 5.8: Luminosity spectra for $\gamma\gamma$ collisions for a laser with target thickness $A/A_0 = 1$ and several distances ϱ between the conversion region and interaction point. $\chi = \sqrt{s}/\sqrt{s_0}$.

As expected, large laser pulse energies lead to an enhancement of the low-energy part of the luminosity spectrum due to increased chance of multiple scattering and an increased number of low-energy photons. For $A/A_0 = 0.5$, $\mathcal{L}_{\text{peak}}/\mathcal{L} = 0.25$ while $\mathcal{L}_{\text{peak}}/\mathcal{L} = 0.085$ for $A/A_0 = 1.5$. Furthermore, larger values of ϱ result in a decrease in the low-energy part of the spectrum and smaller total luminosities. Large values of ϱ however also enhance the relative sharpness with $\mathcal{L}_{\text{peak}}/\mathcal{L} = 0.14$ for $\varrho = 1.0$ and $\mathcal{L}_{\text{peak}}/\mathcal{L} = 0.20$ for $\varrho = 3.0$. Due to this dependence on ϱ, for a fixed distance d between the conversion point and

the IP, decreasing β_y^* would lead to an improvement of the sharpness of the luminosity spectrum, but the increase in total luminosity would be less than the $1/\sqrt{\beta_y^*}$-scaling.

5.2.2 Background

In this background study, we will consider the case where no beam separation scheme for the e^- beams are applied, and compare the results for two sets of β_x^* and β_y^*. Set 1 contains the previously used values $\beta_x^* = 9.0\,\text{mm}$ and $\beta_y^* = 0.147\,\text{mm}$, while set 2 contains the smallest values $\beta_x^* = 1.0\,\text{mm}$ and $\beta_y^* = 1.0\,\mu\text{m}$ that were considered in this parameter scan. In addition, we will also compare these results with outcomes obtained using the CLIC parameter set[iii]. Other parameters such as $N = 5 \cdot 10^9$ electrons, $\sigma_z = 5\,\mu\text{m}$, $2h_e\Omega = -0.8$, $A/A_0 = 1.0$, and $\varrho = 1.0$ are kept identical for all parameter sets.

Table 5.1 summarises key figures such as the total number of different types of background particles produced per beam crossing. Several types of luminosities and energies are also listed. As expected, parameter set 2 results in the highest $\gamma\gamma$ luminosity $\mathcal{L}_{\gamma\gamma}$ and also has the sharpest $\gamma\gamma$ luminosity spectrum.

$\mathcal{L}_{\gamma\gamma}$ of set 1 is larger than expected compared to the CLIC set, which should only have been a factor ~ 1.56 larger due to the $N^2/\sqrt{\varepsilon_x}$ scaling of luminosity. In order to examine if this is caused by the difference in σ_z, we performed a separate simulation using set 1 parameters except replacing $\sigma_z = 5\,\mu\text{m}$ with $\sigma_z = 44\,\mu\text{m}$. This separate simulation resulted in $\mathcal{L}_{\gamma\gamma} = 8.48 \cdot 10^{35}\,\text{m}^{-2}\text{bx}^{-1}$ and $\mathcal{L}_{\gamma\gamma}^{\text{peak}} = 1.27 \cdot 10^{35}\,\text{m}^{-2}\text{bx}^{-1}$, which agree well with the $N^2/\sqrt{\varepsilon_x}$-scaling and indicate a σ_z dependence for large σ_z.

Compared to $\mathcal{L}_{\gamma\gamma}$, both the γe^- luminosity $\mathcal{L}_{\gamma e^-}$ and the e^-e^- luminosity $\mathcal{L}_{e^-e^-}$ are 2–3 orders of magnitude lower for all three parameter sets.

The number of background particles for parameter set 2 is higher than the other sets, which is expected due to more intense beam fields leading to the production of more particles. The total energies of the background particles are also highest for parameter set 2, so that it overall produces the strongest background.

In a $\gamma\gamma$ collider whose electron beams have not been separated after conversion, secondary e^+e^- pairs can be created through all the processes described in subsection 4.2.2 and 4.2.3. Production of secondary e^+e^- pairs are however suppressed due to the Compton backscattering, which leads to energy-depleted beams with reduced beam fields. Reduced fields will suppress the production of both coherent and trident pairs, with the reduction in trident pairs being especially significant, as the trident cascade process requires $\Upsilon \gg 1$. The energy depleted beams also lead to smaller total scattering cross sections for the Bethe-Heitler and Landau-Lifshitz processes, which suppresses the production of in-

[iii] Using $\beta_x^* = 9.0\,\text{mm}$ and $\beta_y^* = 0.147\,\text{mm}$.

Quantity	Unit	Set 1	Set 2	CLIC
N	10^9	5.0	5.0	3.72
σ_z	µm	5.0	5.0	44.0
β_x^*	mm	9.0	1.0	9.0
β_y^*	µm	147	1.0	147
$\gamma\varepsilon_x$	mm mrad	0.887	0.887	0.66
$\gamma\varepsilon_y$	mm mrad	0.02	0.02	0.02
$\mathcal{L}_{\gamma\gamma}$	$10^{35}\,\mathrm{m}^{-2}\ \mathrm{bx}^{-1}$	12.09	209.16	5.45
$\mathcal{L}_{\gamma\gamma}^{\mathrm{peak}}$	$10^{35}\,\mathrm{m}^{-2}\ \mathrm{bx}^{-1}$	1.72	41.51	0.85
$\mathcal{L}_{\gamma\mathrm{e}^-}$	$10^{35}\,\mathrm{m}^{-2}\ \mathrm{bx}^{-1}$	0.06	1.08	0.03
$\mathcal{L}_{\mathrm{e}^-\mathrm{e}^-}$	$10^{35}\,\mathrm{m}^{-2}\ \mathrm{bx}^{-1}$	0.05	0.56	0.02
N_{coh}	10^8	1.73	13.49	0.08
$\mathscr{E}_{\mathrm{coh}}$	$10^{11}\,\mathrm{GeV}$	0.33	1.66	0.03
N_{tri}	10^7	0.91	5.45	0.04
$\mathscr{E}_{\mathrm{tri}}$	$10^9\,\mathrm{GeV}$	1.03	2.70	0.10
N_{inc}	10^5	0.26	3.46	0.12
$\mathscr{E}_{\mathrm{inc}}$	$10^7\,\mathrm{GeV}$	0.12	2.12	0.06
N_{H}		70.15	1291.33	33.17

Table 5.1: Luminosity and background comparison.

coherent pairs. This suppression becomes evident by comparing the results for the CLIC parameter set in table 5.1 with the corresponding results in table 4.6.

The cross section for the direct scattering process $\gamma\gamma \to \mathrm{q\bar{q}}$ falls with energy, but the cross section for resolved photon processes increases with the incident photon energies. In a $\gamma\gamma$ collider, the incident photons are more energetic than in an $\mathrm{e^+e^-}$ collider, which result in stronger hadronic backgrounds. Again comparing table 5.1 and 4.6, we see that the number of hadronic events per beam crossing in a $\gamma\gamma$ collider is significantly higher than in an $\mathrm{e^+e^-}$ collider.

The total numbers of hits per beam crossing in a vertex detector with basic detector parameters as outlined in table 4.1 are listed in table 5.2. Comparing the results for CLIC parameters to the number of hits found in table 4.8, we find a significantly lower number of hits in the $\gamma\gamma$ case. Lastly, the integrated energies deposited at the detector exit are plotted against exit opening radius in figure 5.2. Parameter set 2, which has the highest number of background particles, also has the most severely deflected particles of the three cases, with the incoherent pairs reaching exit aperture radius of $\sim 160\,\mathrm{mm}$.

In summary, the examined $\gamma\gamma$ collider parameter sets can deliver significantly larger total luminosities than the examined $\mathrm{e^+e^-}$ collider parameter sets shown in table 4.4, while also offering reduced background contribution from secondary $\mathrm{e^+e^-}$ pairs. However, the

Parameter set	Unit	Beam	Coh.	Tri.	Incoh.
Set 1	10^4	0	380.0	0	0.32
Set 2	10^4	0	2000.0	0	4.1
CLIC		0	0	0	61

Table 5.2: Total number of hits in the vertex detector from the spent beam (Beam), coherent pairs (Coh.), trident pairs (Tri.) and incoherent pairs (Incoh.) for the three parameter sets.

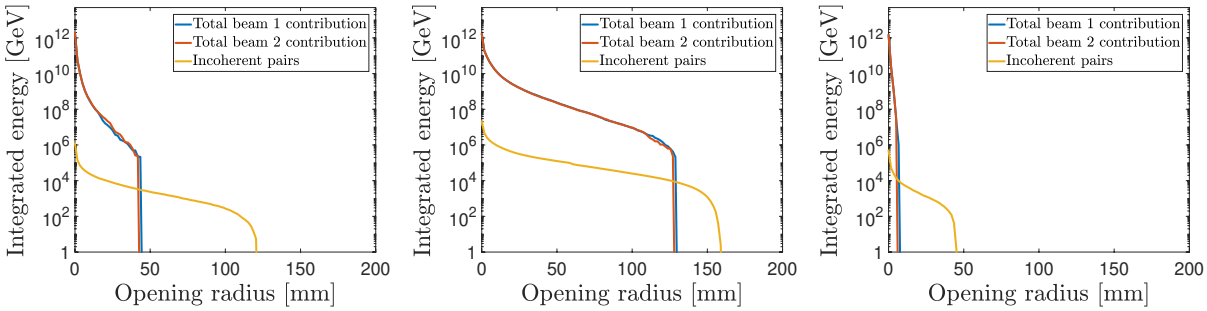

(a) Parameter set 1. **(b)** Parameter set 2. **(c)** CLIC parameter set.

Figure 5.9: Integrated energy deposited at the detector exit for spent beam particles, coherent pairs and trident pairs associated with the two colliding beams in addition to energy deposited by the incoherent pairs vs. detector opening radius. The detector exit is located 3 m downstream of the IP. $\sqrt{s} = 3$ TeV.

luminosity spreads, and hadronic backgrounds are comparatively larger.

CHAPTER 6

Conclusion

6.1 Summary

The objective of this thesis was to establish parameter sets for multi-TeV PWFA e^+e^- and $\gamma\gamma$ colliders that take into account the constraint on efficiency imposed by transverse instabilities induced by transverse wakefields.

Even though several conceptual parameter sets for a PWFA linear collider have been proposed, no PWFA linear collider studies have so far considered the constraint of efficiency imposed by transverse instabilities. In this thesis, we described the transverse instabilities in PWFA using the wakefield formalism used in CLIC parameter studies [27], and benchmarked the results against QuickPIC simulation results in chapter 3. Using the wakefield formalism, a simplified quasi-static model was developed, and was combined with QuickPIC simulations in order to model the evolution of the transverse oscillations of the main beam over a 1.5 TeV PWFA electron accelerator.

We demonstrated that the Snowmass parameter set was unable to provide sufficiently stable propagation for a main beam consisting of electrons, and we performed a parameter scan over the main beam charge, rms beam length and beam separation distance using the Snowmass parameter set as a basis. The energy spread is induced by beam loading as a result of placing the main beam at different phases of the longitudinal wakefield. By selecting an operating point with a reasonable compromise between stability, energy spread and efficiency from the parameter scan results, we derived a new set of PWFA electron accelerator parameters summarised in table 4.2. This parameter set improves the Snowmass parameter set in terms of energy spread, stability and luminosity per power and is the basis for collider parameter studies in chapter 4 and 5.

In addition, chapter 3 also presented a second accelerator parameter scan where we assumed that linear energy chirps of different longitudinal profiles can be introduced to the main beam independently of other parameters such as beam charge and beam separation distance. The results indicate that the required energy chirps are in good agreement with the predictions of the BNS damping requirement.

Results in chapter 4 demonstrate that beamstrahlung can be suppressed with short beams, which allows the horizontal beam size to be reduced appropriately in order to increase luminosity without increasing beamstrahlung. This results in a $1/\sqrt{\sigma_z}$-scaling of the total luminosity, which is beneficial for PWFA, as short beams are preferred for PWFA. Chapter 4 then derived a parameter set for a 3 TeV e^+e^- PWFA linear collider outlined in table 4.2 that shows a promising level of luminosity, while maintaining a reasonable luminosity spread. Even for a scenario where the positron beam only contains 10% of the particles in the electron beam, the derived parameter set can still provide luminosity per beam crossing comparable to that of CLIC at 3 TeV. At 14 TeV, the derived collider parameter set is able to achieve the luminosity goal of $40 \cdot 10^{34}\,\mathrm{cm}^{-2}\,\mathrm{s}^{-1}$ with a significantly lower beam power than the CLIC parameter set. These parameters are however not optimised for this energy level, and thus give rise to a large luminosity spread. The proposed parameter set furthermore has a vertical beta function that is an order of magnitude smaller than what is currently achievable. The CLIC parameter set has minimised the beam sizes by optimising the damping ring and the beam delivery system. The Oide effect is a major obstacle in achieving such small beta functions, which entails challenges for the final focusing system design. Thus, further studies in reducing the beam sizes are required in order to achieve the luminosity goals. However, despite the derived PWFA e^+e^- collider parameter sets being able to offer interesting improvements over the CLIC parameter set, the stronger fields in the PWFA beams also lead to significantly stronger backgrounds that result in more hits in the vertex detector and require larger exit openings. Collisions with asymmetric beam charges will also produce asymmetric backgrounds that should be considered in the detector design.

Due to the challenges of accelerating positrons in a plasma, and the possibility of achieving a higher luminosity than e^+e^- collisions in collisions with high-energy photons due to the absence of beamstrahlung, a $\gamma\gamma$ collider can be considered as an alternative to an e^+e^- collider. The absence of beam-beam effects in $\gamma\gamma$ collisions allows for increasing the total luminosity by minimising $\beta^*_{x,y}$ of incoming electron beams used for back-scattering photons, as shown in chapter 5.

The combined parameter set consisting of the derived PWFA beam parameters and smallest currently achievable $\beta^*_{x,y}$ is able to provide a significantly higher total luminosity than a $\gamma\gamma$ collider based on CLIC parameters, but also produces a larger background. The examined $\gamma\gamma$ collider parameters in table 5.1 can also deliver significantly larger total luminosities than the examined e^+e^- collider parameters in table 4.4 with a smaller background contribution from secondary e^+e^- pairs compared to a similar e^+e^- collider. This

however comes at the expense of larger luminosity spreads and hadronic backgrounds.

6.2 Future outlooks

The parameter study in chapter 3 is not exhaustive, and did not consider the effects of beam induced ion motion, which has been shown to mitigate hose instability [76, 77]. Recent studies also indicate that emittance growth arising from ion motion may not be as severe as previously anticipated [97], so ion motion should be considered as another mitigation mechanism for transverse instabilities in addition to damping using energy spread. If these two mitigation mechanisms can be combined, the energy spread required to achieve acceptable beam stability may be reduced and the constrain on the maximum amount of beam particles that can be accelerated may also be relaxed. The additional damping from ion motion may in certain cases even allow the main beam to be placed further behind inside the plasma ion bubble to achieve a higher efficiency.

Technical constraints were rarely considered in this thesis, but in order to arrive at a conceptual design report for a PWFA-based collider, design work carried out in parallel with further technical development is required, as parameter optimisation will be affected by technical choices. This will require test facilities capable of addressing challenges such as emittance preservation at the mm mrad-level, energy spread minimisation through beam loading and operation with beam trains in addition to the challenges mentioned above. There are currently less than ten facilities in the world that are capable of delivering particle beams suitable for PWFA experiments, i.e. nC particle beams with sub-ps length and GeV energy focused to sub-mm transverse sizes [43]. In the ALEGRO input for the 2020 update of the European Strategy for Particle Physics [43, 44], it was stated that the major goal of the collaboration is to construct dedicated advanced and novel accelerator facilities that can reliably deliver high-quality, multi-GeV electron beams from a small number of stages in the coming decade.

Even though PWFA experiments have already successfully demonstrated important milestones such as two-beam acceleration [35], acceleration of electrons at high gradient ($\sim 50\,\mathrm{GV/m}$) over a metre-scale plasma [36] and energy transfer efficiency from the drive to the main beam of 30 % [37], important elements such as staging of multi-GeV acceleration stages, reliable acceleration of positrons and acceleration of collider-grade beams remain to be demonstrated. On the modelling and simulation front, it is envisioned that future exascale computing can drastically reduce computation time, while theory and machine learning algorithms will be deployed to develop fast models that can guide large-scale parameter scans.

Another proposed collider option that has recently seen an increased interest is the muon collider, envisioned to collide muons and anti-muons at multi-TeV centre of mass energies. Since muons are fundamental particles, they possess the potential to produce very high-energy collisions that can transfer all energy into the production of new particles. In

comparison, only a fraction of the energy carried by colliding partons is available for the hard collisions. This potential is highlighted in the Muon Collider Working Group's input to the European Strategy for Particle Physics, where the report emphasised that a 14 TeV muon collider can provide an effective energy reach similar to that of a 100 TeV FCC proton-proton collider [91].

However, the mean lifetime of muons at rest is 2.2 µs, which constitute major challenges for achieving high luminosities. In order to minimise the loss of muons through decay, muon beams must be cooled to low emittances and accelerated to collision energies on short timescales. Plasma acceleration with their high gradients may thus be a suitable accelerator choice for a muon collider.

From the ancient atomists of Greece to the dreams of future high-energy colliders, humanity's quest for knowledge has seen remarkable triumphs and uncovered profound wonders motivated by fundamental human curiosity, often independently of immediate practical applications. Nevertheless, era-defining technological revolutions that have transformed our civilisation can often be traced back to discoveries in fundamental physics that seemed of little relevance to the everyday life of their time. It is thus of paramount importance that fundamental research continues independently of immediate potentials for applications. After all, there are few ideas that are more detrimental to a civilisation's continued prosperity than the arrogant delusion that our knowledge is sufficient, that there are no worthwhile frontiers to be conquered and that there are no wonders of value left to be discovered.

Considering the many remaining enigmas in fundamental physics, it is only to be expected that the most profound discoveries are yet ahead of us, hidden beyond our current horizon. It has been a true pleasure and honour to give my contribution in expanding this horizon in the form of this thesis – however humble it might be.

Bibliography

[1] G. Aad, T. Abajyan, B. Abbott, J. Abdallah, *et al.*, "Measurements of Higgs boson production and couplings in diboson final states with the ATLAS detector at the LHC," *Phys. Lett. B*, vol. 726, 2013.

[2] S. Chatrchyan, V. Khachatryan, A. Sirunyan, A. Tumasyan, *et al.*, "Combination of standard model Higgs boson searches and measurements of the properties of the new boson with a mass near 125 GeV," tech. rep., Apr 2013.

[3] F. Englert and R. Brout, "Broken symmetry and the mass of gauge vector mesons," *Phys. Rev. Lett.*, vol. 13, Aug 1964.

[4] P. W. Higgs, "Broken symmetries and the masses of gauge bosons," *Phys. Rev. Lett.*, vol. 13, Oct 1964.

[5] P. W. Higgs, "Broken symmetries, massless particles and gauge fields," *Phys. Lett.*, vol. 12, no. 2, 1964.

[6] G. S. Guralnik, C. R. Hagen, and T. W. B. Kibble, "Global conservation laws and massless particles," *Phys. Rev. Lett.*, vol. 13, Nov 1964.

[7] O. Chamberlain, E. Segrè, C. Wiegand, and T. Ypsilantis, "Observation of antiprotons," *Phys. Rev.*, vol. 100, Nov 1955.

[8] G. Danby, J. Gaillard, K. A. Goulianos, L. Lederman, *et al.*, "Observation of high-energy neutrino reactions and the existence of two kinds of neutrinos," *Phys. Rev. Lett.*, vol. 9, 1962.

[9] J. J. Aubert, U. Becker, P. J. Biggs, J. Burger, *et al.*, "Experimental observation of a heavy particle J," *Phys. Rev. Lett.*, vol. 33, Dec 1974.

[10] J. E. Augustin, A. M. Boyarski, M. Breidenbach, F. Bulos, *et al.*, "Discovery of a narrow resonance in e^+e^- annihilation," *Phys. Rev. Lett.*, vol. 33, Dec 1974.

[11] R. Brandelik *et al.*, "Evidence for planar events in e^+ e^- annihilation at high-

energies," *Phys. Lett. B*, vol. 86, 1979.

[12] C. Berger, H. Genzel, R. Grigull, W. Lackas, *et al.*, "Evidence for gluon bremsstrahlung in e^+e^- annihilations at high energies," *Phys. Lett. B*, vol. 86, no. 3, 1979.

[13] G. Arnison, A. Astbury, B. Aubert, C. Bacci, *et al.*, "Experimental observation of isolated large transverse energy electrons with associated missing energy at $\sqrt{s} =$ 540 GeV," *Phys. Lett. B*, vol. 122, no. 1, 1983.

[14] P. Bagnaia, M. Banner, R. Battiston, P. Bloch, *et al.*, "Evidence for $Z^0 \to e^+e^-$ at the CERN pp collider," *Phys. Lett. B*, vol. 129, no. 1, 1983.

[15] G. Aad, T. Abajyan, B. Abbott, J. Abdallah, *et al.*, "Observation of a new particle in the search for the Standard Model Higgs boson with the ATLAS detector at the LHC," *Phys. Lett. B*, vol. 716, no. 1, 2012.

[16] S. Chatrchyan, V. Khachatryan, A. Sirunyan, A. Tumasyan, *et al.*, "Observation of a new boson at a mass of 125 GeV with the CMS experiment at the LHC," *Phys. Lett. B*, vol. 716, no. 1, 2012.

[17] P. Spentzouris, J. Cary, L. McInnes, W. Mori, *et al.*, "Community petascale project for accelerator science and simulation: Advancing computational science for future accelerators and accelerator technologies," *J. Phys. Conf. Ser.*, vol. 125, Aug 2008.

[18] P. Chen, G. Horton-Smith, T. Ohgaki, A. Weidemann, *et al.*, "CAIN: Conglomérat d'abel et d'interactions non-linéaires," *Nucl. Instr. Meth. Phys. Res. Sec. A*, vol. 355, no. 1, 1995.

[19] D. Schulte, *Study of Electromagnetic and Hadronic Background in the Interaction Region of the TESLA Collider*. PhD thesis, Hamburg U., 1997.

[20] K. Wille and J. McFall, *The Physics of Particle Accelerators: An Introduction*. Oxford University Press, 2000.

[21] M. A. Thomson, "Model-independent measurement of the $e^+e^- \to HZ$ cross section at a future e^+e^--linear collider using hadronic Z decays," *Eur. Phys. J. C*, vol. 76, Feb 2016.

[22] H. Abramowicz, A. Abusleme, K. Afanaciev, N. Alipour Tehrani, *et al.*, "Higgs physics at the CLIC electron–positron linear collider," *Eur. Phys. J. C*, vol. 77, Jul 2017.

[23] "2020 Update of the European Strategy for Particle Physics (Brochure)," Tech. Rep. CERN-ESU-015, Geneva, 2020.

[24] R. K. Ellis, B. Heinemann, J. de Blas, M. Cepeda, *et al.*, "Physics Briefing Book:

Input for the European Strategy for Particle Physics Update 2020," Tech. Rep. arXiv:1910.11775, Geneva, Oct 2019.

[25] A.-M. Liénard, "L'eclairage electrique," 1898.

[26] C. Adolphsen, M. Barone, B. Barish, K. Buesser, *et al.*, "The International Linear Collider Technical Design Report," tech. rep., Geneva, Jun 2013.

[27] M. Aicheler, P. Burrows, M. Draper, T. Garvey, *et al.*, *A Multi-TeV Linear Collider Based on CLIC Technology: CLIC Conceptual Design Report*. CERN Yellow Reports: Monographs, Geneva: CERN, 2012.

[28] M. Benedikt, A. Blondel, O. Brunner, M. Capeans Garrido, *et al.*, "FCC-ee: The Lepton Collider: Future Circular Collider Conceptual Design Report Volume 2. Future Circular Collider," Tech. Rep. CERN-ACC-2018-0057. 2, CERN, Geneva, Dec 2018.

[29] M. Benedikt, M. Capeans Garrido, F. Cerutti, B. Goddard, *et al.*, "FCC-hh: The Hadron Collider: Future Circular Collider Conceptual Design Report Volume 3. Future Circular Collider," Tech. Rep. CERN-ACC-2018-0058, CERN, Geneva, Dec 2018.

[30] The CEPC Study Group, "CEPC conceptual design report: Volume 1 - accelerator," 2018, arXiV: 1809.00285.

[31] W. Wuensch, "CLIC Accelerating Structure Development," Sep 2008.

[32] D. Schulte, "Application of advanced accelerator concepts for colliders," *Rev. of Accel. Sci. and Tech.*, vol. 09, 2016.

[33] S. M. Hooker, R. Bartolini, S. P. D. Mangles, A. Tünnermann, *et al.*, "Multi-pulse laser wakefield acceleration: a new route to efficient, high-repetition-rate plasma accelerators and high flux radiation sources," *J. Phys. B*, vol. 47, Nov 2014.

[34] T. Tajima and J. M. Dawson, "Laser electron accelerator," *Phys. Rev. Lett.*, vol. 43, Jul 1979.

[35] J. B. Rosenzweig, D. B. Cline, B. Cole, H. Figueroa, *et al.*, "Experimental observation of plasma wake-field acceleration," *Phys. Rev. Lett.*, vol. 61, Jul 1988.

[36] I. Blumenfeld, C. Clayton, F.-J. Decker, M. Hogan, *et al.*, "Energy doubling of 42 GeV electrons in a metre-scale plasma wakefield accelerator," *Nature*, vol. 445, Mar 2007.

[37] M. Litos *et al.*, "High-efficiency acceleration of an electron beam in a plasma wakefield accelerator," *Nature*, vol. 515, no. 7525, 2014.

[38] V. Lebedev, A. Burov, and S. Nagaitsev, "Luminosity limitations of linear colliders based on plasma acceleration," *Rev. of Accel. Sci. and Tech.*, vol. 09, 2016.

[39] "Advanced accelerator development strategy report: DOE advanced accelerator concepts research roadmap workshop," tech. rep., Feb 2016.

[40] B. Cros and P. Muggli, "Towards a Proposal for an Advanced Linear Collider Report on the Advanced and Novel Accelerators for High Energy Physics Roadmap Workshop, CERN, Geneva, April 2017," tech. rep., Dec 2017.

[41] E. Adli, J.-P. Delahaye, S. J. Gessner, M. J. Hogan, *et al.*, "A Beam Driven Plasma-Wakefield Linear Collider: From Higgs Factory to Multi-TeV," in *Community Summer Study 2013: Snowmass on the Mississippi*, Aug 2013.

[42] E. Adli, "Plasma wakefield linear colliders–opportunities and challenges," *Phil. Trans. R. Soc. A.*, vol. 377, 2019.

[43] B. Cros and P. Muggli, "ALEGRO input for the 2020 update of the European Strategy," Jan 2019.

[44] ALEGRO collaboration, "Towards an advanced linear international collider," 2019, arXiV: 1901.10370.

[45] E. Gschwendtner, E. Adli, L. Amorim, R. Apsimon, *et al.*, "AWAKE, the advanced proton driven plasma wakefield acceleration experiment at cern," *Nucl. Instr. Meth. Phys. Res. Sec. A*, vol. 829, Dec 2015.

[46] M. Litos, E. Adli, J. Allen, W. An, *et al.*, "9 GeV energy gain in a beam-driven plasma wakefield accelerator," *Plasma Physics and Controlled Fusion*, vol. 58, Nov 2015.

[47] J. Vieira and J. T. Mendonça, "Nonlinear laser driven donut wakefields for positron and electron acceleration," *Phys. Rev. Lett.*, vol. 112, May 2014.

[48] S. Gessner, *Demonstration of the hollow channel wakefield accelerator*. PhD thesis, Stanford University, Sep 2016.

[49] S. Gessner, E. Adli, J. Allen, W. An, *et al.*, "Demonstration of a positron beam-driven hollow channel plasma wakefield accelerator," *Nature Communications*, vol. 7, Jun 2016.

[50] C. A. Lindstrøm, E. Adli, J. M. Allen, W. An, *et al.*, "Measurement of transverse wakefields induced by a misaligned positron bunch in a hollow channel plasma accelerator," *Phys. Rev. Lett.*, vol. 120, Mar 2018.

[51] S. Diederichs, T. J. Mehrling, C. Benedetti, C. B. Schroeder, *et al.*, "Positron transport and acceleration in beam-driven plasma wakefield accelerators using plasma

columns," *Phys. Rev. Accel. Beams*, vol. 22, Aug 2019.

[52] S. Diederichs, C. Benedetti, E. Esarey, J. Osterhoff, *et al.*, "High-quality positron acceleration in beam-driven plasma accelerators," *Phys. Rev. Accel. Beams*, vol. 23, Dec 2020.

[53] I. F. Ginzburg, G. Kotkin, V. G. Serbo, and V. I. Telnov, "Production of high-energy colliding $\gamma\gamma$ and γe beams with a high luminosity at VLEPP accelerators," *JETP Lett.*, vol. 34, Nov 1981.

[54] C. Akerlof, "Using the SLC as a photon accelerator," 1981.

[55] W. Chou, "$\gamma\gamma$ collider – a brief history and recent developments," *CERN Proc.*, vol. 1, 2018.

[56] V. I. Telnov, "Physics goals and parameters of photon colliders," *Int. J. Mod. Phys. A*, vol. 13, 1998.

[57] B. Badelek, C. Blöchinger, J. Blümlein, E. Boos, *et al.*, "The photon collider at TESLA," *Int. J. Mod. Phys. A*, vol. 19, Dec 2004.

[58] M. J. Boland, U. Felzmann, P. J. Giansiracusa, T. G. Lucas, *et al.*, *Updated baseline for a staged Compact Linear Collider*. CERN Yellow Reports: Monographs, Geneva: CERN, Aug 2016.

[59] A. W. Chao, *Physics of Collective Beam Instabilities in High-Energy Accelerators*. New York: Wiley, 1993.

[60] K. Bane and K. LF, "Short-range dipole wakefields in accelerating structures for the NLC," Aug 2020.

[61] R. Keinigs and M. E. Jones, "Two-dimensional dynamics of the plasma wakefield accelerator," *The Physics of Fluids*, vol. 30, no. 1, 1987.

[62] W. Lu, C. Huang, M. Zhou, W. Mori, *et al.*, "Nonlinear theory for relativistic plasma wakefields in the blowout regime," *Phys. Rev. Lett.*, vol. 96, May 2006.

[63] P. B. Wilson, "Introduction to Wake Fields and Wake Potentials," in *Physics of particle accelerators Proc., Fermilab Summer School 1987, Cornell Summer School 1988*, vol. 184, (Fermilab), American Institute of Physics, 1989.

[64] V. Lebedev, A. Burov, and S. Nagaitsev, "Efficiency versus instability in plasma accelerators," *Phys. Rev. Accel. and Beams*, vol. 20, Dec 2017.

[65] G. Stupakov, "Short-range wakefields generated in the blowout regime of plasma-wakefield acceleration," *Phys. Rev. Accel. Beams*, vol. 21, Apr 2018.

[66] M. Kelliher and R. Beadle, "Pulse-shortening in electron linear accelerators," *Nature*, vol. 187, Sep 1960.

[67] W. Panofsky and M. Bander, "Asymptotic theory of beam breakup in linear accelerators," *Rev. Sci. Instrum.*, vol. 39, 1968.

[68] D. H. Whittum, W. M. Sharp, S. S. Yu, M. Lampe, *et al.*, "Electron-hose instability in the ion-focused regime," *Phys. Rev. Lett.*, vol. 67, Aug 1991.

[69] J. B. B. Chen, D. Schulte, and E. Adli, "Modeling and simulation of transverse wakefields in PWFA," *J. Phys. Conf. Ser.*, vol. 1596, Jul 2020.

[70] C. Huang, V. Decyk, C. Ren, M. Zhou, *et al.*, "QUICKPIC: A highly efficient particle-in-cell code for modeling wakefield acceleration in plasmas," *J. Comp. Phys.*, vol. 217, no. 2, 2006.

[71] C. Huang, W. Lu, M. Zhou, C. E. Clayton, *et al.*, "Hosing instability in the blow-out regime for plasma-wakefield acceleration," *Phys. Rev. Lett.*, vol. 99, Dec 2007.

[72] T. J. Mehrling, R. A. Fonseca, A. Martinez de la Ossa, and J. Vieira, "Mitigation of the hose instability in plasma-wakefield accelerators," *Phys. Rev. Lett.*, vol. 118, Apr 2017.

[73] C. Joshi, E. Adli, W. An, C. E. Clayton, *et al.*, "Plasma wakefield acceleration experiments at FACET-II," *Plasma Physics and Controlled Fusion*, vol. 60, Jan 2018.

[74] W. An, M. Zhou, N. Vafaei-Najafabadi, K. Marsh, *et al.*, "Strategies for mitigating the ionization-induced beam head erosion problem in an electron-beam-driven plasma wakefield accelerator," *Phys. Rev. ST Accel. Beams*, vol. 16, Oct 2013.

[75] V. E. Balakin, A. V. Novokhatsky, and V. P. Smirnov, "VLEPP: Transverse Beam Dynamics," in *Proc., 12th Int. Conf. on High-Energy Accelerators, HEACC 1983*, vol. C830811, (Batavia, IL), Fermilab, Fermilab, 1983.

[76] A. Burov, S. Nagaitsev, and V. Lebedev, "Beam breakup mitigation by ion mobility in plasma acceleration," 2018, arXiV: 1808.03860.

[77] T. J. Mehrling, R. A. Fonseca, A. Martinez de la Ossa, and J. Vieira, "Mitigation of the hose instability in plasma-wakefield accelerators," *Phys. Rev. Lett.*, vol. 118, Apr 2017.

[78] E. Adli, J.-P. Delahaye, S. J. Gessner, M. J. Hogan, *et al.*, "A beam driven plasma-wakefield linear collider: From Higgs factory to multi-TeV," in *Proc., 2013 Community Summer Study on the Future of U.S. Particle Physics: Snowmass on the Mississippi (CSS2013)*, (Minneapolis, MN), 2013.

[79] M. Tzoufras, W. Lu, F. Tsung, C. Huang, *et al.*, "Beam loading by electrons in nonlinear plasma wakes," *Physics of Plasmas*, vol. 16, May 2009.

[80] R. D'Arcy, S. Wesch, A. Aschikhin, S. Bohlen, *et al.*, "Tunable plasma-based energy dechirper," *Phys. Rev. Lett.*, vol. 122, Jan 2019.

[81] J. B. B. Chen, D. Schulte, and E. Adli, "e^+e^- beam-beam parameter study for a TeV-scale PWFA linear collider," 2020, arXiV: 2009.13672.

[82] K. Yokoya and P. Chen, "Beam-beam phenomena in linear colliders," *Lect. Notes Phys.*, vol. 400, Apr 1991.

[83] D. Schulte, "Beam-beam effects in linear colliders," *CERN Yellow Reports: School Proceedings*, vol. 3, 2017.

[84] A. Sokolov, I. Ternov, and C. Kilmister, *Radiation from Relativistic Electrons*. American Institute of Physics translation series, American Inst. of Physics, 1986.

[85] A. W. Chao, K. H. Mess, M. Tigner, and F. Zimmermann, *Handbook of Accelerator Physics and Engineering*. World Scientific Publishing Company, 2013.

[86] P. Chen and V. I. Telnov, "Coherent pair creation in linear colliders," *Phys. Rev. Lett.*, vol. 63, Oct 1989.

[87] P. Chen, T. Tauchi, and D. Schroeder, "Pair creation at large inherent angles," in *1990 DPF Summer Study on High-energy Physics: Research Directions for the Decade (Snowmass 90)*, 1990.

[88] V. Baier, V. Fadin, V. Khoze, and E. Kuraev, "Inelastic processes in high energy quantum electrodynamics," *Physics Reports*, vol. 78, no. 3, 1981.

[89] M. Drees and R. M. Godbole, "Resolved photon processes," *J. Phys.*, vol. 21, 1995.

[90] A. Doche, C. Beekman, S. Corde, J. Allen, *et al.*, "Acceleration of a trailing positron bunch in a plasma wakefield accelerator," *Scientific Reports*, vol. 7, Dec 2017.

[91] J. P. Delahaye, M. Diemoz, K. Long, B. Mansoulié, *et al.*, "Muon colliders," 2019, arXiV: 1901.06150.

[92] K. Oide, "Synchrotron Radiation Limit on the Focusing of Electron Beams," *Phys. Rev. Lett.*, vol. 61, 1988.

[93] O. Blanco, R. Tomás, and P. Bambade, "Beam focusing limitation from synchrotron radiation in two dimensions," *Phys. Rev. Accel. Beams*, vol. 19, no. 2, 2016.

[94] J. B. B. Chen, D. Schulte, and E. Adli, "$\gamma\gamma$ beam-beam parameter study for a 3 TeV PWFA linear collider," 2020, arXiV: 2010.00680.

[95] V. Telnov, "Principles of photon colliders," *Nucl. Instr. Meth. Phys. Res. Sec. A*, vol. 355, no. 1, 1995.

[96] I. F. Ginzburg, G. L. Kotkin, V. G. Serbo, and V. I. Telnov, "Colliding ge and gg beams based on the single-pass $e^{\pm}e^{-}$ colliders (VLEPP type)," *Nucl. Instr. Meth. Phys. Res.*, vol. 205, no. 1, 1983.

[97] W. An, W. Lu, C. Huang, X. Xu, *et al.*, "Ion motion induced emittance growth of matched electron beams in plasma wakefields," *Phys. Rev. Lett.*, vol. 118, Jun 2017.

[98] A. V. Fedotov, R. L. Gluckstern, and M. Venturini, "Transverse impedance of a periodic array of cavities," *Phys. Rev. ST Accel. Beams*, vol. 2, Jun 1999.

APPENDIX A

Non-linear Regime Transverse Wake Function

Using the identity

$$\frac{\mathrm{d}}{\mathrm{d}\xi}\left(r_{\mathrm{b}}^2\frac{\mathrm{d}r_{\mathrm{b}}}{\mathrm{d}\xi}\right) = 2r_{\mathrm{b}}\left(\frac{\mathrm{d}r_{\mathrm{b}}}{\mathrm{d}\xi}\right)^2 + r_{\mathrm{b}}^2\frac{\mathrm{d}^2r_{\mathrm{b}}}{\mathrm{d}\xi^2}, \tag{A.1}$$

Lu's equation can be written as

$$\frac{\mathrm{d}}{\mathrm{d}\xi}\left(r_{\mathrm{b}}^2\frac{\mathrm{d}r_{\mathrm{b}}}{\mathrm{d}\xi}\right) + r_{\mathrm{b}} = \frac{4\lambda}{n_0 r_{\mathrm{b}}}. \tag{A.2}$$

Invoking equation (2.120), we obtain

$$-\frac{2\varepsilon_0}{en_0}\frac{\mathrm{d}}{\mathrm{d}\xi}(r_{\mathrm{b}}\mathcal{W}_z) + r_{\mathrm{b}} = \frac{4\lambda}{n_0 r_{\mathrm{b}}}. \tag{A.3}$$

For a beam with a bi-Gaussian particle distribution

$$n_{\mathrm{b}}(r,\xi) = \frac{N}{(2\pi)^{3/2}\sigma_r^2\sigma_z}\exp\left(-\frac{r^2}{2\sigma_r^2} - \frac{\xi^2}{2\sigma_z^2}\right), \tag{A.4}$$

the line distribution is given by

$$\lambda(\xi) = \int_0^\infty n_{\mathrm{b}} r\,\mathrm{d}r = \frac{N}{(2\pi)^{3/2}\sigma_z}\exp\left(-\frac{\xi^2}{2\sigma_z^2}\right), \tag{A.5}$$

normalised as

$$\int_{-\infty}^{\infty}\lambda(\xi)\,\mathrm{d}\xi = \frac{N}{2\pi}. \tag{A.6}$$

In order to obtain the wakefield immediately behind a driving particle placed at ξ', we add a perturbation to the line distribution of the form

$$\delta\lambda = \frac{1}{2\pi}\delta(\xi' - \xi) \tag{A.7}$$

and integrate equation A.3, which yields

$$\mathcal{W}_z(\xi'^{-}) = -\frac{e}{\pi\varepsilon_0 r_\mathrm{b}^2(\xi')}. \tag{A.8}$$

Next, we apply the short-range wake theorem [60, 64, 98] to obtain the transverse wake function. Adapted to our definitions, this reads

$$W_r = -\frac{2}{e r_\mathrm{b}^2(\xi')}\int_{\xi}^{\xi'} \mathcal{W}_z \,\mathrm{d}z = \frac{2}{\pi\varepsilon_0}\frac{\xi' - \xi}{r_\mathrm{b}^4(\xi')}\Theta(\xi' - \xi). \tag{A.9}$$

The Heaviside step function $\Theta(\xi' - \xi)$ has been added, since trailing particles are placed at $\xi < \xi'$ in our convention.

Finally, by making the substitution $r_\mathrm{b}(\xi') \to r_\mathrm{b}(\xi') + \alpha k_\mathrm{p}^{-1}$, we recover the transverse wake function given in chapter 2:

$$\boxed{W_r(\xi' - \xi, \alpha) = \frac{2}{\pi\varepsilon_0}\frac{\xi' - \xi}{(r_\mathrm{b}(\xi') + \alpha k_\mathrm{p}^{-1})^4}\Theta(\xi' - \xi).} \tag{A.10}$$